Universitatea "Politehnica" din Bucureşti
Facultatea de Inginerie Industriala si Robotica
Departamentul de Rezistenţa Materialelor
Splaiul Independenţei nr.313, sector 6, Bucureşti, 060042
☎4029204, 4029213

Winter School on *Trends on Additive Manufacturing for Engineering Applications*

Experimental Fracture Mechanics

Dan Mihai Constantinescu

Department of Strength of Materials
University POLITEHNICA of Bucharest

SIRAMM
H2020-WIDESPREAD-2018,
Project No. 857124
TWINNING
HORIZON 2020

Overview of the presentation

Analytical solutions in LEFM

Strain gage evaluation of SIFs

Photoelastic (2D and 3D) evaluation of SIFs

Digital Image Correlation in Fracture Mechanics and damage initiation

Current research in AM

Analytical solutions in LEFM

Williams' solution

Williams has proposed a biharmonic stress function that can be used for a through thickness plane cracked body with arbitrary shape, size and tractions applied to the outer boundaries. The solution is valid either in plane strain or idealized plane stress.

$$\sigma_r = \sum_{n=1}^{\infty} r^{\frac{n}{2}-1}\left[F_n''(\theta;\lambda) + \left(\frac{n}{2}+1\right) F_n(\theta;\lambda)\right],$$

$$\sigma_\theta = \sum_{n=1}^{\infty} r^{\frac{n}{2}-1}\left[\frac{n}{2}\left(\frac{n}{2}+1\right) F_n(\theta;\lambda)\right],$$

$$\tau_{r\theta} = -\sum_{n=1}^{\infty} r^{\frac{n}{2}-1}\left[\frac{n}{2} F_n'(\theta;\lambda)\right],$$

$$\sigma_r = r^{-\frac{1}{2}}\left\{\frac{C_1}{4}\left[3\sin\frac{3\theta}{2} - 5\sin\frac{\theta}{2}\right] + \frac{D_1}{4}\left[\cos\frac{3\theta}{2} - 5\cos\frac{\theta}{2}\right]\right\} + 4C_2\cos^2\theta +$$

$$+ r^{\frac{1}{2}}\left\{\frac{3C_3}{4}\left[-5\sin\frac{5\theta}{2} - 3\sin\frac{\theta}{2}\right] + \frac{3D_3}{4}\left[\cos\frac{5\theta}{2} + 3\cos\frac{\theta}{2}\right]\right\} + 0(r)\cdots$$

$$\sigma_\theta = r^{-\frac{1}{2}}\left\{\frac{C_1}{4}\left[-3\sin\frac{\theta}{2}-3\sin\frac{3\theta}{2}\right]+\frac{D_1}{4}\left[-3\cos\frac{\theta}{2}-\cos\frac{3\theta}{2}\right]\right\}+4C_2\sin^2\theta+$$

$$+r^{\frac{1}{2}}\left\{\frac{15C_3}{4}\left[-\sin\frac{\theta}{2}+\sin\frac{5\theta}{2}\right]+\frac{15D_3}{4}\left[\cos\frac{\theta}{2}-\frac{1}{5}\cos\frac{5\theta}{2}\right]\right\}+0(r)\cdots$$

$$\tau_{r\theta} = r^{-\frac{1}{2}}\left\{\frac{C_1}{4}\left[3\cos\frac{3\theta}{2}+\cos\frac{\theta}{2}\right]+\frac{D_1}{4}\left[-\sin\frac{\theta}{2}-\sin\frac{3\theta}{2}\right]\right\}-2C_2\sin 2\theta+$$

$$+r^{\frac{1}{2}}\left\{C_3\left[3\cos\frac{\theta}{2}-15\cos\frac{5\theta}{2}\right]+D_3\left[3\sin\frac{\theta}{2}-3\sin\frac{5\theta}{2}\right]\right\}+0(r)\cdots$$

$$C_1=\frac{K_{II}}{\sqrt{2\pi}};\qquad D_1=-\frac{K_I}{\sqrt{2\pi}};\qquad 4C_2=A$$

$$\sigma_x \cong \frac{K_I}{\sqrt{2\pi r}}\cos\frac{\theta}{2}\left(1-\sin\frac{\theta}{2}\sin\frac{3\theta}{2}\right)-\frac{K_{II}}{\sqrt{2\pi r}}\sin\frac{\theta}{2}\left(2+\cos\frac{\theta}{2}\cos\frac{3\theta}{2}\right)+A,$$

$$\sigma_y \cong \frac{K_I}{\sqrt{2\pi r}}\cos\frac{\theta}{2}\left(1+\sin\frac{\theta}{2}\sin\frac{3\theta}{2}\right)+\frac{K_{II}}{\sqrt{2\pi r}}\sin\frac{\theta}{2}\cos\frac{\theta}{2}\cos\frac{3\theta}{2},$$

$$\tau_{xy} \cong \frac{K_I}{\sqrt{2\pi r}}\sin\frac{\theta}{2}\cos\frac{\theta}{2}\cos\frac{3\theta}{2}+\frac{K_{II}}{\sqrt{2\pi r}}\cos\frac{\theta}{2}\left(1-\sin\frac{\theta}{2}\sin\frac{3\theta}{2}\right).$$

Westergaard's solution

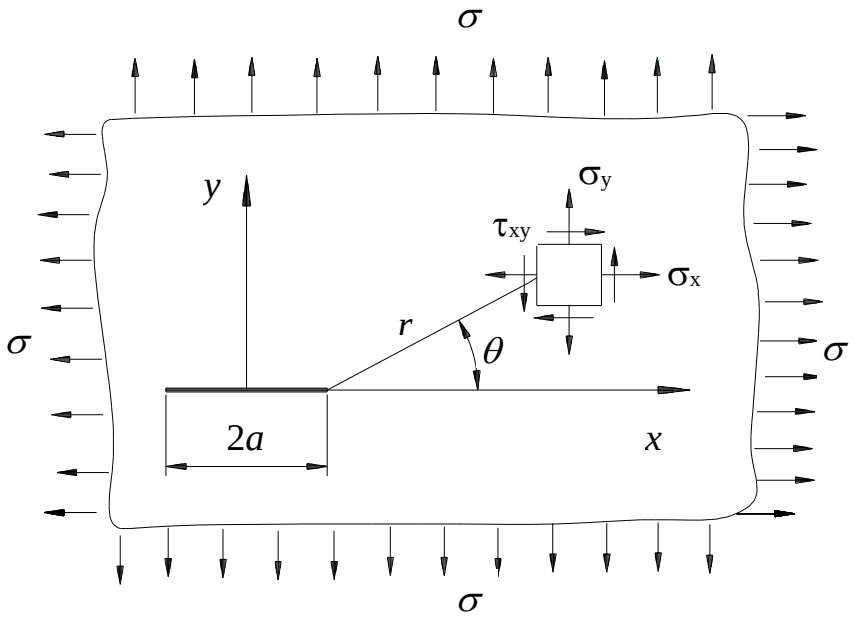

Complex stress function

$$Z(z) = \frac{\sigma \cdot z}{\sqrt{z^2 - a^2}}$$

$z \to \infty$, $Z(z) = \sigma$ $Z(z)$ is real for $|x| > |a|$

$$\sigma_x = \mathrm{Re}Z - y \cdot \mathrm{Im}Z';$$

$$\sigma_y = \mathrm{Re}Z + y \cdot \mathrm{Im}Z';$$

$$\tau_{xy} = -y \cdot \mathrm{Re}Z'.$$

For $y = 0$, $Z(z)$ is real for $|x| > |a|$

$$\sigma_x = \sigma_y = \mathrm{Re}Z(z) = \frac{\sigma \cdot x}{\sqrt{x^2 - a^2}}$$

$z^* = z - a = re^{i\theta}$

$$Z(z^*) = \frac{K_I}{\sqrt{2\pi z^*}} = \frac{K_I}{\sqrt{2\pi r}} e^{-\frac{1}{2}i\theta} = \frac{K_I}{\sqrt{2\pi r}} \left(\cos\frac{\theta}{2} - i \sin\frac{\theta}{2} \right)$$

For any other geometry and loading *Z(z)* has to be changed.

WELLS, A., A., POST, D., The Dynamic Stress Distributions Surrounding a Running Crack - A Photoelastic Analysis, *Proceedings SESA*, Vol. 16, 69-92 and discussion by Irwin, G., R., 93-96, 1958

$$\sigma_x = \mathrm{Re}Z - y\,\mathrm{Im}Z' - \sigma_{ox}$$

Sih's solution

SIH, G.C., On the Westergaard Method of Crack Analysis, *Journal of Fracture Mechanics*, Vol. 2, pp. 628-631, 1966.

Starting from the Goursat-Kolosov solution presented by Muskhelishvili

$$\sigma_x + \sigma_y = 4\,\mathrm{Re}\left[\phi'(z)\right];$$
$$\sigma_x - \sigma_y + 2i\tau_{xy} = 2\left[\bar{z}\phi''(z) + \psi'(z)\right],$$

$$\sigma_x = 2\,\mathrm{Re}\left[\phi'(z)\right] - 2y\cdot\mathrm{Im}\left[\phi''(z)\right] - A;$$
$$\sigma_y = 2\,\mathrm{Re}\left[\phi'(z)\right] + 2y\cdot\mathrm{Im}\left[\phi(z)\right] + A;$$
$$\tau_{xy} = 2y\cdot\mathrm{Re}\left[\phi(z)\right],$$

If $2\phi(z) = Z(z) - A$

$$\sigma_x = \mathrm{Re}\left[Z(z)\right] - y\,\mathrm{Im}\left[Z'(z)\right] - 2A;$$
$$\sigma_y = \mathrm{Re}\left[Z(z)\right] + y\,\mathrm{Im}\left[Z'(z)\right];$$
$$\tau_{xy} = -y\,\mathrm{Re}\left[Z'(z)\right].$$

Eftis-Liebovitz solution

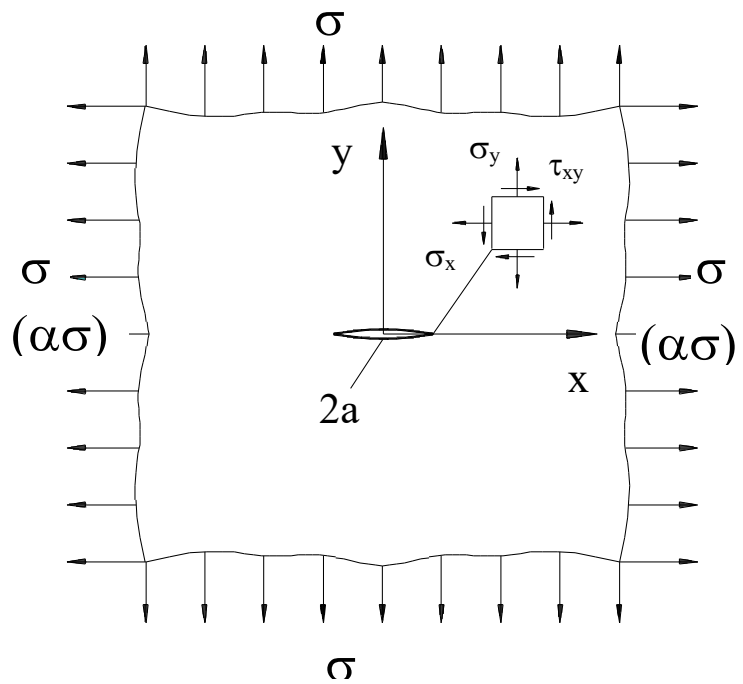

In terms of the holomorphic functions

$$\phi(z) \qquad \psi(z) = \Psi'(z)$$

$$\sigma_x + \sigma_y = 2\left[\phi'(z) + \overline{\phi'(z)}\right] = 4\,\mathrm{Re}\left[\phi'(z)\right]$$

$$\sigma_y - \sigma_x + 2i\tau_{xy} = 2\left[\bar{z}\cdot\phi''(z) + \psi'(z)\right]$$

$$\sigma_y - i\tau_{xy} = \phi'(z) + \overline{\phi'(z)} + z\cdot\overline{\phi''(z)} + \overline{\psi'(z)}$$

$$\sigma_y + i\tau_{xy} = 2\,\mathrm{Re}\left[\phi'(z)\right] + \left[\bar{z}\cdot\phi''(z) + \psi'(z)\right]$$

Equating the imaginary parts, imposing zero shear stress along the *x* - axis (*y* = 0) and considering $\bar{z} = z$

$$\mathrm{Im}\left[z\cdot\phi''(z) + \psi'(z)\right]\Big|_{y=0} = 0 \qquad \text{or} \qquad z\cdot\phi''(z) + \psi'(z) + B = 0$$

EFTIS, J., LIEBOWITZ, H., On the Modified Westergaard Equations for Certain Plane Crack Problems, *Journal of Fracture Mechanics*, Vol. 8, 383-391, 1972.

$$2\phi'(z) = \frac{\sigma\cdot z}{\sqrt{z^2 - a^2}} + B \qquad B = -\frac{(1-\alpha)\sigma}{2} \qquad 2A = (1\text{-}\alpha)\sigma$$

Sanford's solution

SANFORD, R.J., A Critical re-examination of the Westergaard method for solving opening mode problems. *Mechanics Research Communications*, **6**, 289-294, 1979.

$$\eta(z) = z \cdot \phi''(z) + \psi'(z) \qquad \mathrm{Im}[\eta(z)] = 0 \qquad \text{for } \tau_{xy} = 0$$

$$2\phi'(z) = Z(z) - \eta(z)$$

$$Z(z) = \sum_{n=0}^{N} A_n z^{n-\frac{1}{2}},$$

$$Y(z) = \sum_{m=0}^{M} B_m z^m \ .$$

$$\sigma_x = \mathrm{Re}[Z(z)] - y \cdot \mathrm{Im}[Z'(z)] - y \cdot \mathrm{Im}[Y'(z)] + 2\,\mathrm{Re}[Y(z)]$$

$$\sigma_y = \mathrm{Re}[Z(z)] + y \cdot \mathrm{Im}[Z'(z)] + y \cdot \mathrm{Im}[Y'(z)]$$

$$\tau_{xy} = -y \cdot \mathrm{Re}[Z'(z)] - y\,\mathrm{Re}[Y'(z)] - \mathrm{Im}[Y(z)]$$

DALLY, J.W., SANFORD, R.J., Strain gage methods for measuring the opening-mode stress intensity factor "K_I". *Experimental Mechanics*, **27**, 391-388, 1987.

BERGER, J.R., DALLY, J.W., SANFORD, R.J., Extend of validity of three-parameter crack-tip strain fields. *Proceedings SEM Spring Conference on Experimental Mechanics*, Milwaukee, Wisconsin, 572-578, 1991.

CHONA, R., FOURNEY, W.L., SANFORD, R.J., SHUKLA, A., Determining stress intensity factors for running cracks. *Modeling Problems in Crack Tip Mechanics*, Waterloo, Ontario, Canada, 207-215, 1983.

Strain gages evaluation of SIFs

$$Z(z) = \sum_{n=0}^{N} A_n z^{n-1/2} \;;\; Y(z) = \sum_{m=0}^{M} B_m z^m \quad (z = x + iy) \;;$$

$$Z'(z) = \frac{dZ(z)}{dz} \;;\; Y'(z) = \frac{dY(z)}{dz} \;.$$

$$E\varepsilon_x = (1-\nu)\,\mathrm{Re}\,Z(z) - (1+\nu)\,y\,\mathrm{Im}\,Z'(z) - (1+\nu)\,y\,\mathrm{Im}\,Y'(z) + 2\,\mathrm{Re}\,Y(z) \;;$$

$$E\varepsilon_y = (1-\nu)\,\mathrm{Re}\,Z(z) - (1+\nu)\,y\,\mathrm{Im}\,Z'(z) - (1+\nu)\,y\,\mathrm{Im}\,Y'(z) - 2\nu\,\mathrm{Re}\,Y(z) \;;$$

$$G\gamma_{xy} = -y\,\mathrm{Re}\,Z'(z) - y\,\mathrm{Re}\,Y'(z) - \mathrm{Im}\,Y(z) \;,$$

$$\varepsilon_{x'} = \varepsilon_x \cos^2\alpha + \varepsilon_y \sin^2\alpha + \gamma_{xy} \sin\alpha\cos\alpha \;.$$

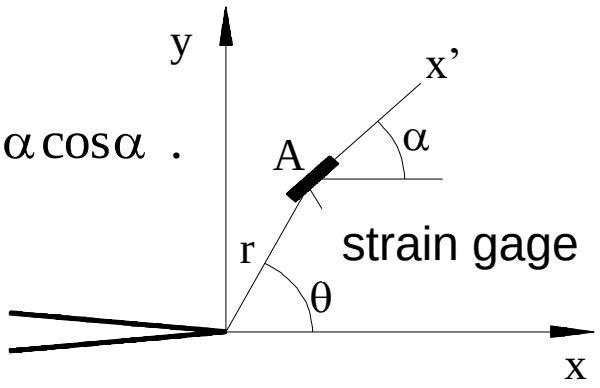

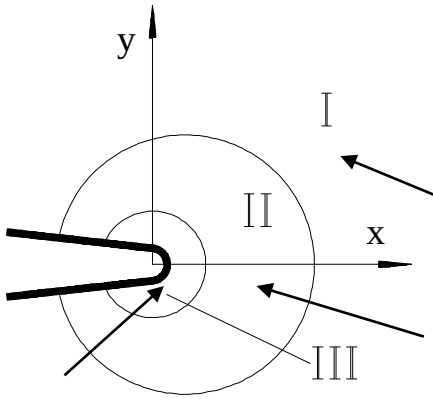

I – expanded solution

II - K-dominance region

III - process zone

In a representation with 6 terms, N = M = 2, the unknown coefficients are: A_o , A_1 , A_2 , B_o , B_1 , B_2.

$$E\varepsilon_{x'} = A_o r^{-1/2}\left\{\cos\frac{\theta}{2}\left[\cos^2\alpha\left((1-\nu)-(1+\nu)\sin\frac{\theta}{2}\sin\frac{3\theta}{2}\right)+\sin^2\alpha\left((1-\nu)+(1+\nu)\sin\frac{\theta}{2}\sin\frac{3\theta}{2}\right)\right]+\right.$$

$$\left.+(1+\nu)\sin\alpha\cos\alpha\sin\theta\cos\frac{3\theta}{2}\right\}+$$

$$+A_1 r^{1/2}\left\{\cos\frac{\theta}{2}\left[\cos^2\alpha\left((1-\nu)+(1+\nu)\sin^2\frac{\theta}{2}\right)+\sin^2\alpha\left((1-\nu)-(1+\nu)\sin^2\frac{\theta}{2}\right)\right]-\right.$$

$$\left.-(1+\nu)\sin\alpha\cos\alpha\sin\theta\cos\frac{\theta}{2}\right\}+$$

$$+A_2 r^{3/2}\left[\cos^2\alpha\left((1-\nu)\cos\frac{3\theta}{2}-\frac{3}{2}(1+\nu)\sin\theta\sin\frac{\theta}{2}\right)+\sin^2\alpha\left((1-\nu)\cos\frac{3\theta}{2}+\frac{3}{2}(1+\nu)\sin\theta\sin\frac{\theta}{2}\right)-\right.$$

$$\left.-3(1+\nu)\sin\alpha\cos\alpha\sin\theta\cos\frac{\theta}{2}\right]+$$

$$+B_o\left(\cos^2\alpha-\nu\sin^2\alpha\right)+$$

$$+B_1 r\left[\cos^2\alpha\cos\theta-\nu\sin^2\alpha\cos\theta-2(1+\nu)\sin\alpha\cos\alpha\sin\theta\right]+$$

$$+2B_2 r^2\left[\cos^2\alpha\left(1-(3+\nu)\sin^2\theta\right)+\sin^2\alpha\left((1+2\nu)\sin^2\theta-\nu\cos^2\theta\right)-2(1+\nu)\sin\alpha\cos\alpha\sin 2\theta\right]$$

Considering only the first 3 terms, unknown coefficients: Ao, A1, Bo

But B_o=0 if $$\cos 2\alpha = -\frac{1-\nu}{1+\nu} \ ,$$

and A_1=0 if $$\operatorname{tg}\frac{\theta}{2} = -\operatorname{ctg} 2\alpha$$

Resulting $$K_I = A_o \sqrt{2\pi}$$

with A_o being established by measuring strain along x' direction as

$$E\varepsilon_{x'} = A_0 r^{-1/2}\left\{\cos\frac{\theta}{2}\left[\cos^2\alpha\left((1-\nu)-(1+\nu)\sin\frac{\theta}{2}\sin\frac{3\theta}{2}\right)+\sin^2\alpha\left((1-\nu)+(1+\nu)\sin\frac{\theta}{2}\sin\frac{3\theta}{2}\right)\right]+\right.$$

$$\left.+(1+\nu)\sin\alpha\cos\alpha\sin\theta\cos\frac{3\theta}{2}\right\}.$$

Experimental evaluation of SIFs

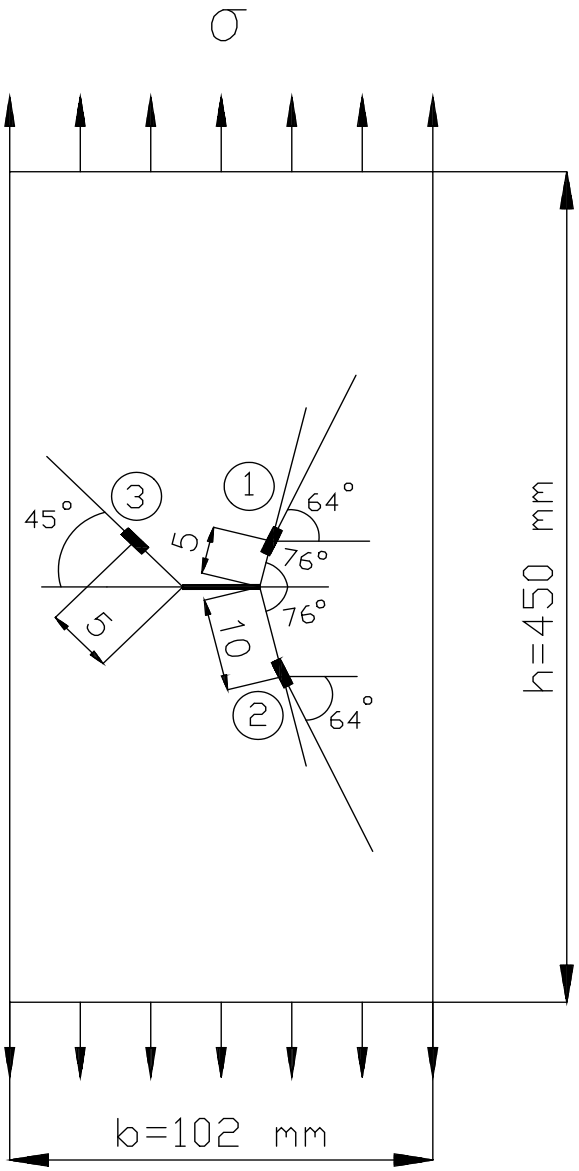

Aa steel plate with central crack, electro discharged with a wire of thickness of 0,15 mm. The central crack is of length $2a$ = 20 mm. The elastic constants of the material are: ν = 0,24 and E = 2,19105 MPa. With a known Poisson's ratio ν we establish the angle $\alpha = 64^{o}$ and angle $\theta = 76^{o}$.

$$E\varepsilon_{x'} = 0{,}744424\, A_0 r^{-1/2}. \qquad K_{I\,\exp} = A_0\sqrt{2\pi}$$

We chose the distances from the crack tip in points 1 and 2, as being 5 mm and 10 mm, symmetric with respect to the crack. Another strain gauge was positioned at r = 5 in point 3, close to the other tip of the crack.

Strain gages LY11 Höttinger strain gauges with a gauge length of 0,6 mm, resistance R = 120 Ω, and a constant k = 1,87.

F [kN]		80	90	100	110	120
σ [MPa]		156,8	176,5	196,1	215,7	235,4
K_{Ith} [MPa$\sqrt{mm}$]		900,3	1013,4	1125,9	1238,5	1351,6
K_{Iexp} [MPa$\sqrt{mm}$]	1	781,6	885,5	982,7	1088,3	1182,3
	2	897,8	1002,7	1121,6	1205,6	1294,2
	3	625,1	715,4	807,1	896	989,1

The experimentally established SIFs are in a very good correlation with the theoretical values in point 2, not so close to the crack tip.

In point 1, probably influenced by the process zone, the strains and the SIFs are diminished – it looks like the LEFM equations are not valid any more.

It is important to underline that for point 3, where an arbitrary angle of
$\alpha = \theta = 45^o$
the obtained SIFs are much smaller than in point 1 which is at the same distance from the crack tip.

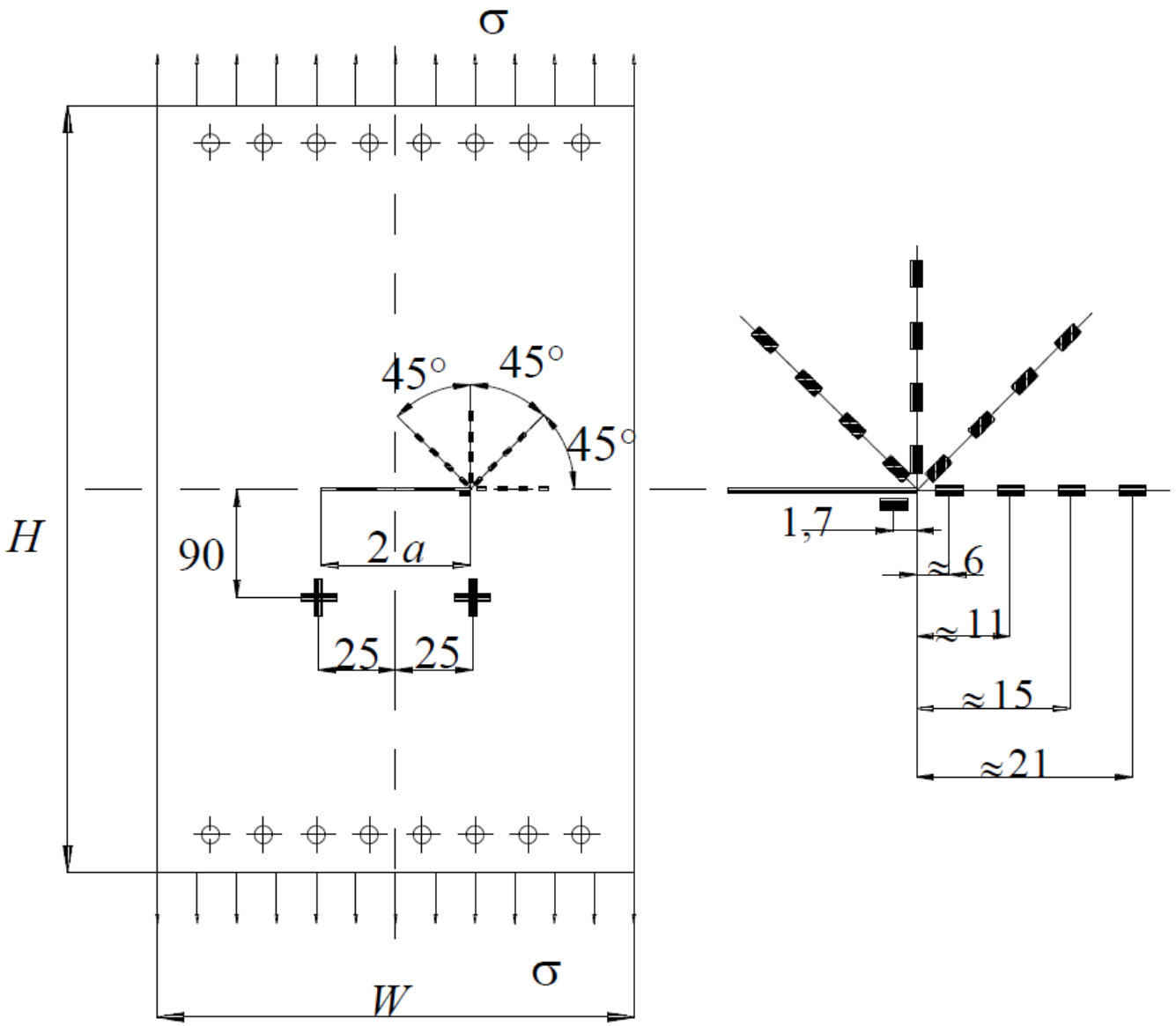
σ
45°
45°
45°
H
90
2a
25
25
W
σ
1,7
≈6
≈11
≈15
≈21

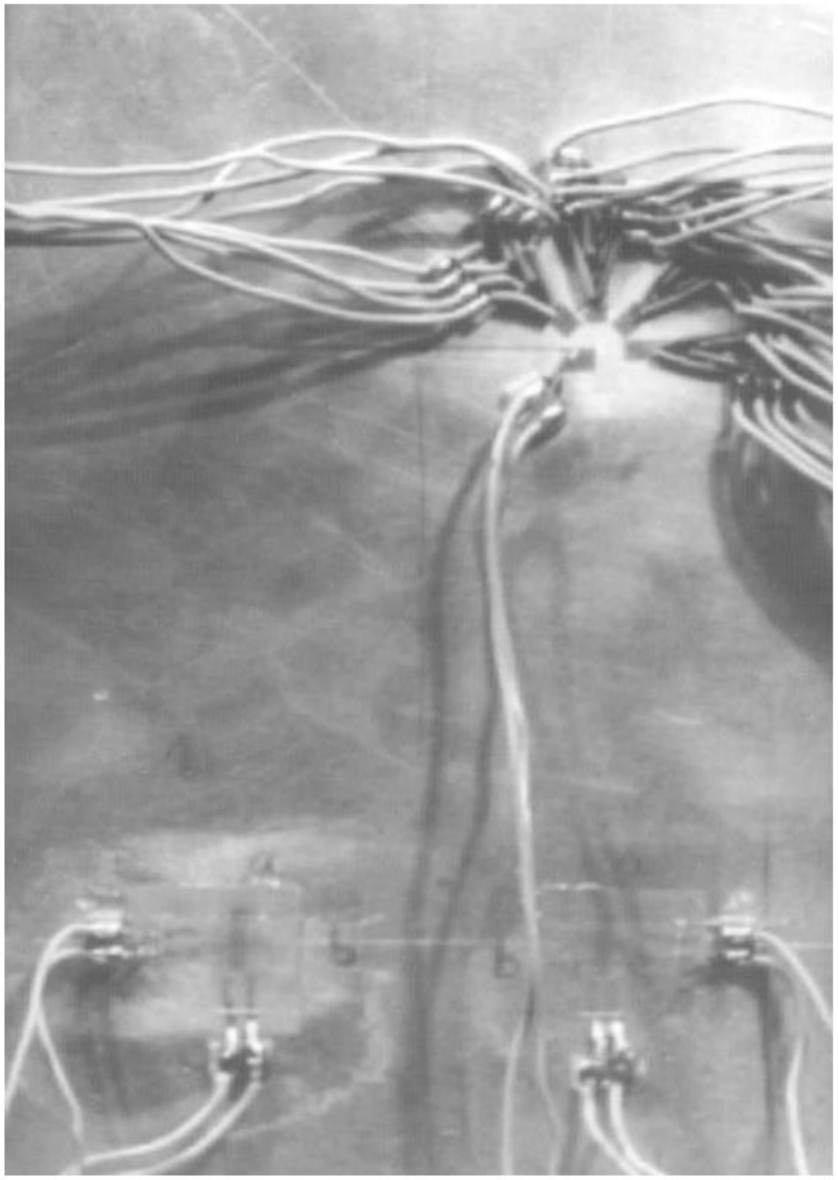

Aluminum plate E = 61000 MPa , and ν = 0,3.

The plate has the following dimensions:

- height H = 580 mm,
- width W = 240 mm
- thickness t = 2,5 mm.

The through thickness crack has a width of 0,2 mm. The length of the central crack is the same

$2a$ = 48 mm,

The dimensions of the width of the plate are changed as to obtain:

$2a/W$ = 0,2 ;

$2a/W$ = 0,3

$2a/W$ = 0,4.

Along radial lines defined by the angles of θ = 0°; θ = 45°; θ = 90° and θ = 135°, the strains are measured on each direction in four points with Höttinger gauges 0,6/120 LY 13, compensated for aluminum, a gage length of 0,6 mm and the constant k = 1,65 $\pm$ 1,5 %

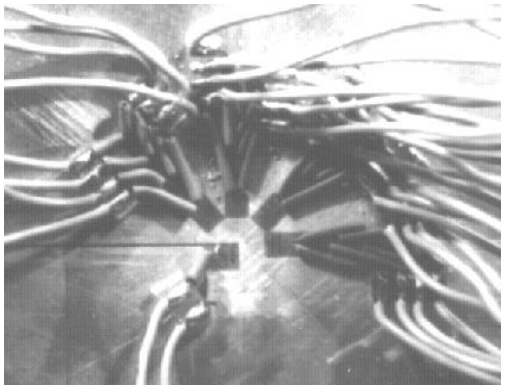

2a / W = 0.3

θ = 0°

$G * \varepsilon_{x'} / \sigma$

strains

1 term

2 terms

3 terms

4 terms

σ = 1.98 MPa

σ = 4.01 MPa

σ = 5.90 MPa

2.00
1.75
1.50
1.25
1.00
0.75
0.50
0.25
0.00
-0.25

0.00 0.10 0.20 0.30 0.40 0.50 0.60 0.70 0.80 0.90 1.00

r / a

2a / W = 0.3

θ = 90°

$G * \varepsilon_{x'} / \sigma$

strains

1 term

2 terms

3 terms

4 terms

σ = 1.98 MPa

σ = 4.01 MPa

σ = 5.90 MPa

2.75
2.50
2.25
2.00
1.75
1.50
1.25
1.00
0.75
0.50
0.25
0.00

0.00 0.10 0.20 0.30 0.40 0.50 0.60 0.70 0.80 0.90 1.00

r / a

Photoelastic (2D and 3D) evaluation of SIFs

2D Photoelasticity

POST, D., Photoelastic Stress Analysis for an Edge Crack in a Tensile Field, *Proceedings SESA*, **12**, 99-116, 1954.

WELLS, A., A., POST, D., The Dynamic Stress Distributions Surrounding a Running Crack - A Photoelastic Analysis, *Proceedings SESA*, **16**, pp.69-92 and discussion by Irwin, G., R., 93-96, 1958.

COTTERELL, B., On Brittle Fracture Paths, *Int. J. Fract. Mech.*, **1**, 96-103, 1965.

BRADLEY, W.B., KOBAYASHI, A.S., Fracture Dynamics. A Photoelastic Investigation, *J. Engng. Fract. Mech*., **3**, 317-332, 1971.

THEOCARIS, P.S., GDOUTOS, E.E., A Photoelastic Determination of K_I Stress Intensity Factors, *J. Engng. Fract. Mech.*, **7**, 331-339, 1975.

DALLY, J.W., SANFORD, R.J., Classification of Stress Intensity Factors from Isochromatic Fringe Pattern, *Experimental Mechanics*, 441-448, December 1978.

SANFORD, R.J., DALLY, J.W., A General Method for Determining Mixed-Mode. Stress Intensity Factors from Isochromatic Fringe Patterns, *Engng. Fract. Mech.*, **11**, 621-633, 1979.

SMITH, C.W., *Use of Photoelasticity in Fracture Mechanics*, in Mehanics of Fracture, G.C. Sih, Ed., vol. 7, ch. 2, pp.163-187, Martinus Nijhoff, 1981.

SMITH, C.W., WIERSMA, S.J., Stress-Fringe Signatures for Propagating Cracks, *Engng. Fract. Mech.*, **23**, pp. 229-236, 1986.

SMITH, C.W., KOBAYASHI, A.S., *Experimental Fracture Mechanics*, Ch. 19 of Handbook on Experimental Mechanics, SEM, Inc., A.S. Kobayashi, Ed., Prentice-Hall, Inc., Englewood Cliffs, NJ, pp. 891-956, 1987.

$$\sigma_x = \frac{K_I}{\sqrt{8\pi r}}\cos\frac{\theta}{2}\left(1-\sin\frac{\theta}{2}\sin\frac{3\theta}{2}\right)+\sigma_{ox}+$$

$$+\sum_{n=3}^{\infty}\left(A_n\frac{n}{2}\right)r^{\frac{n}{2}-1}\left\{\left[2+(-1)^n+\frac{n}{2}\right]\cos\left(\frac{n}{2}-1\right)\theta-\left(\frac{n}{2}-1\right)\cos\left(\frac{n}{2}-3\right)\theta\right\}$$

$$\sigma_y = \frac{K_I}{\sqrt{8\pi r}}\cos\frac{\theta}{2}\left(1+\sin\frac{\theta}{2}\sin\frac{3\theta}{2}\right)+$$

$$+\sum_{n=3}^{\infty}\left(A_n\frac{n}{2}\right)r^{\frac{n}{2}-1}\left\{\left[2-(-1)^n-\frac{n}{2}\right]\cos\left(\frac{n}{2}-1\right)\theta-\left(\frac{n}{2}-1\right)\cos\left(\frac{n}{2}-3\right)\theta\right\}$$

$$\sigma_{xy} = \frac{K_I}{\sqrt{8\pi r}}\sin\frac{\theta}{2}\cos\frac{\theta}{2}\cos\frac{3\theta}{2}-$$

$$-\sum_{n=3}^{\infty}\left(A_n\frac{n}{2}\right)r^{\frac{n}{2}-1}\left\{\left[(-1)^n+\frac{n}{2}\right]\sin\left(\frac{n}{2}-1\right)\theta-\left(\frac{n}{2}-1\right)\sin\left(\frac{n}{2}-3\right)\theta\right\}$$

Photoelasticity is a nondestructive, whole-field, graphic stress-analysis technique based on an optomechanical property called *birefringence*, possessed by many transparent polymers.

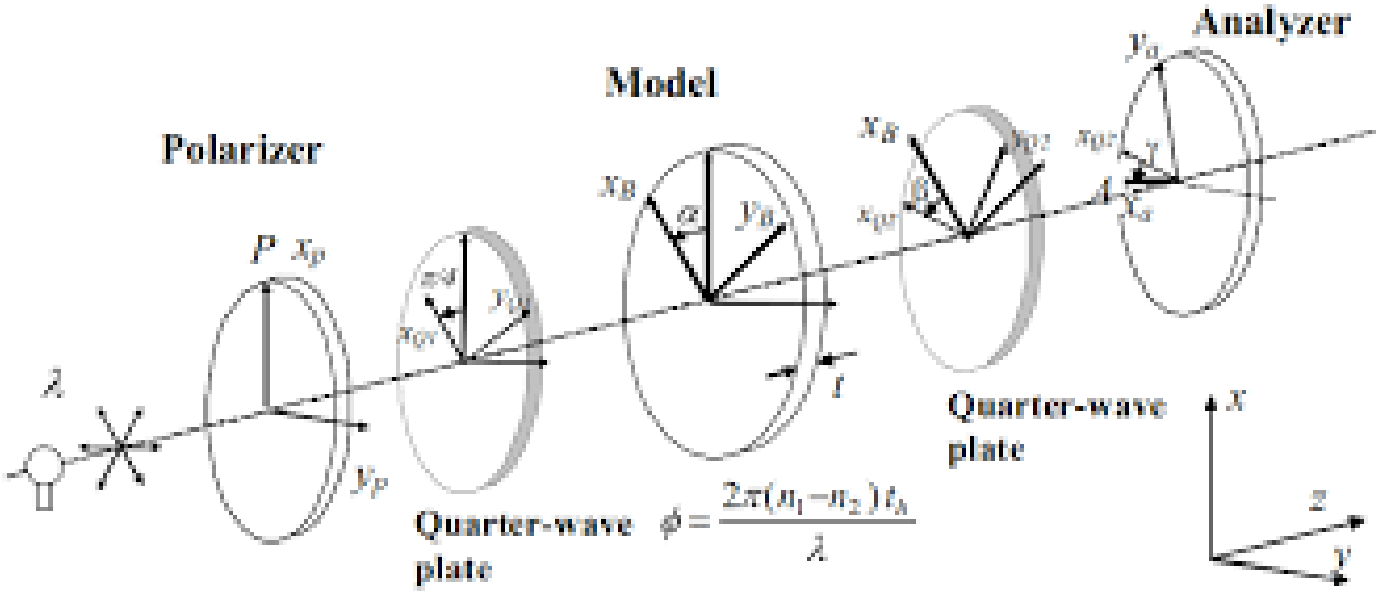

Photoelastic materials are birefringent, that is, they act as temporary wave plates, refracting light differently for different light-amplitude orientations, depending upon the state of stress in the material.

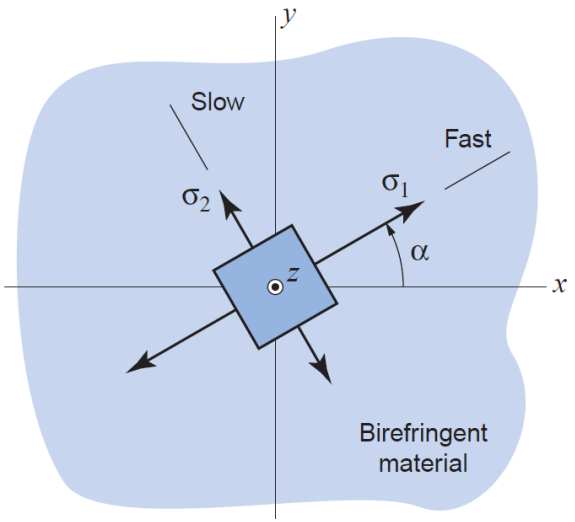

Tardy Compensation Method

The analyzer *alone* is rotated through some angle γ until a neighboring (dark) isochromatic of *integer* order *n* passes through the point in question.

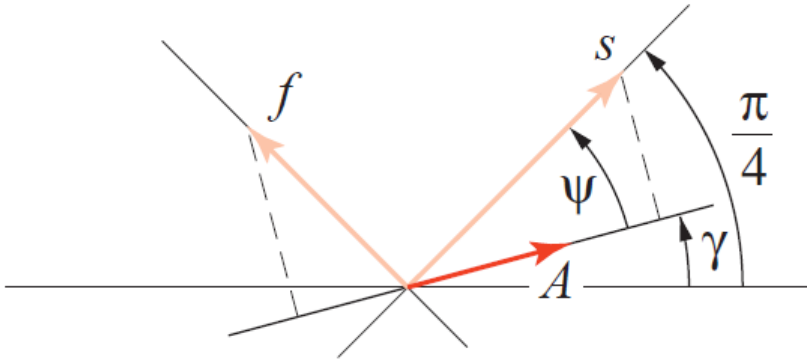

The fractional fringe order is then equal to the ratio γ / π, as will be shown subsequently.

Therefore the value of *N* at the point is

$$N = n \pm \gamma / \pi \ .$$

Fringe Order Multiplication

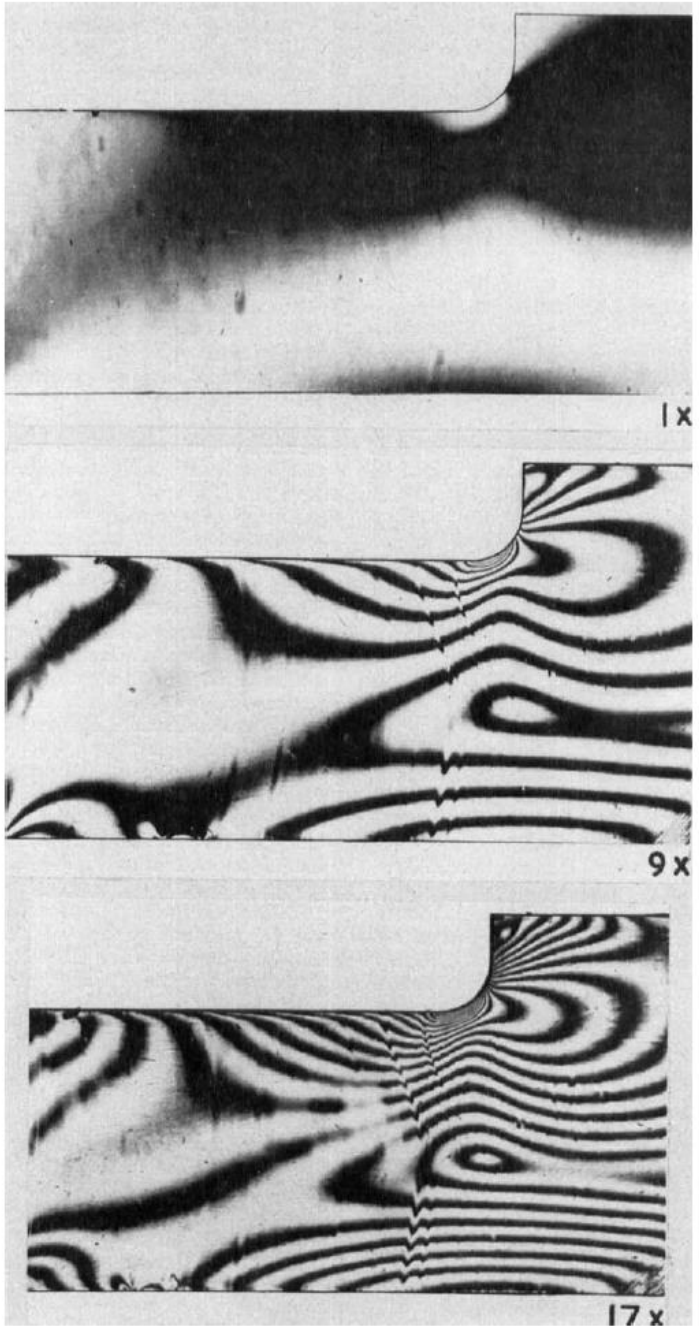

Fig. 3. 1, 9 and 17 fringe multiplication for slice from pressure vessel header study. Slice thickness 0·051 in

Since the slices are thin, and the number of fringes will be proportional to the slice thickness, it is necessary to optically increase the number of fringes for accurate analysis.

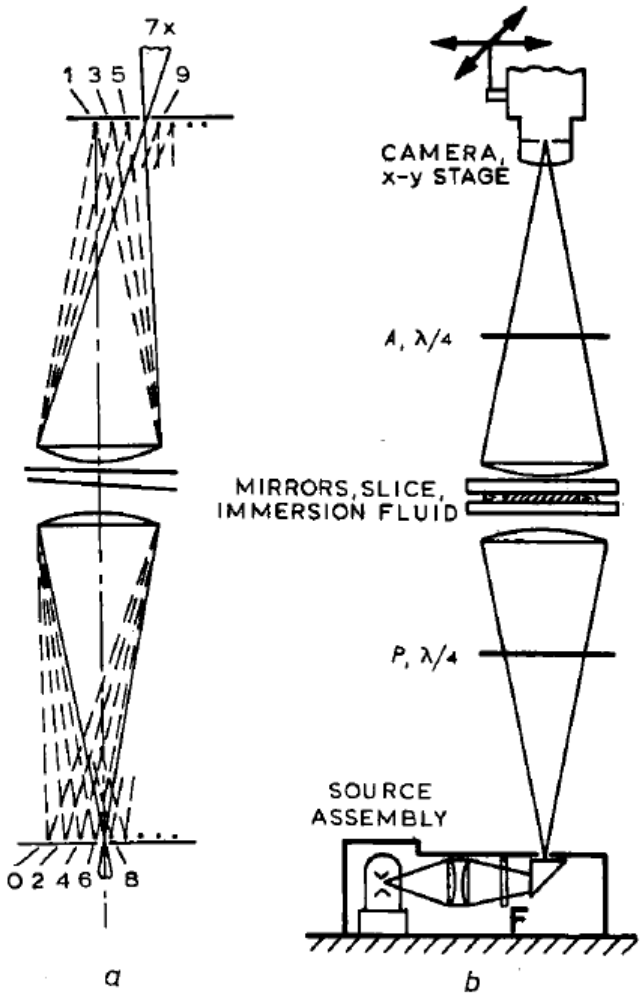

a Convergence of reflected rays.
b Experimental apparatus.
P polarizer, A analyser, F filter.

Fig. 5

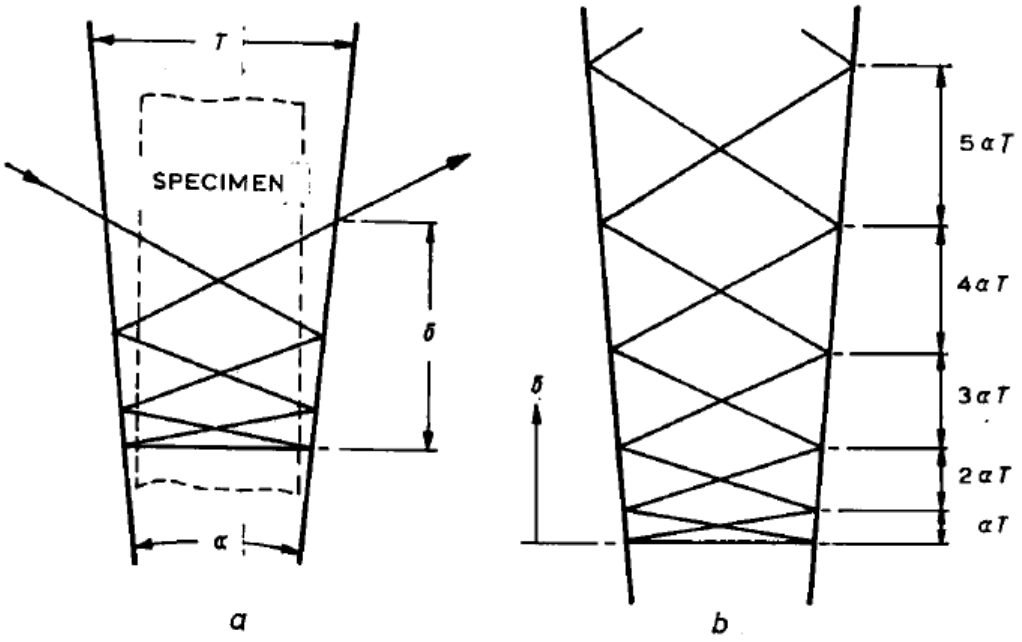

a Optimum path for multiplication by 7.
b Accumulation of path spread with increasing multiplication.

Fig. 6

POST, D. Fringe multiplication in three dimensional photoelasticity, *Journal of Strain Analysis*, **1**, 380–388, 1966.

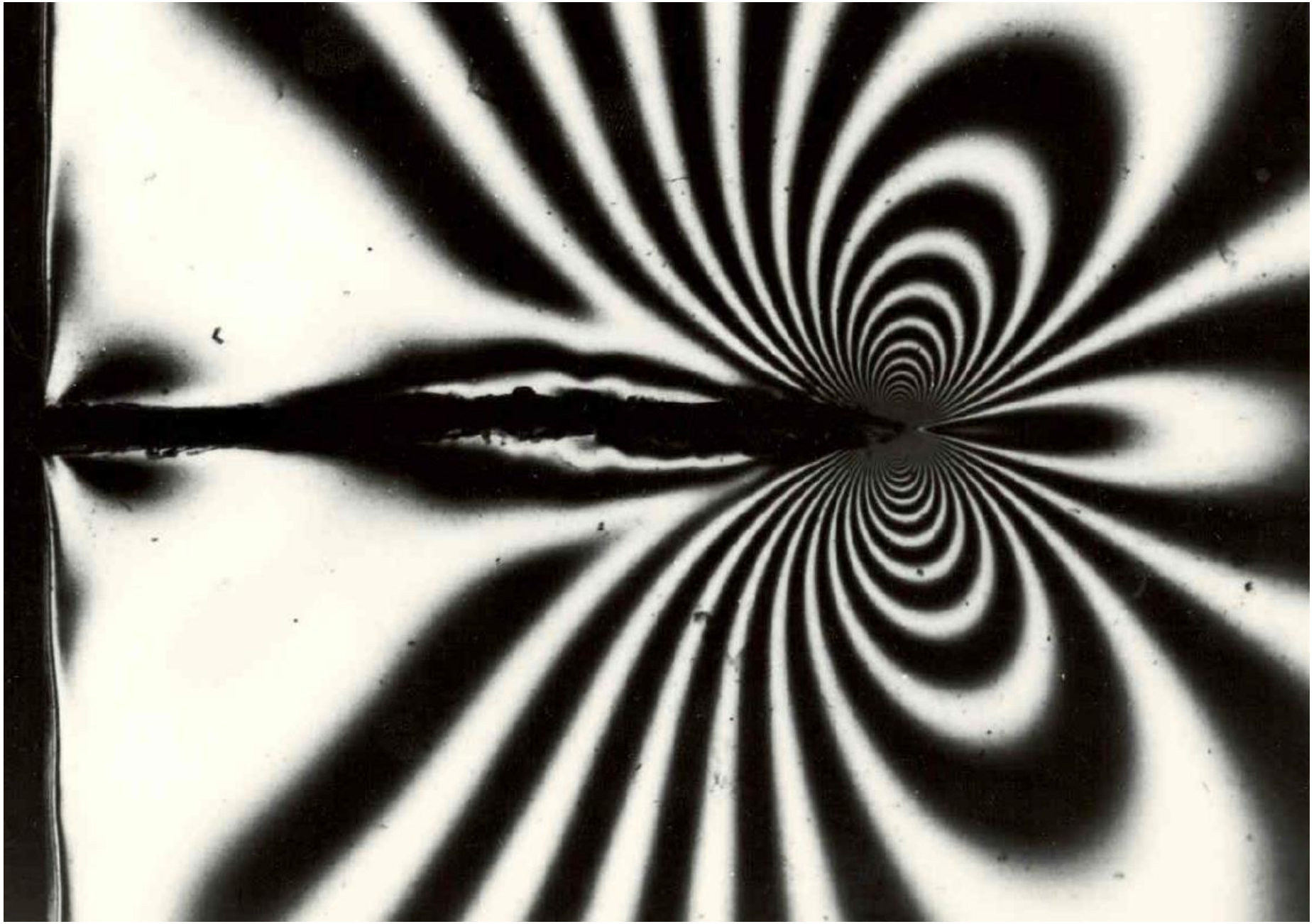

Initial SIF evaluation

MODE I ALGORITHM

Beginning with the Griffith-Irwin Equations, we may write, for Mode I, for the homogeneous case,

$$\sigma_{ij} = \frac{K_1}{(2\pi r)^{\frac{1}{2}}} f_{ij}(\theta) + \sigma^{\circ}_{ij} \qquad (i,j = n,z) \quad (1)$$

where:

σ_{ij} are components of stress

K_1 is SIF

r, θ are measured from crack tip (Fig. B-1)

σ°_{ij} are non-singular stress components.

Then, along $\theta = \pi/2$, after truncating σ_{ij}

$$\tau^{\max}_{nz} = \frac{K_1}{(8\pi r)^{\frac{1}{2}}} + \tau^{\circ} = \frac{K_{AP}}{(8\pi r)^{\frac{1}{2}}} \qquad (2)$$

where: $\tau^{\circ} = f(\sigma^{\circ}_{ij})$ and is constant over the data range

K_{AP} = apparent SIF

$\tau^{\max}_{nz}$ = maximum shear stress in nz plane

$$\therefore \frac{K_{AP}}{\bar{\sigma}(\pi a)^{\frac{1}{2}}} = \frac{K_1}{\bar{\sigma}(\pi a)^{\frac{1}{2}}} + \frac{\sqrt{8}\tau^{\circ}}{\bar{\sigma}} \left(\frac{r}{a}\right)^{\frac{1}{2}} \qquad (3)$$

where (Fig. B-1) a = crack length, and $\bar{\sigma}$ = remote normal stress

i.e. $\frac{K_{AP}}{\bar{\sigma}(\pi a)^{\frac{1}{2}}}$ vs. $\sqrt{\frac{r}{a}}$ is linear.

Since from the Stress-Optic Law

$\tau^{\max}_{nz} = \frac{nf}{2t}$ where

n = stress fringe order

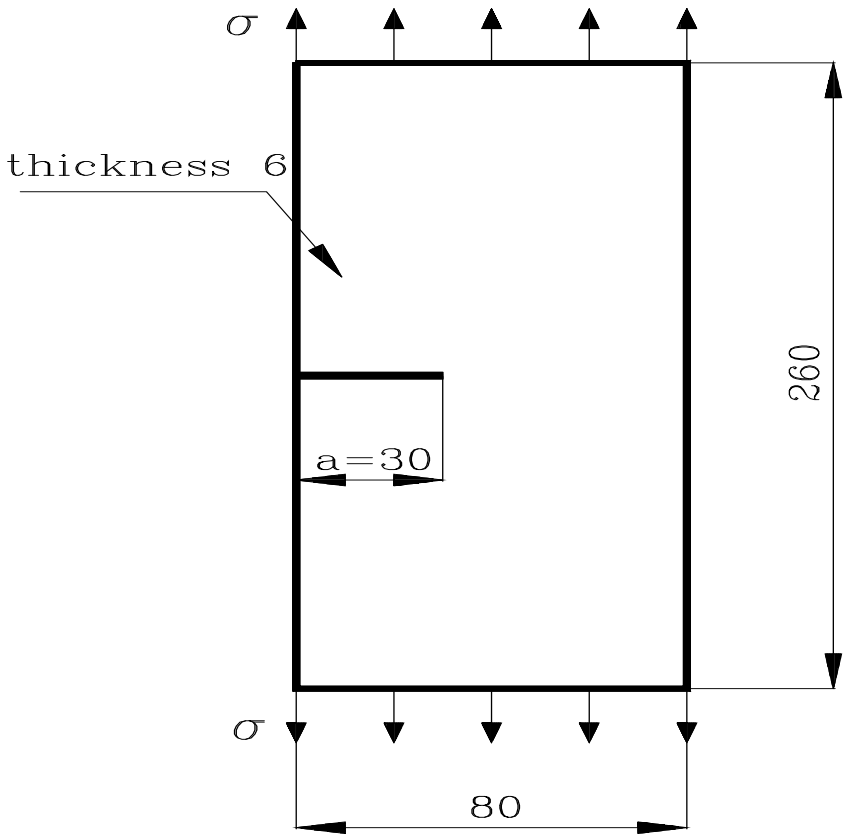

r [mm]	n [fringes]	τ_{max} [MPa]	K_{AP} [MPa$\sqrt{mm}$]	$\sqrt{r/a}$	$K_{AP}/\sigma\sqrt{\pi a}$
1	1.51	1.51	7.570017	0.182574	2.757165
2	1.125	1.125	7.976042	0.258199	2.905048
3	0.87	0.87	7.554397	0.316228	2.751475
4	0.735	0.735	7.369487	0.365148	2.684127
5	0.69	0.69	7.734888	0.408248	2.817214
6	0.66	0.66	8.104748	0.447214	2.951925
7	0.615	0.615	8.157256	0.483046	2.97105
8	0.58	0.58	8.224186	0.516398	2.995427
9	0.54	0.54	8.121476	0.547723	2.958018
10	0.52	0.52	8.243721	0.57735	3.002542

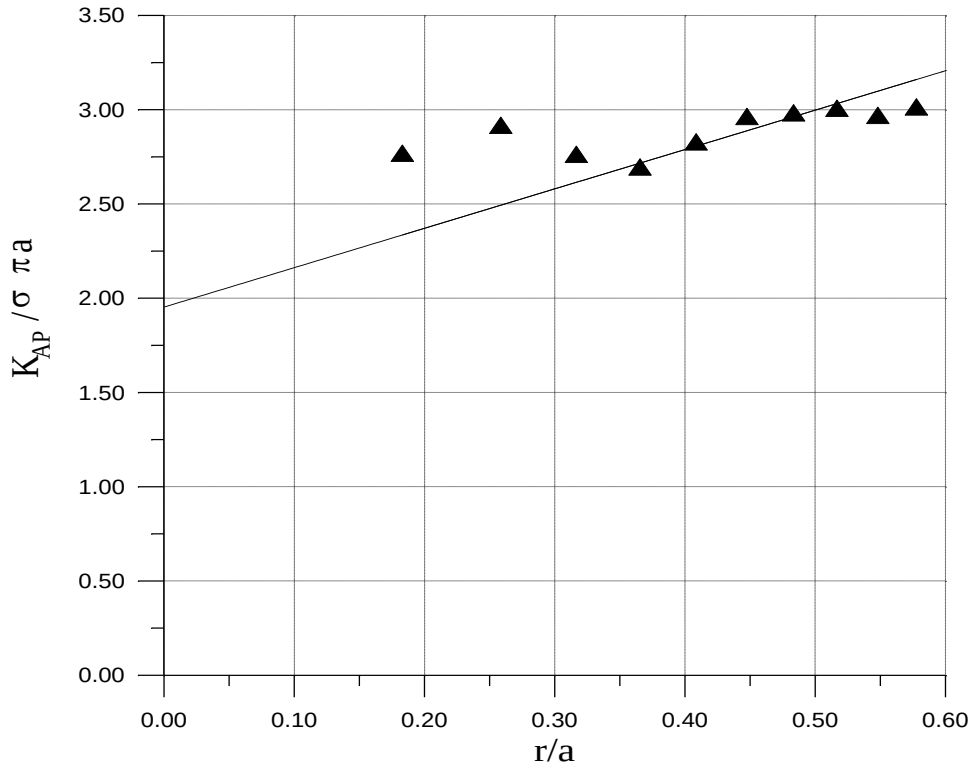

The general recommendation is that

$$\sqrt{r/a} = 0.2 \ldots 0.5$$

$[\mathrm{MPa}\sqrt{\mathrm{mm}}]$

Remote stress σ [MPa]	Theoretical SIF K_{Ith} $[\mathrm{MPa}\sqrt{\mathrm{mm}}]$	Experimental SIF K_{Iexp} $[\mathrm{MPa}\sqrt{\mathrm{mm}}]$	Error [%]
0.283	5.42	5.74	5.9
0.377	7.22	7.26	0.6
0.471	9.03	10.77	19.3
0.566	10.83	11.09	2.4

At four different remote unit stress levels the error between the experimental and theoretical SIF is calculated and presented.

Experimental SIFs are greater that the theoretical SIFs, and the error was between 1 and 20%.

Mixed Mode (Bimaterial) SIF evaluation

Mixed Mode Algorithm

The mixed mode algorithm was developed (see Fig. 9) by requiring that:

$$\lim_{\substack{r_m \to 0 \\ \Theta_m \to \Theta_m^0}} \left\{ (8\pi r_m)^{1/2} \frac{\delta(\tau)_{nz}^{\max}}{\delta \Theta} (K_1, K_2, r_m, \Theta_m, \tau_{ij}) \right\} = 0$$

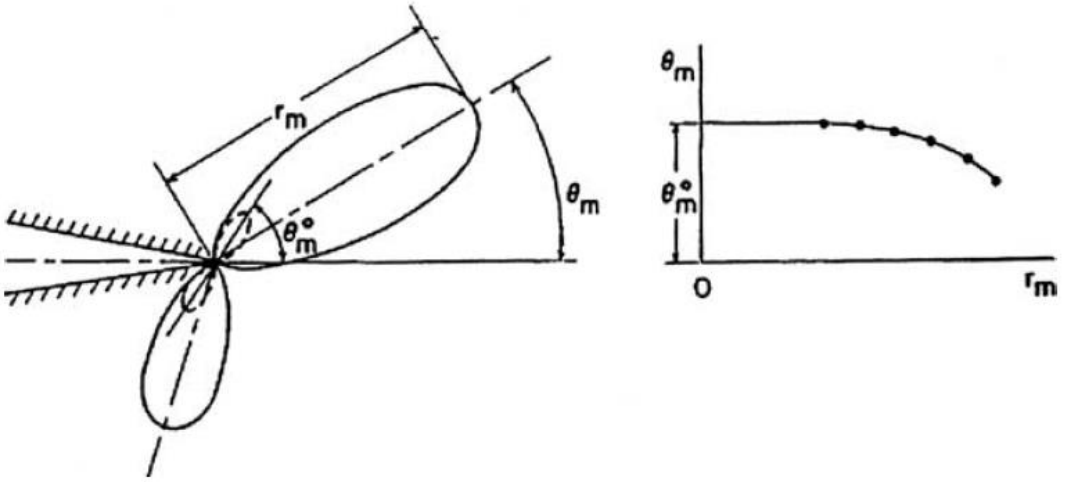

Fig. 9. Determination of θ_m^0 for mixed mode loading.

which leads to

$$\left(\frac{K_2}{K_1}\right)^2 - \frac{4}{3}\left(\frac{K_2}{K_1}\right)\cot 2\Theta_m^0 - \frac{1}{3} = 0 \tag{A.5}$$

By measuring Θ_m^0 which is approximately in the direction of the applied load, K_2/K_1 can be determined.

Then writing the stress-optic law as

$$\tau_{nz}^{\max} = \frac{fn}{2t} = \frac{K_{\mathrm{AP}}^*}{(8\pi r)^{1/2}}$$

where K_{AP}^* is the mixed mode of SIF, one may plot $K_{\mathrm{AP}}^*/(\bar{\sigma}(\pi a)^{1/2})$ vs. $\sqrt{r/a}$ as before, locate a linear zone and extrapolate to $r = 0$ to obtain K^*. Knowing, K^*, K_2/K_1 and Θ_m^0, values of K_1 and K_2 may be determined since

$$K^* = [(K_1 \sin\Theta_m^0 + 2K_2 \cos\Theta_m^0)^2 + (K_2 \sin\Theta_m^0)^2]^{1/2} \tag{A.6}$$

Knowing K^* and θ_m^0, K_1 and K_2 can be determined from Eqs. (A.5) and (A.6). Details are found in Smith and Kobayashi (1993).

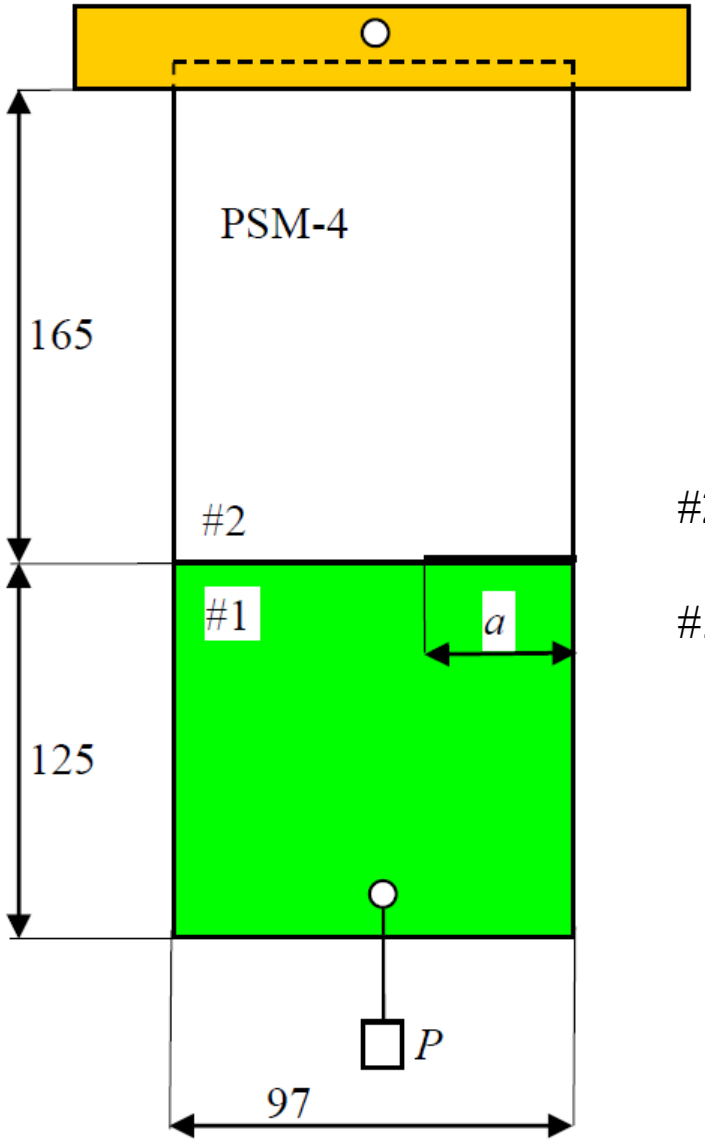

#2 polyurethane PSM-4 $E_2 = 4$ MPa $\nu_2 = 0.5$

#1 steel $E_1 = 210000$ MPa $\nu_1 = 0.3$

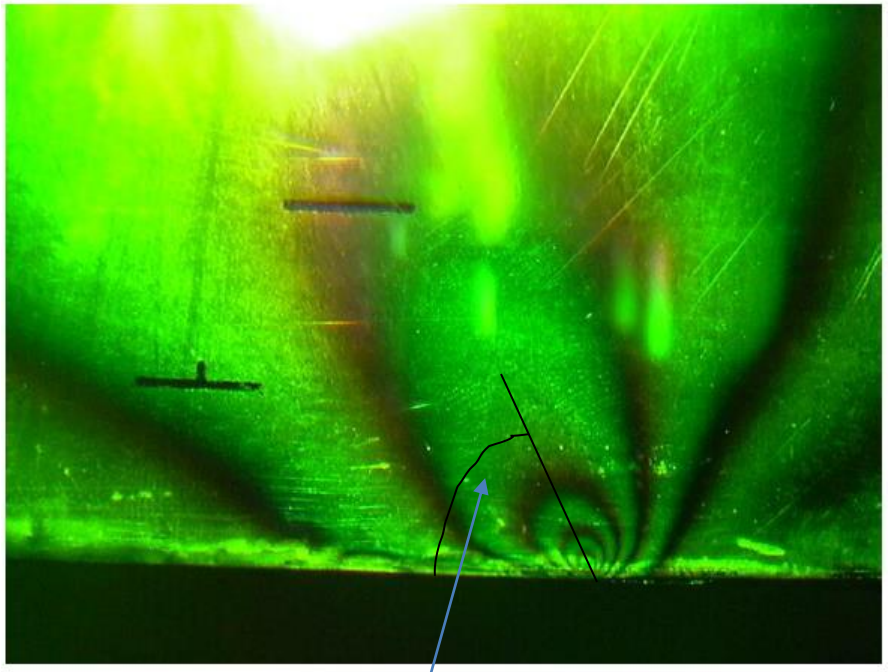

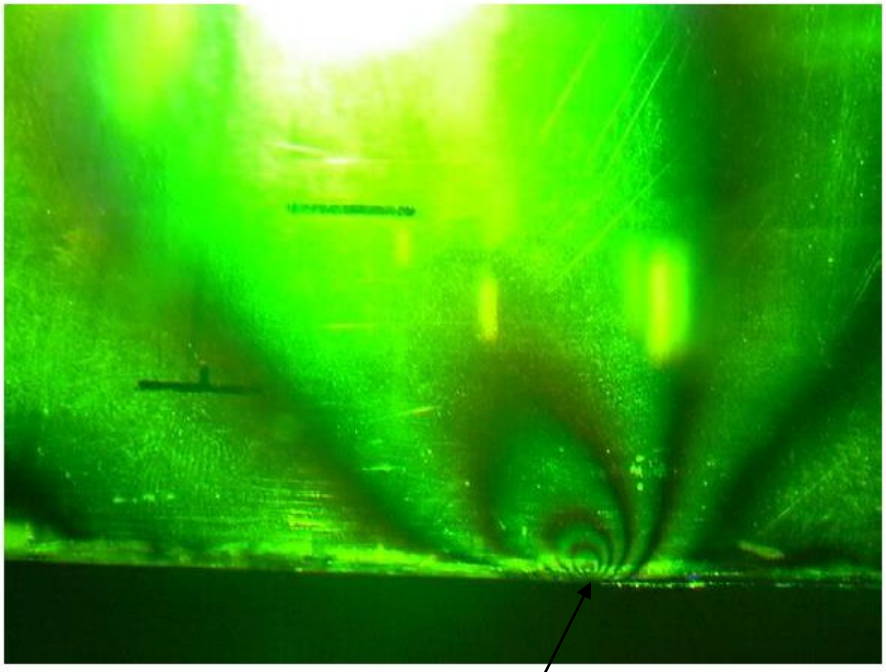

dark field – integral fringes are dark

Polarizer and analyzer have crossed polarizing planes.

bright field – integral fringes are bright

Polarizer and analyzer have parallel polarizing planes.

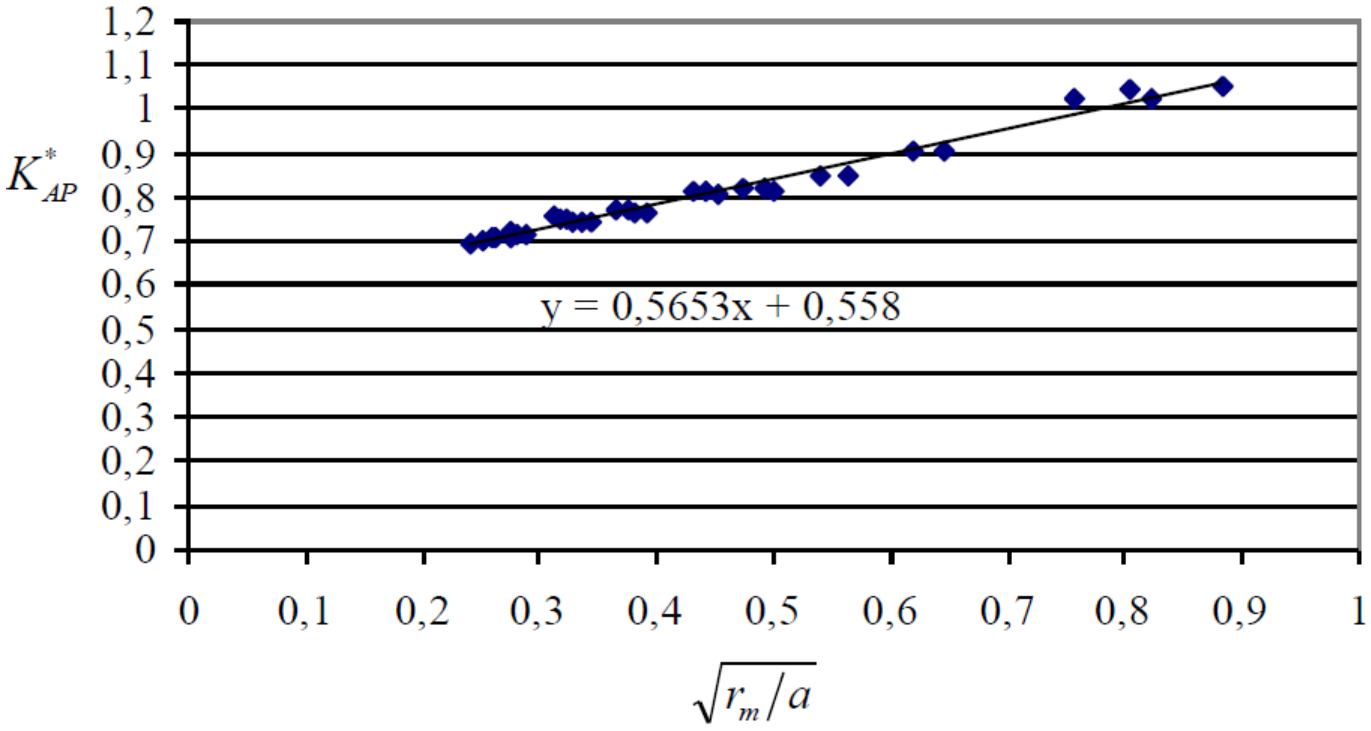

$$K^* = [(K_1 \sin \Theta_m^0 + 2K_2 \cos \Theta_m^0)^2 + (K_2 \sin \Theta_m^0)^2]^{1/2}$$

*K** greater than the theoretical one, as errors resulted when establishing the value θ_m^o

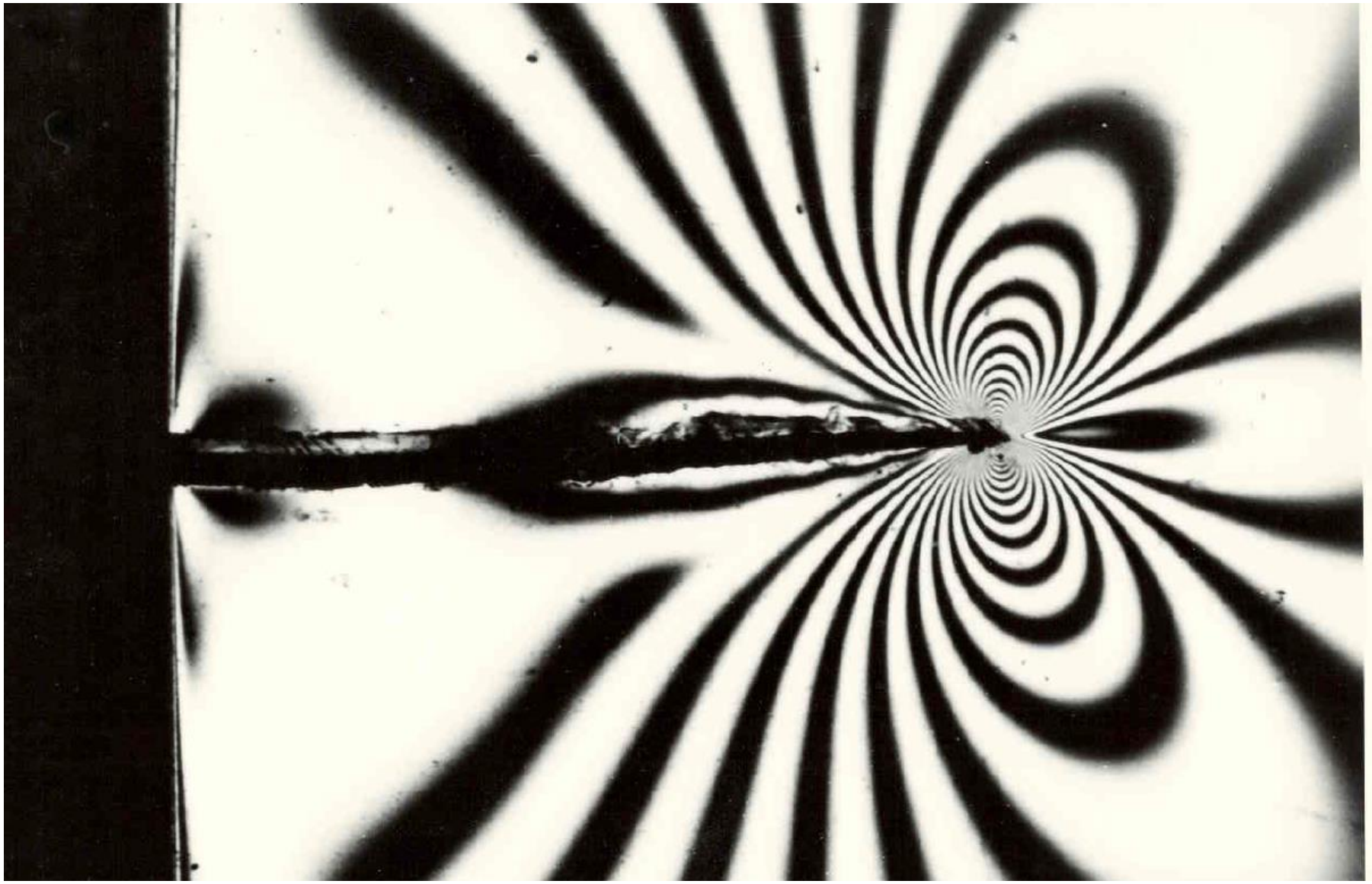

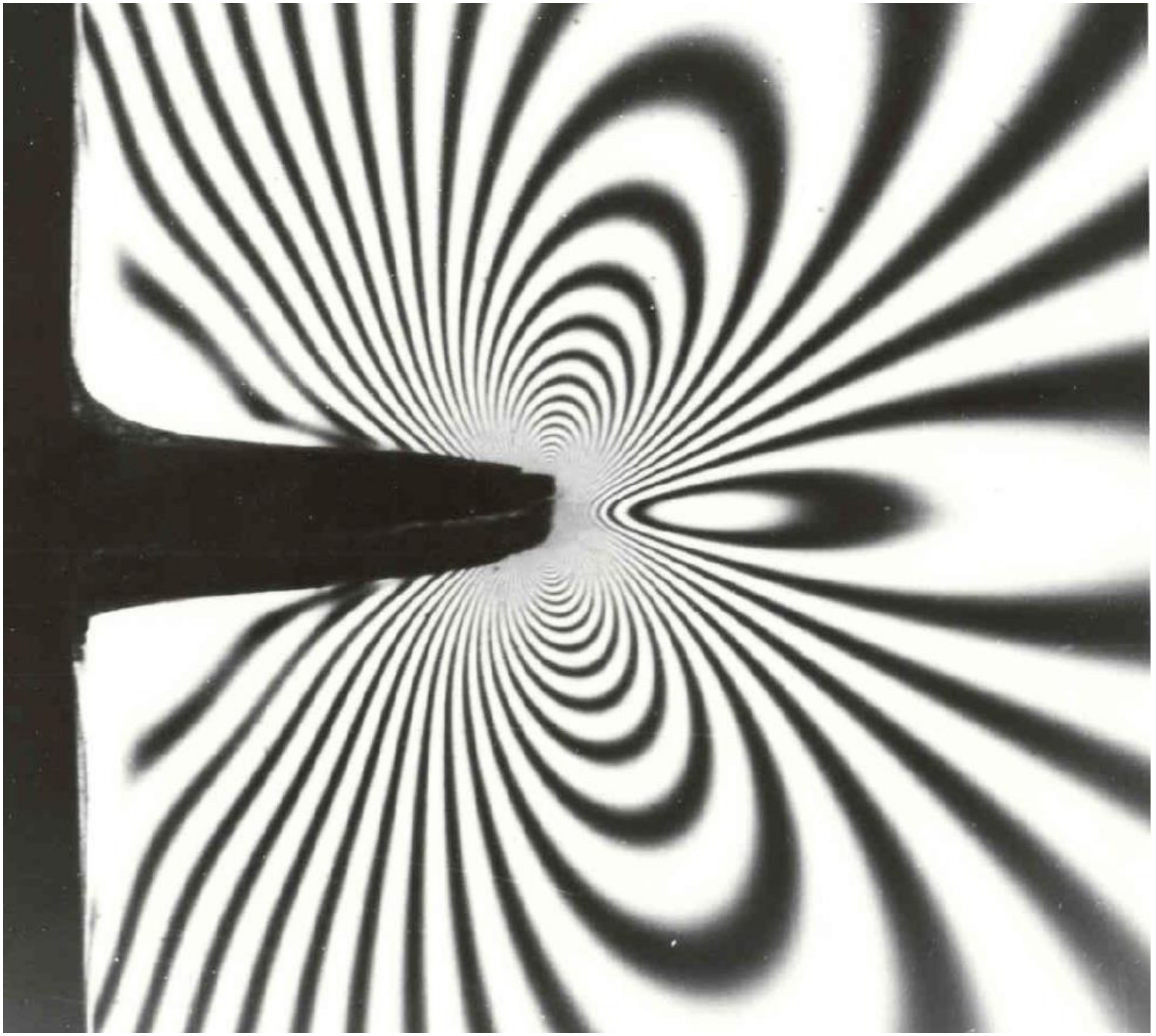

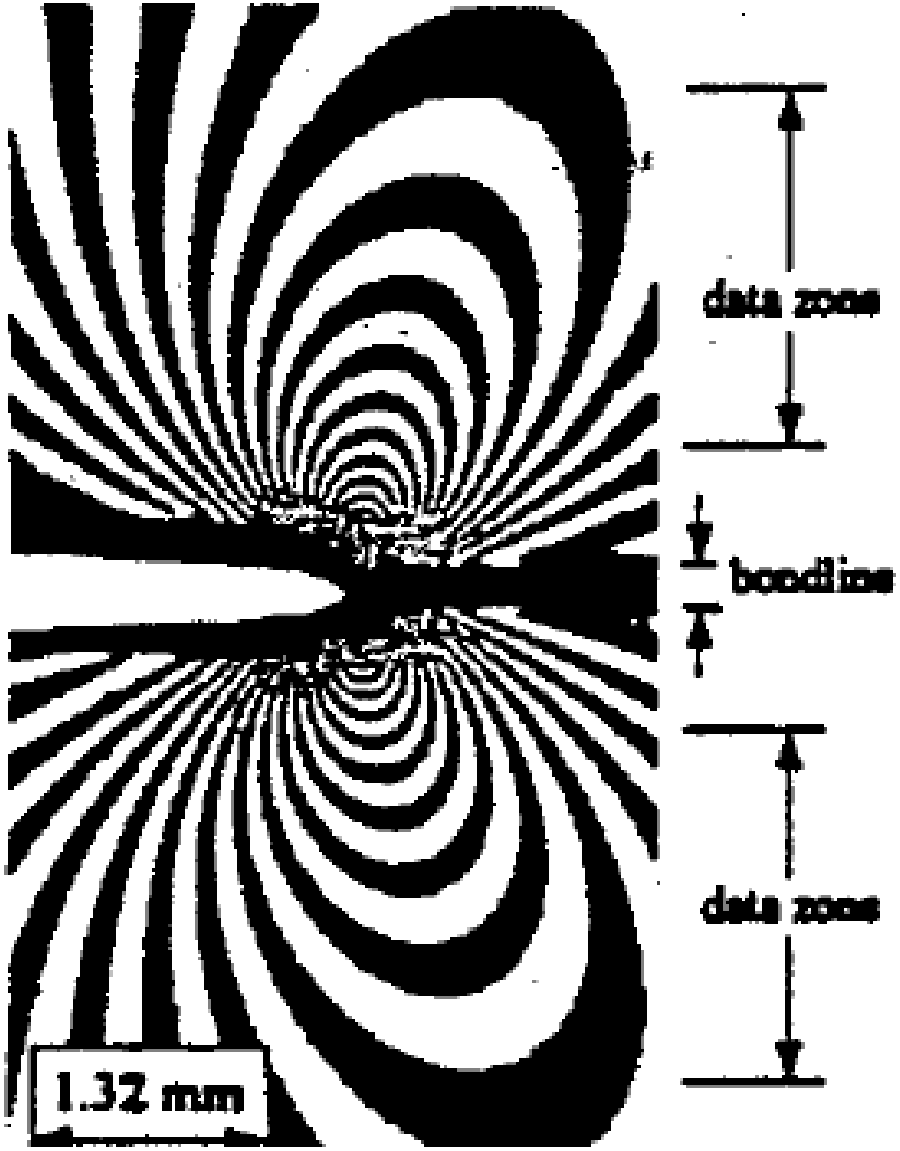

White field (integral fringes are white)

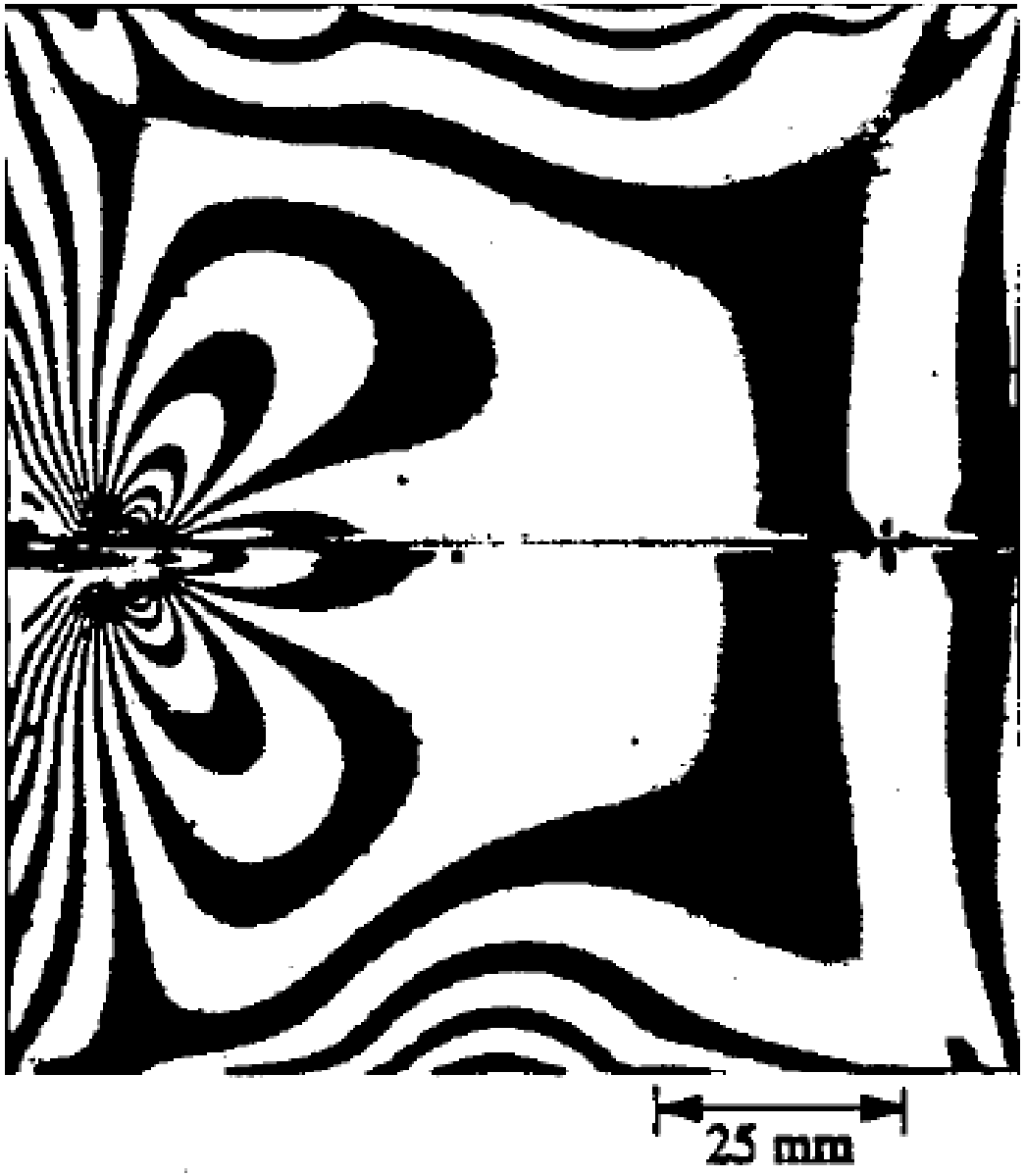

Dark field (integral fringes are dark)

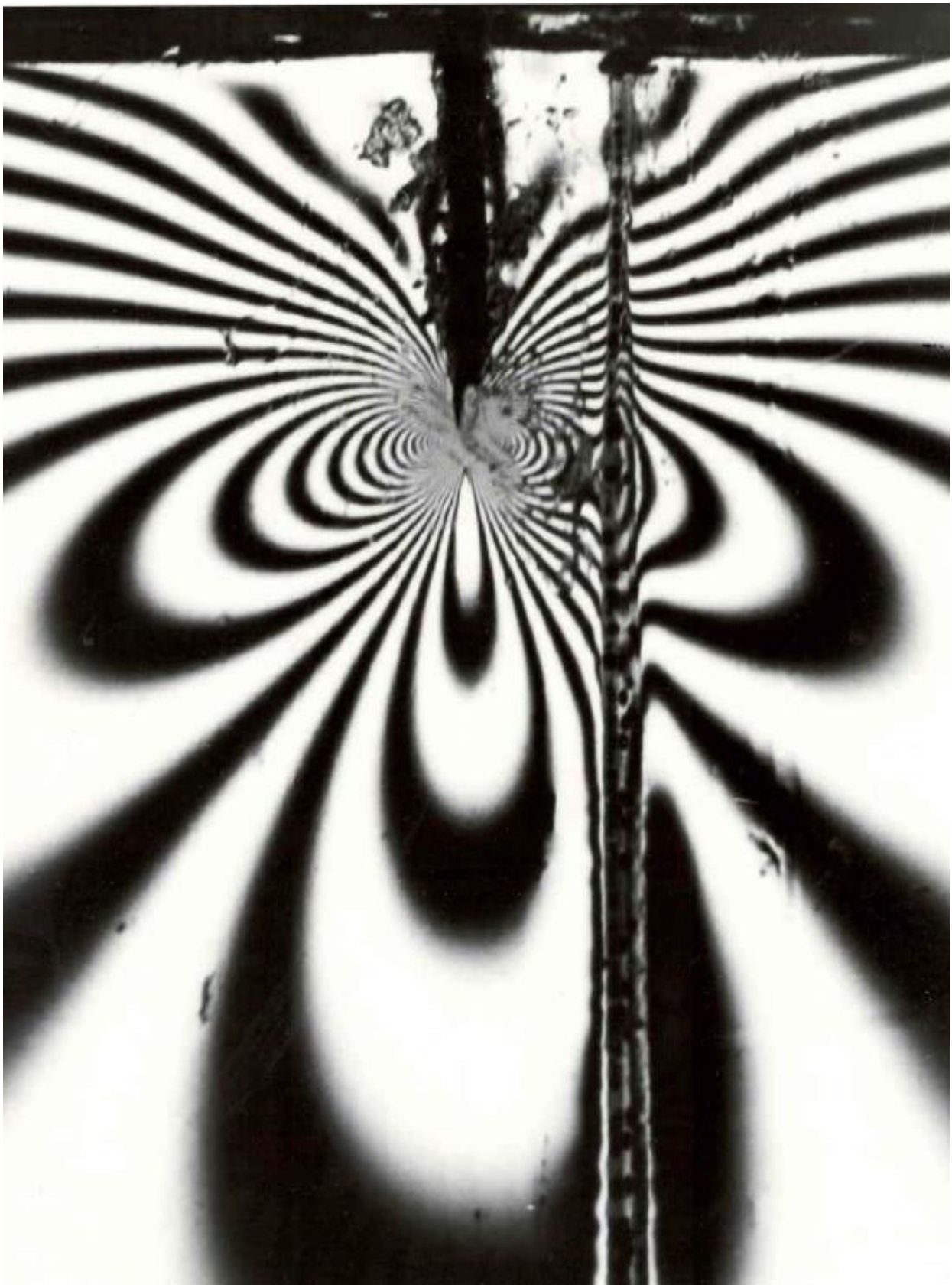

3D (frozen stress) Photoelasticity

- The frozen stress method was introduced by Opel (1936). It involved utilizing the fact that some photoelastic materials exhibited essentially diphase mechanical response to change in temperature.
- Stress freezing materials possess the special characteristic of possessing a temperature, T_c, called the critical temperature, which is in the neighborhood of the glass transition temperature of the material.
- Material will be slightly viscoelastic at room temperature, but when heated above T_c, the viscous coefficient vanishes and the material becomes linearly elastic with an *elastic modulus of about one six hundredth* of its room temperature value and the *material becomes incompressible*.
- Furthermore*, the stress fringe sensitivity of the material above T_c increases to a value of some 20 times the value at room temperature*.
- Then, upon unloading, fringe recovery will be small due to the relatively low fringe sensitivity at room temperature, and the fringes produced above T_c will be retained along with the deformations but no live stress results.
- Consequently the model may be sliced into *thin slices and analyzed as in two dimensional photoelasticity, but with the three dimensional effect embedded in the fringes*.

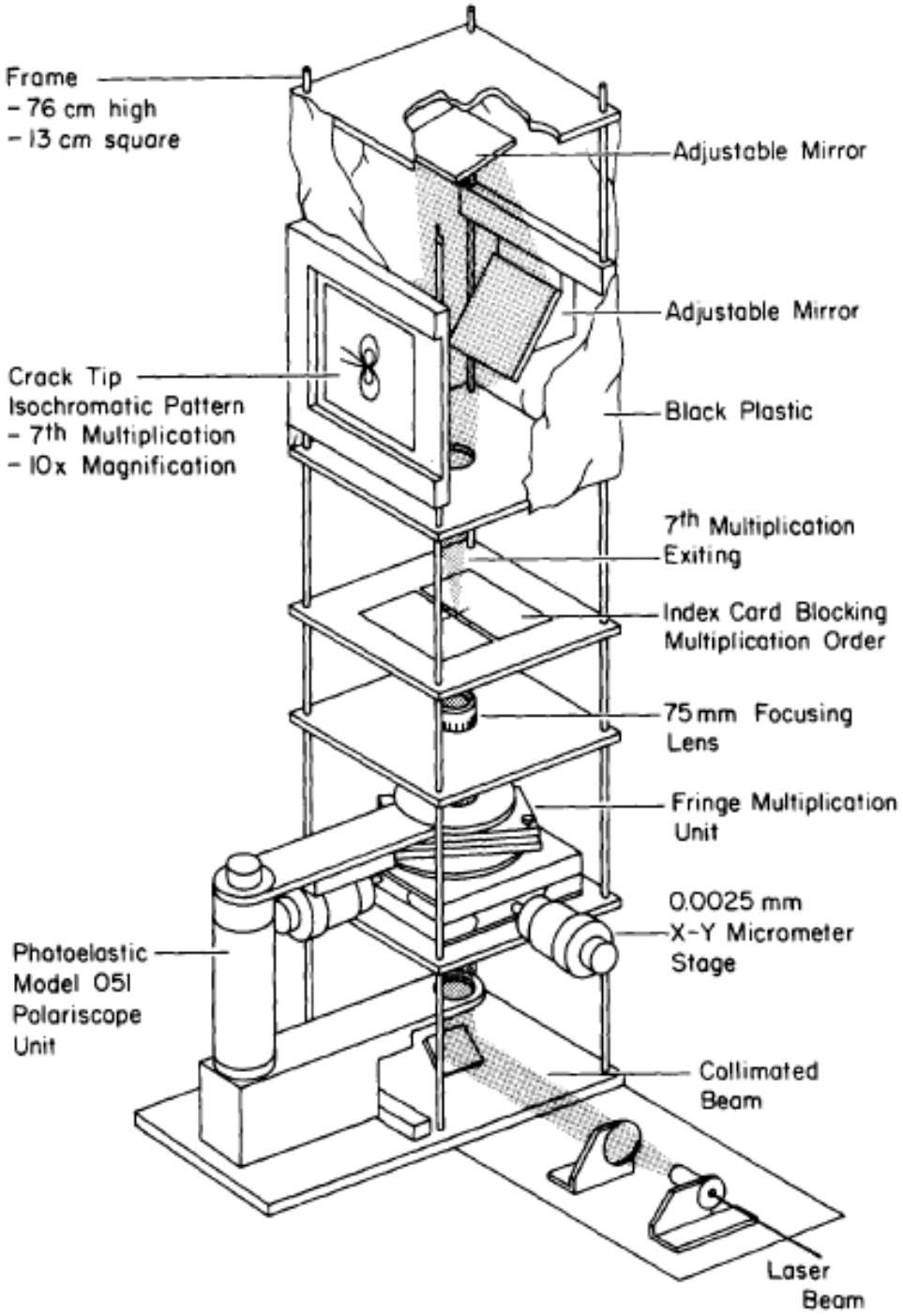
Frame
- 76 cm high
- 13 cm square
Adjustable Mirror
Adjustable Mirror
Crack Tip
Isochromatic Pattern
- 7th Multiplication
- 10x Magnification
Black Plastic
7th Multiplication
Exiting
Index Card Blocking
Multiplication Order
75 mm Focusing
Lens
Fringe Multiplication
Unit
0.0025 mm
X-Y Micrometer
Stage
Photoelastic
Model 051
Polariscope
Unit
Collimated
Beam
Laser
Beam

Large volumes of particulate composites are finding use in many applications in the commercial and military transportation industry.

One of these is solid propellant, which consists of hard polyhedral particles embedded in a soft rubber matrix which stiffens at low temperatures. The presence of defects, mainly cracks, in structures composed of these materials has become important as a result of efforts to extend the life of these structures for economic reasons.

When a crack grows in such a material, the matrix ahead of the crack tip stretches, separating into strands and producing severe blunting and moving the hard particles above and below the crack plane until the crack breaks the strands to advance through the stretch zone.

This blunt-growth-process is repeated, producing a highly non-linear phenomena. *At very low temperatures, the stretching of the matrix is suppressed, producing an embrittling effect.*

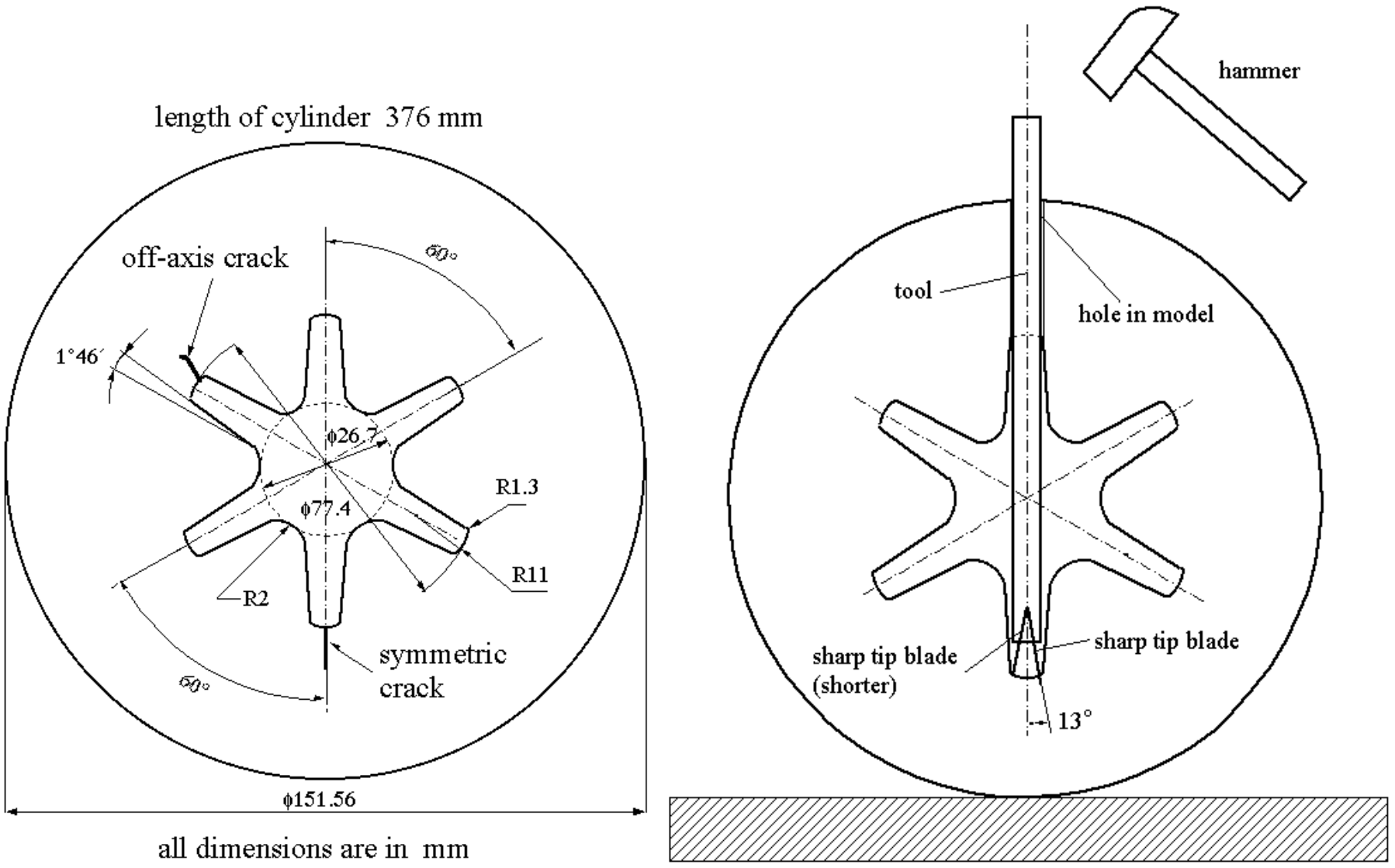

All test models were cast at Measurements Group (Raleigh, NC) in molds provided by Virginia Tech using PLM-4BR stress freezing material manufactured by Measurements Group.

Stress freezing procedure

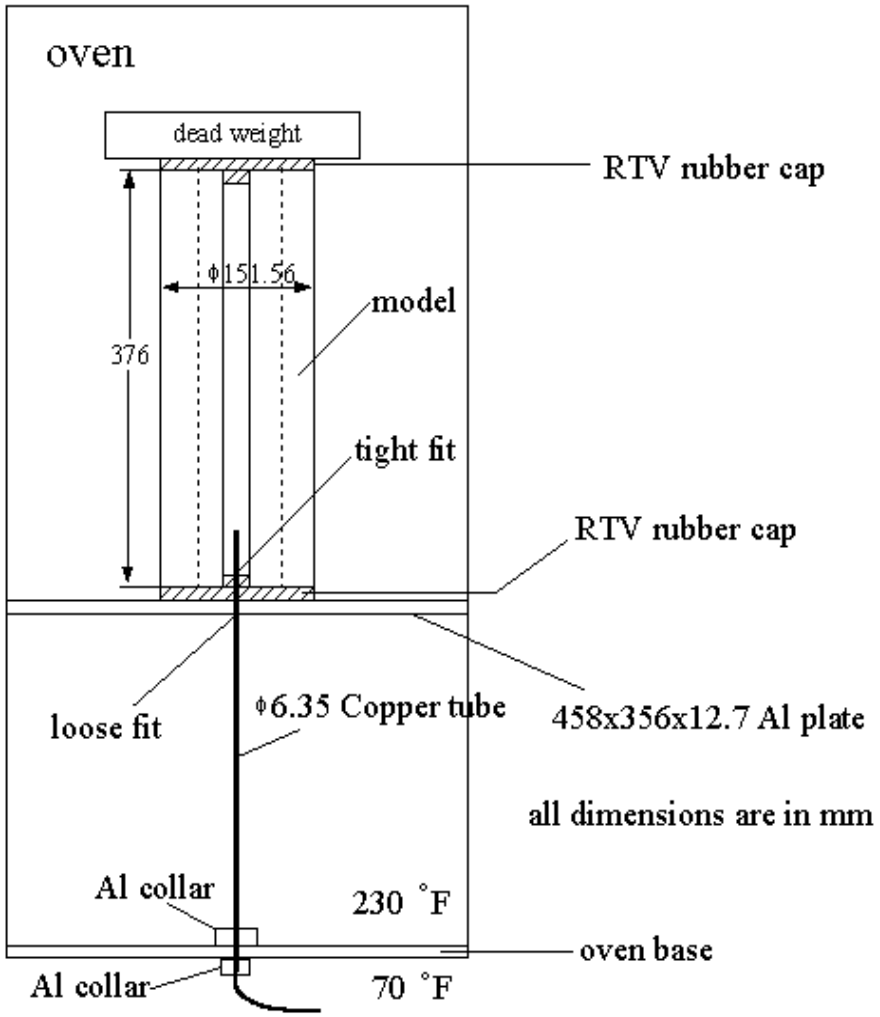

ϕ6.35 Copper tube to precision pressure gage

- The heating in the oven is done with about 3,9-4,4 °C/hour up to a temperature with about 6 °C above T_c (that is 110 °C).
- We keep the model in the oven at this temperature for about three hours to get an uniform temperature field. The cracks were grown under internal pressure above critical temperature to desired size (or assumed to be),
- Pressure was dropped to about 0,04-0,05 MPa and stress freezing was completed by cooling down with about 0,45 °C/hour when going through the critical temperature, and then faster.

The whole thermal cycle lasts for about one week.

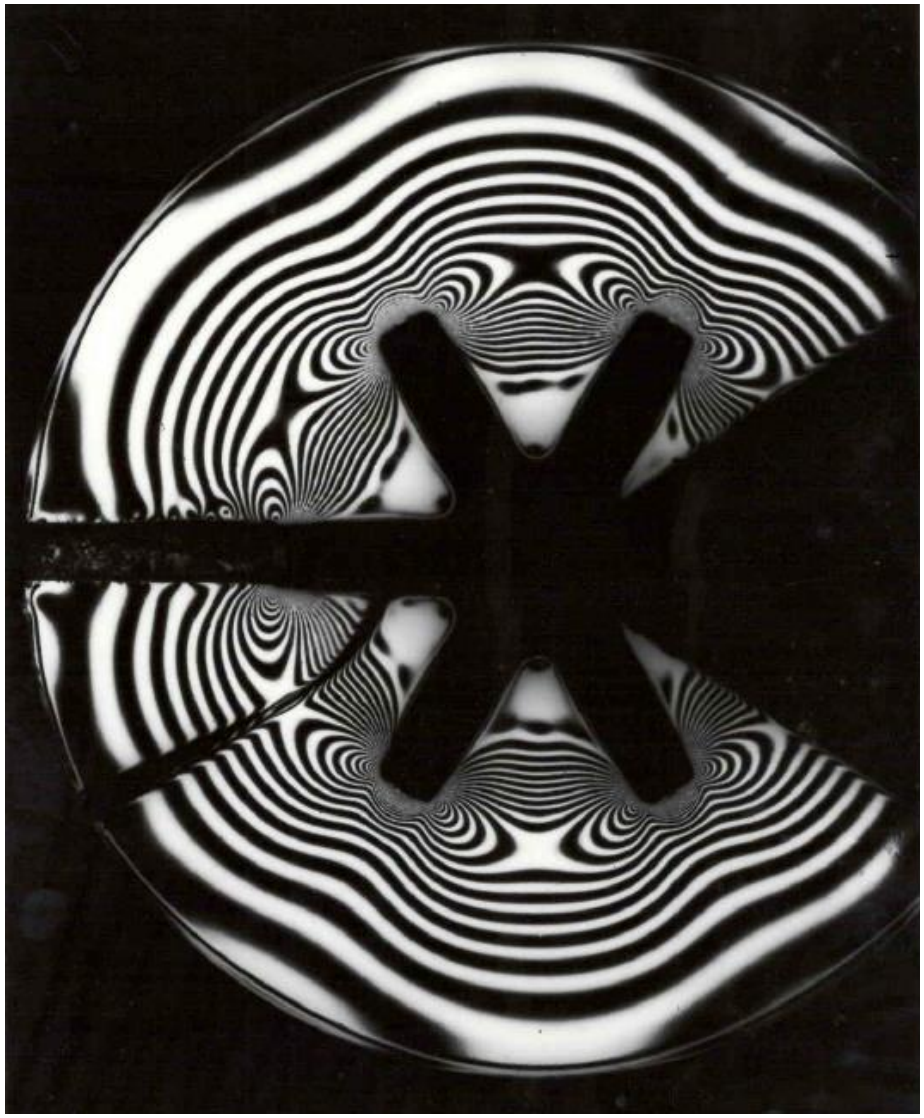

Dark field (integral fringes are dark)

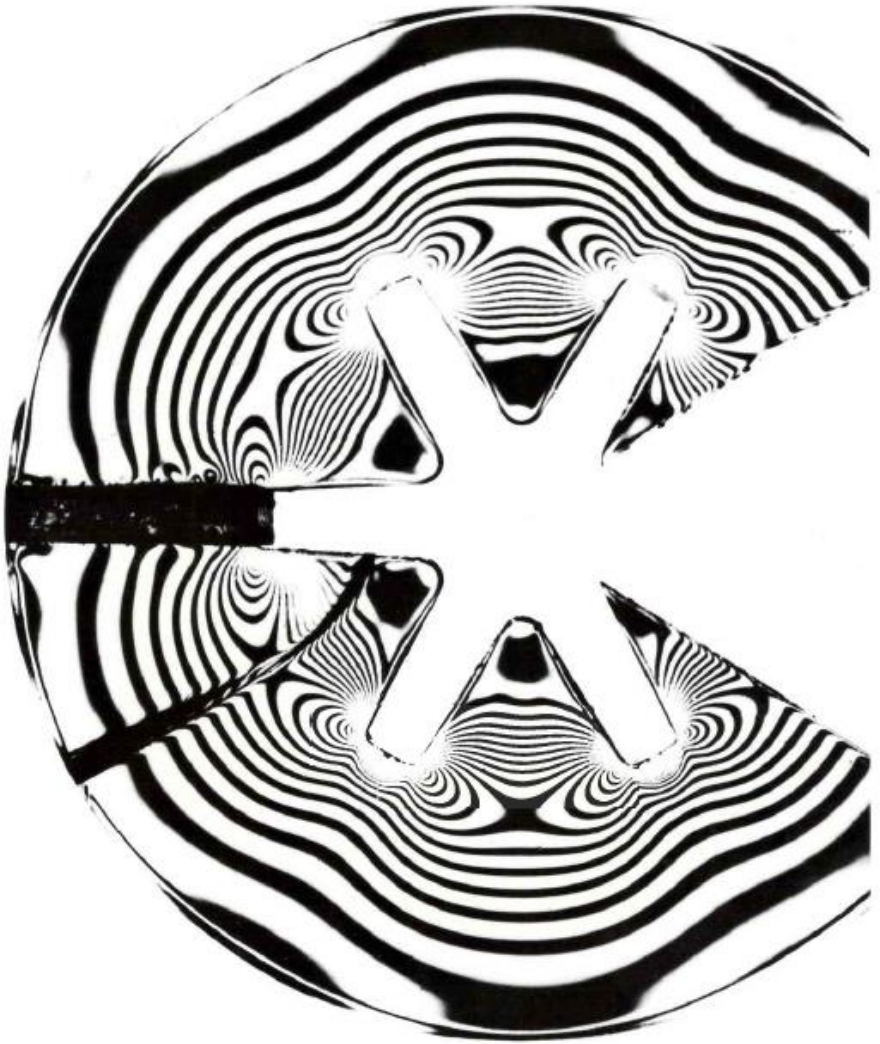

White field (integral fringes are white)

uncracked fin

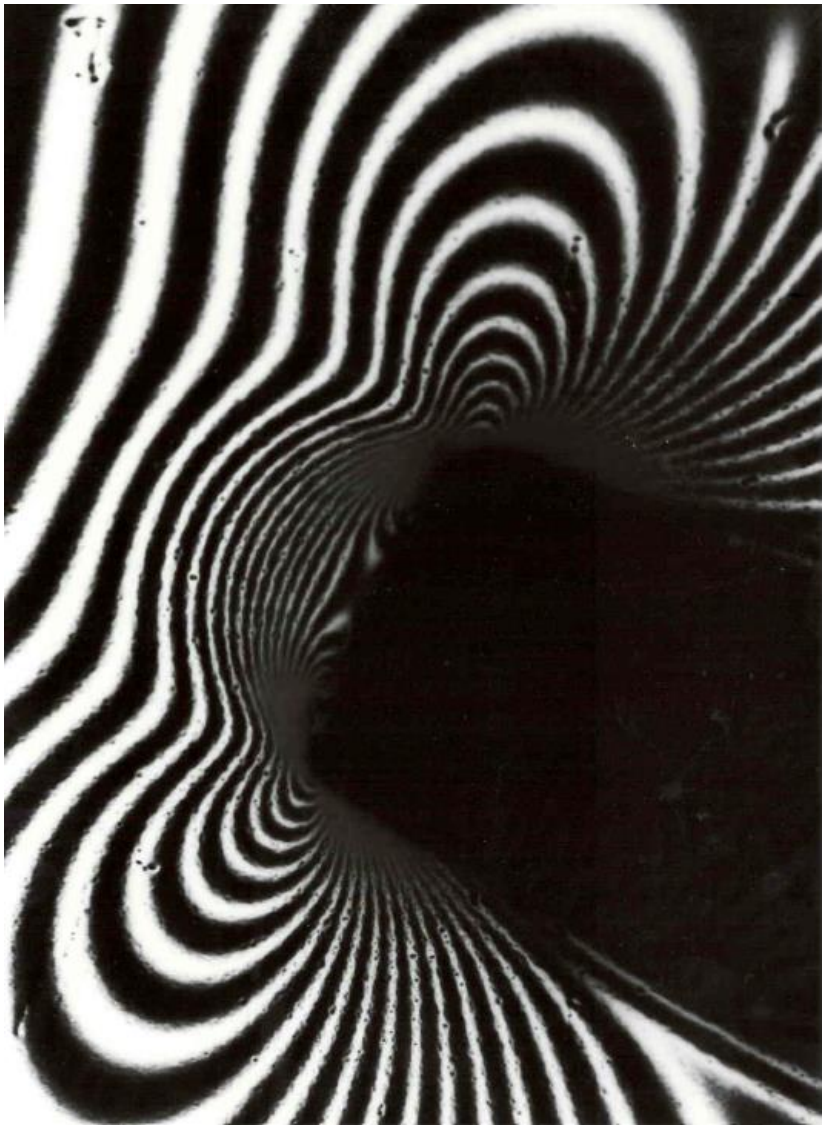

Dark field (integral fringes are dark)

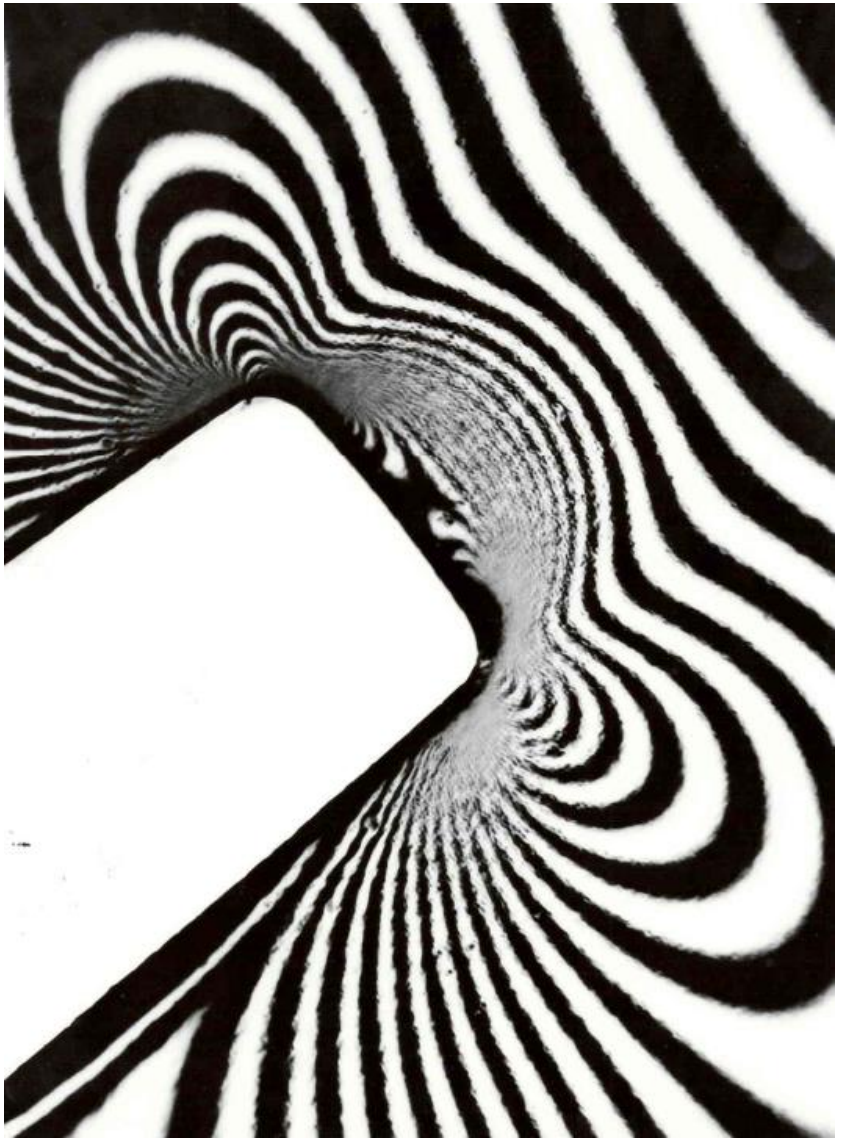

White field (integral fringes are white)

Not conclusive which position is “worse”

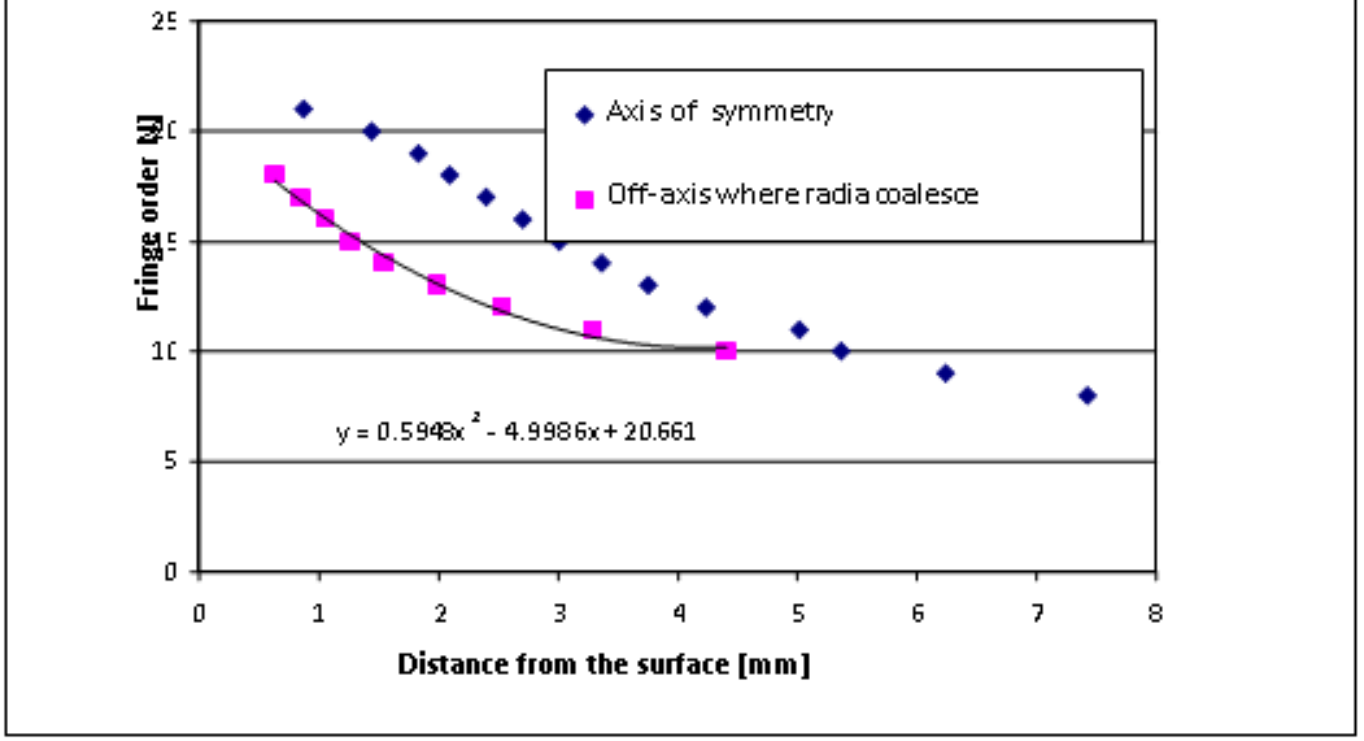

Pure bending calibration beam

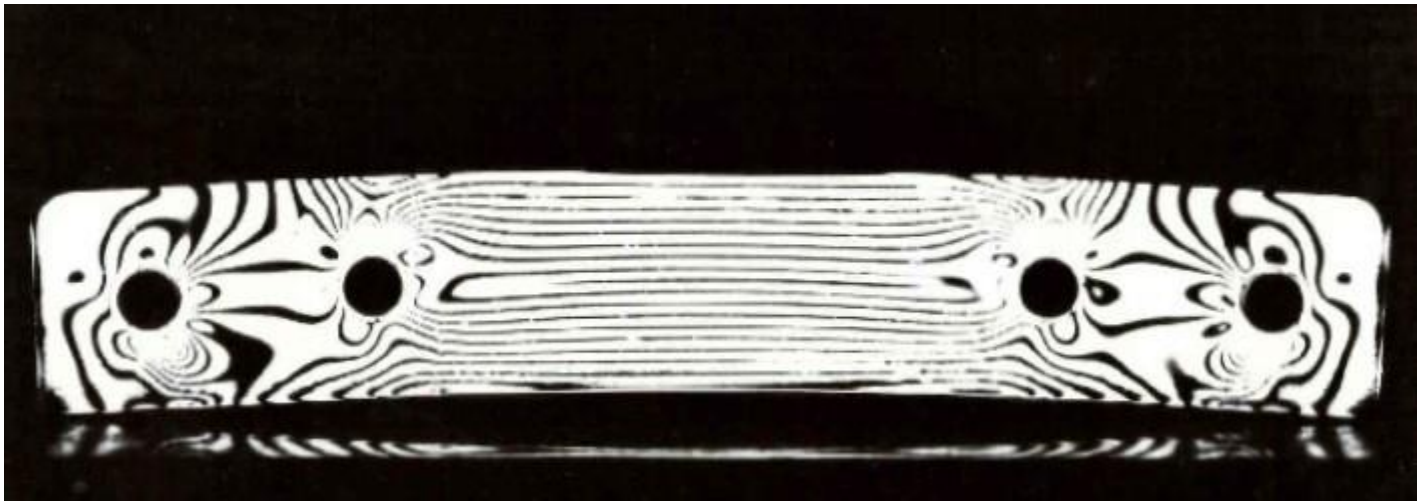

MIXED MODE ALGORITHM

The mixed mode algorithm was developed (see Fig. B-3) by requiring that:

$$\lim_{\substack{r_m \to 0 \\ \Theta_m \to \Theta_m^\circ}} \left\{ (8\pi r_m)^{1/2} \frac{\partial(\tau_{nz}^{max})}{\partial \Theta} (K_1, K_2, r_m, \Theta_m, \tau_{ij}) \right\} = 0 \tag{4}$$

which leads to:

$$\left(\frac{K_2}{K_1}\right)^2 - \frac{4}{3}\left(\frac{K_2}{K_1}\right) cot 2\Theta_m^\circ - \frac{1}{3} = 0 \tag{5}$$

By measuring $\Theta_{m_j}^\circ$ which is approximately in the direction of the applied load, K_2/K_1 can be determined.

Then writing the stress optic law as:

$$\tau_{nz}^{max} = \frac{fn}{2t} = \frac{K_{AP}^*}{(8\pi r)^{\frac{1}{2}}}$$

one may plot $\frac{K_{AP}^* \sqrt{Q}}{p\sqrt{\pi a}}$ vs. $\sqrt{r/a}$ as before, locate a linear zone and extrapolate to $r = 0$ to obtain K^*. Now K^*, may be written as:

$$K^* = [(K_1 sin\Theta_m^\circ + 2K_2 cos\Theta_m^\circ)^2 + (K_2 sin\Theta_m^\circ)^2]^{\frac{1}{2}} \tag{6}$$

After cooling, thin slices (around 1 mm thickness) were removed normal to the crack front and analyzed at maximum crack depth and in certain locations along the crack front, finally obtaining the values of the normalized stress intensity factors by using a two parameter algorithm valid within the linear elastic fracture mechanics (LEFM) constrains.

The *symmetric* crack, remained planar during growth and exhibited only pure Mode I values around the crack front. Moreover, it conformed to the definition of a **Class I** crack as described by Cotterell.

The second type of crack emanated from the point of confluence of the main fin tip radius (R11 mm) with a much smaller edge radius (R1,3 mm). This latter crack was non-planar and generally contained, prior to turning, mixed mode SIF values at various locations along its border except near the fin surface where Mode I prevailed. These cracks, due to turning, grew in arbitrary directions until turning eliminated the shear mode effects and so were essentially **Class II** cracks, as described by Cotterell, grew until the shear modes were eliminated, after which the cracks grew as Class I cracks exhibiting pure Mode I loading. These latter cracks are referred to here as off-axis cracks and the present discussion will focus on these cracks.

In the present study all off-axis cracks were analyzed for SIF values by using dimensions of planar projections of the crack fronts as their semi-elliptical dimensions since the out-of-plane dimensions of the crack surfaces were small (except for river markings), and eventually disappeared with the shear modes during growth.

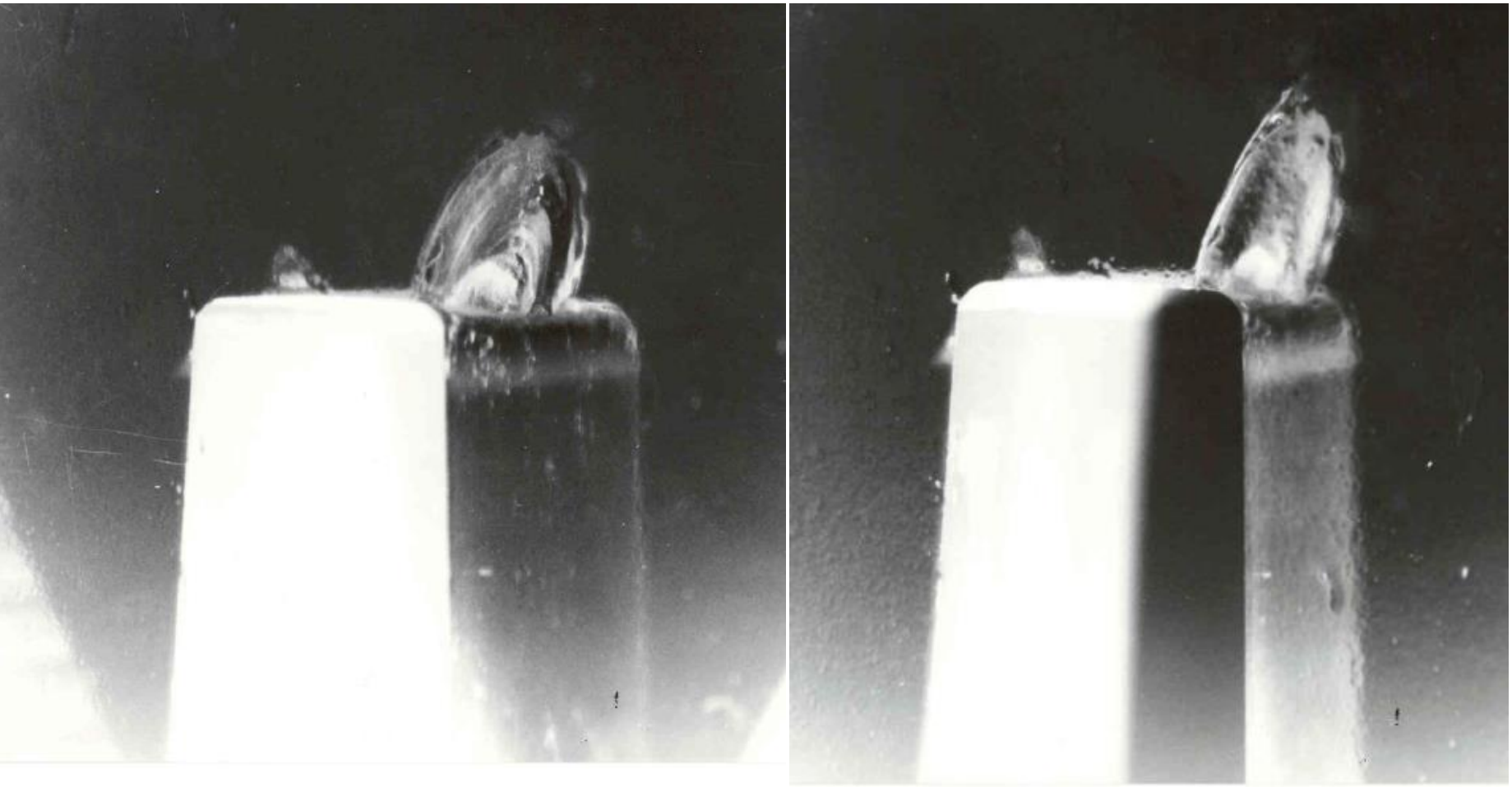

Crack surface non-planar while turning in eliminating shear modes

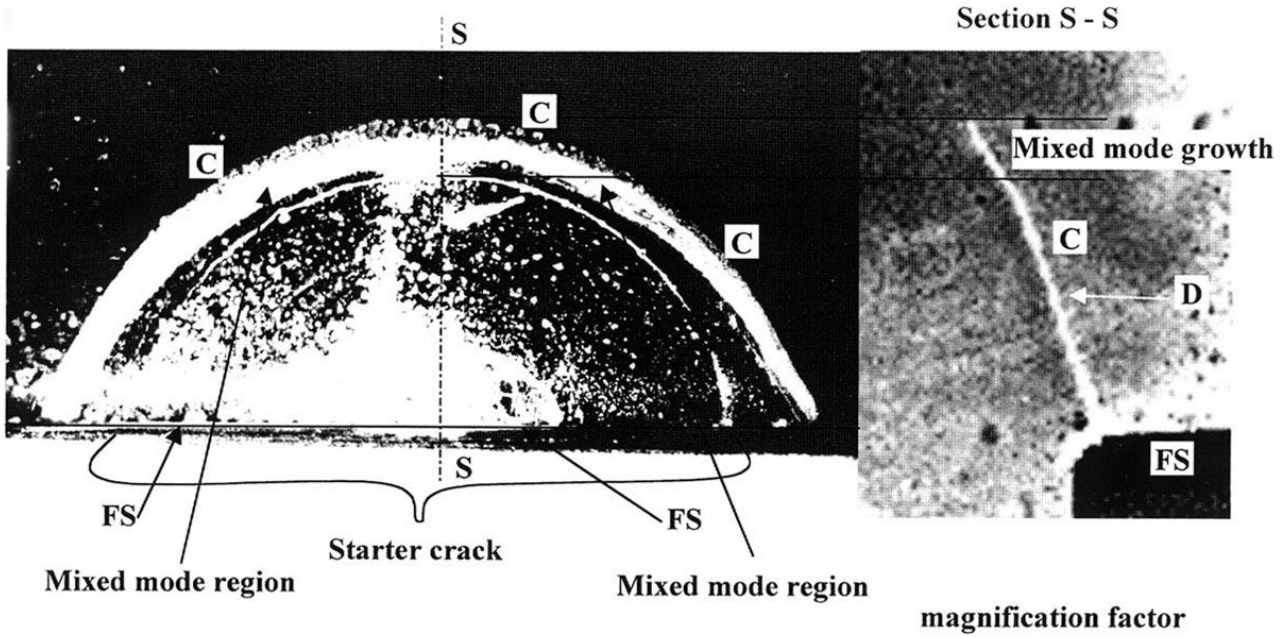

Model 4 Off-Axis Inclined Crack Showing Starter Crack and Final Crack Front

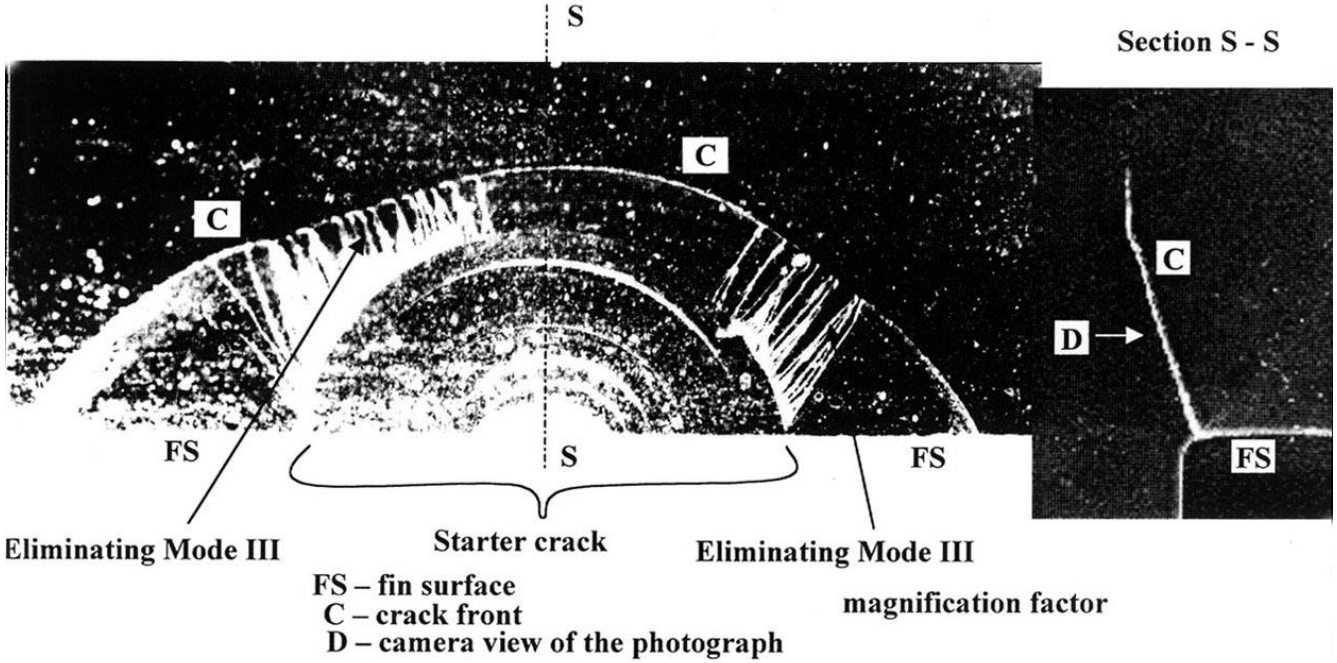

Model 8 Off-Axis Inclined Crack Showing Starter Crack and Final Mode I Crack Front

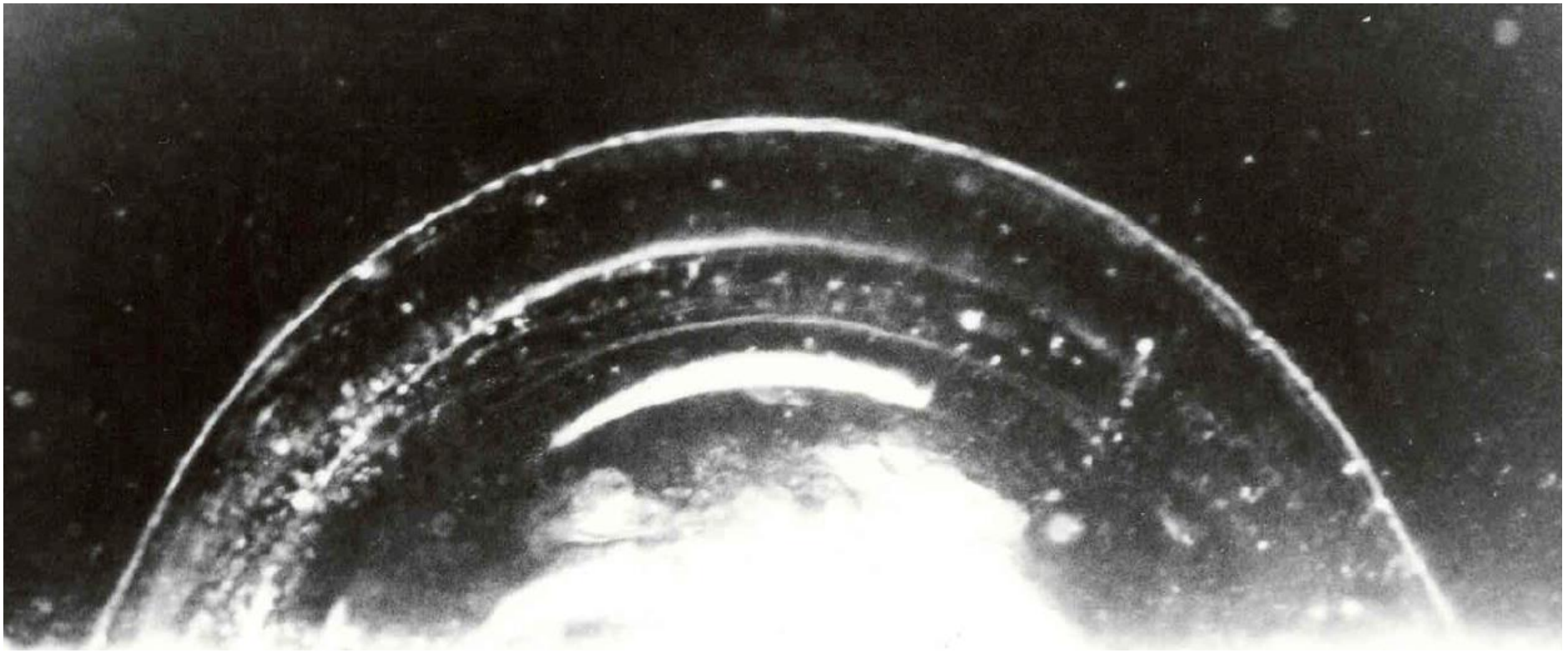

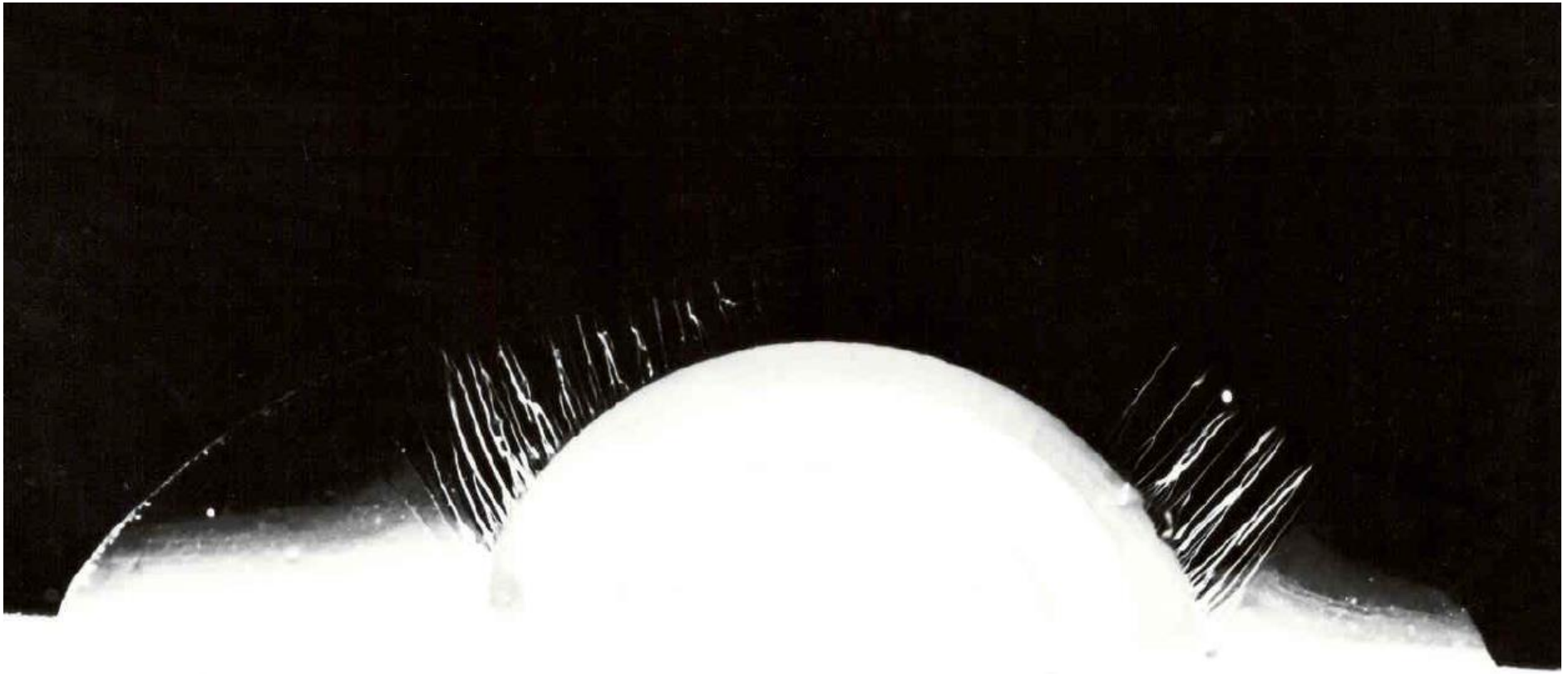

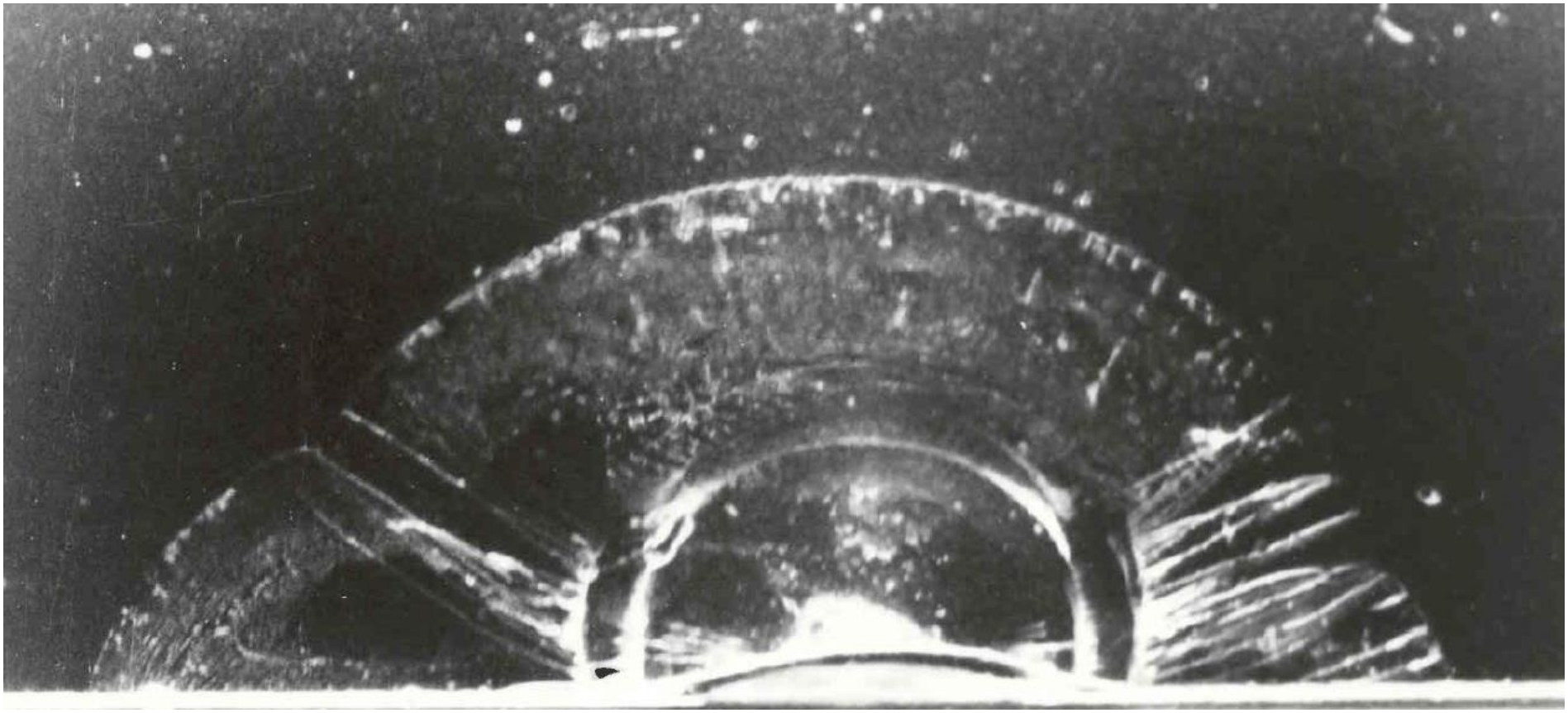

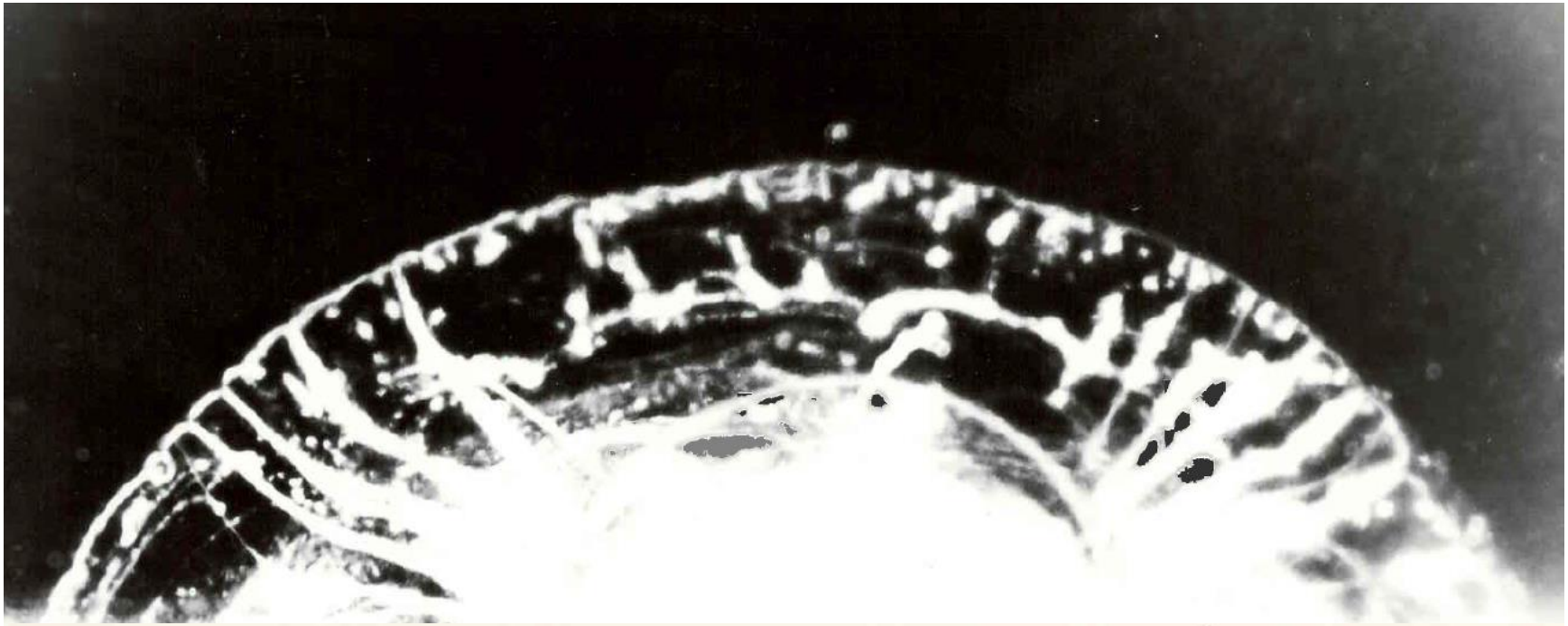

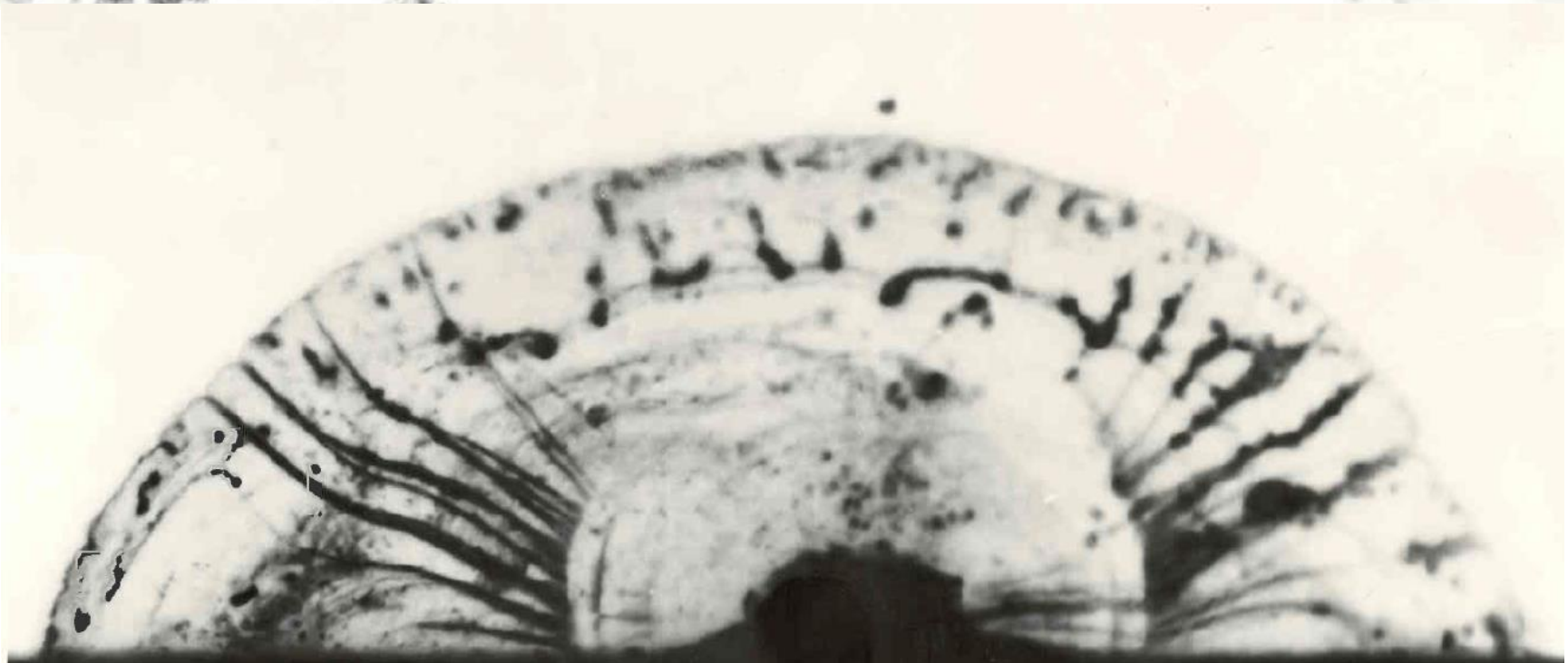

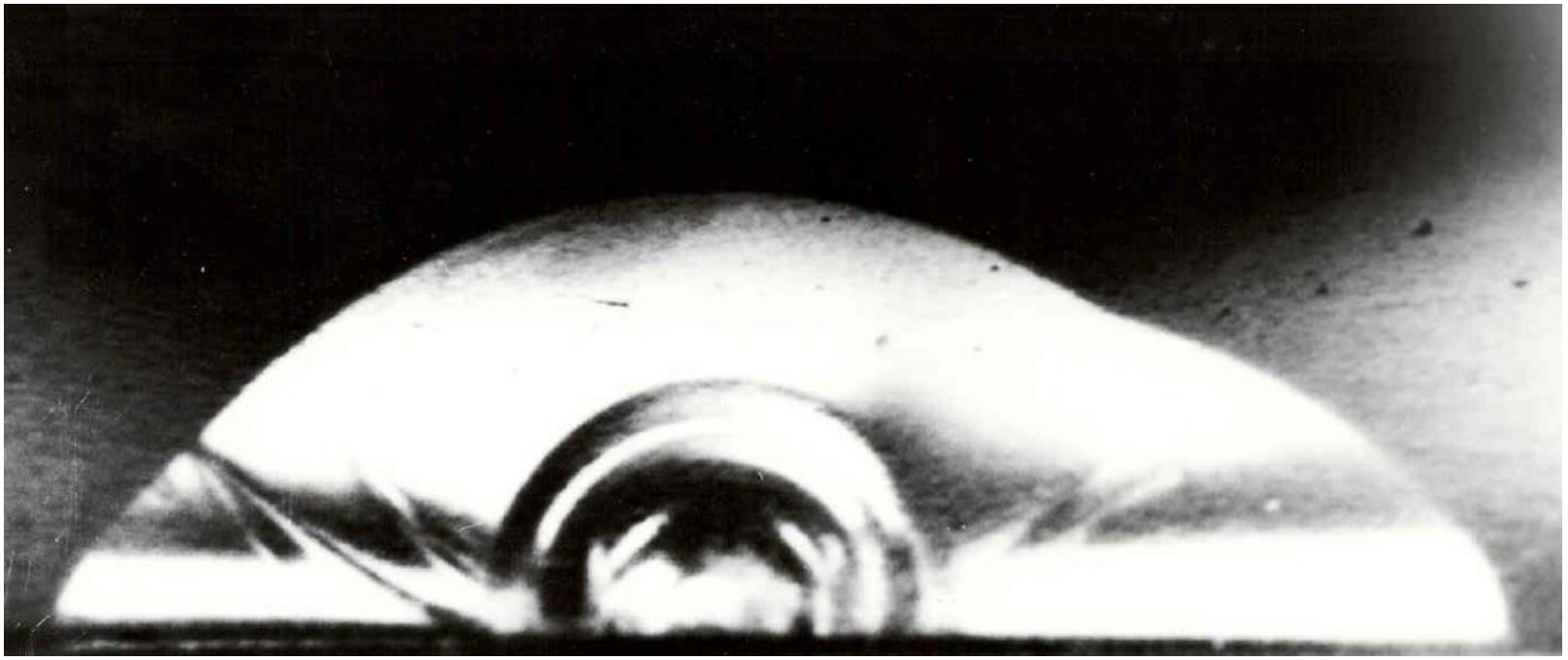

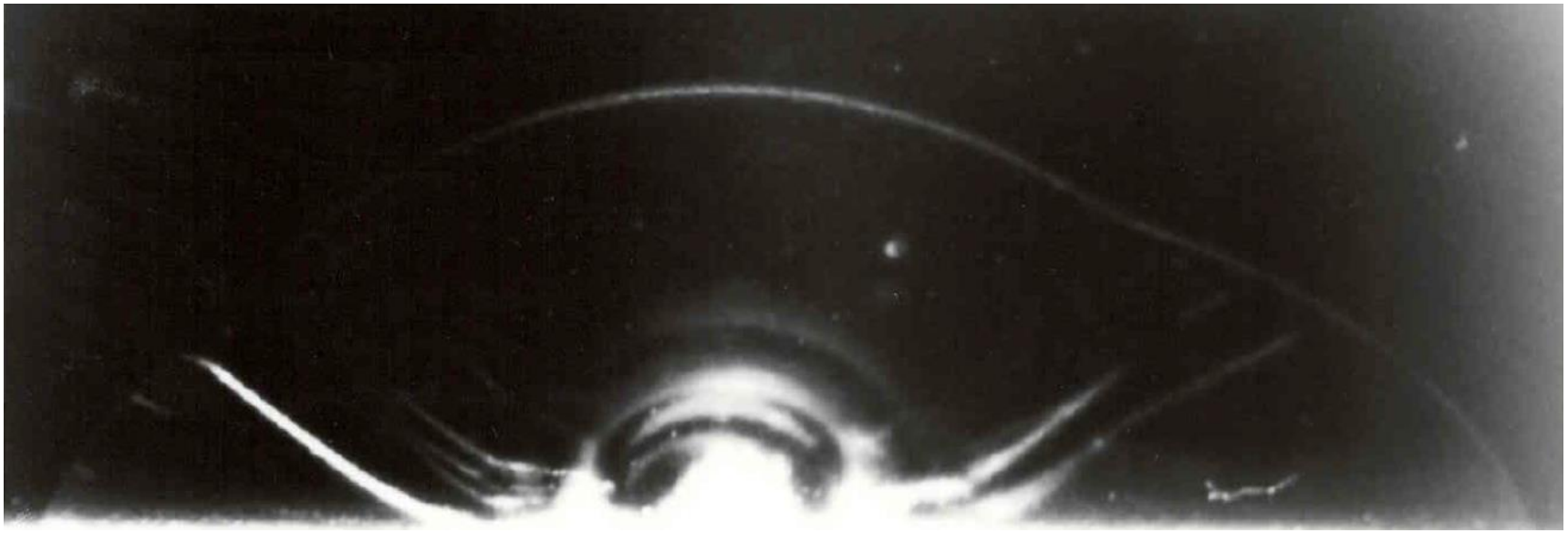

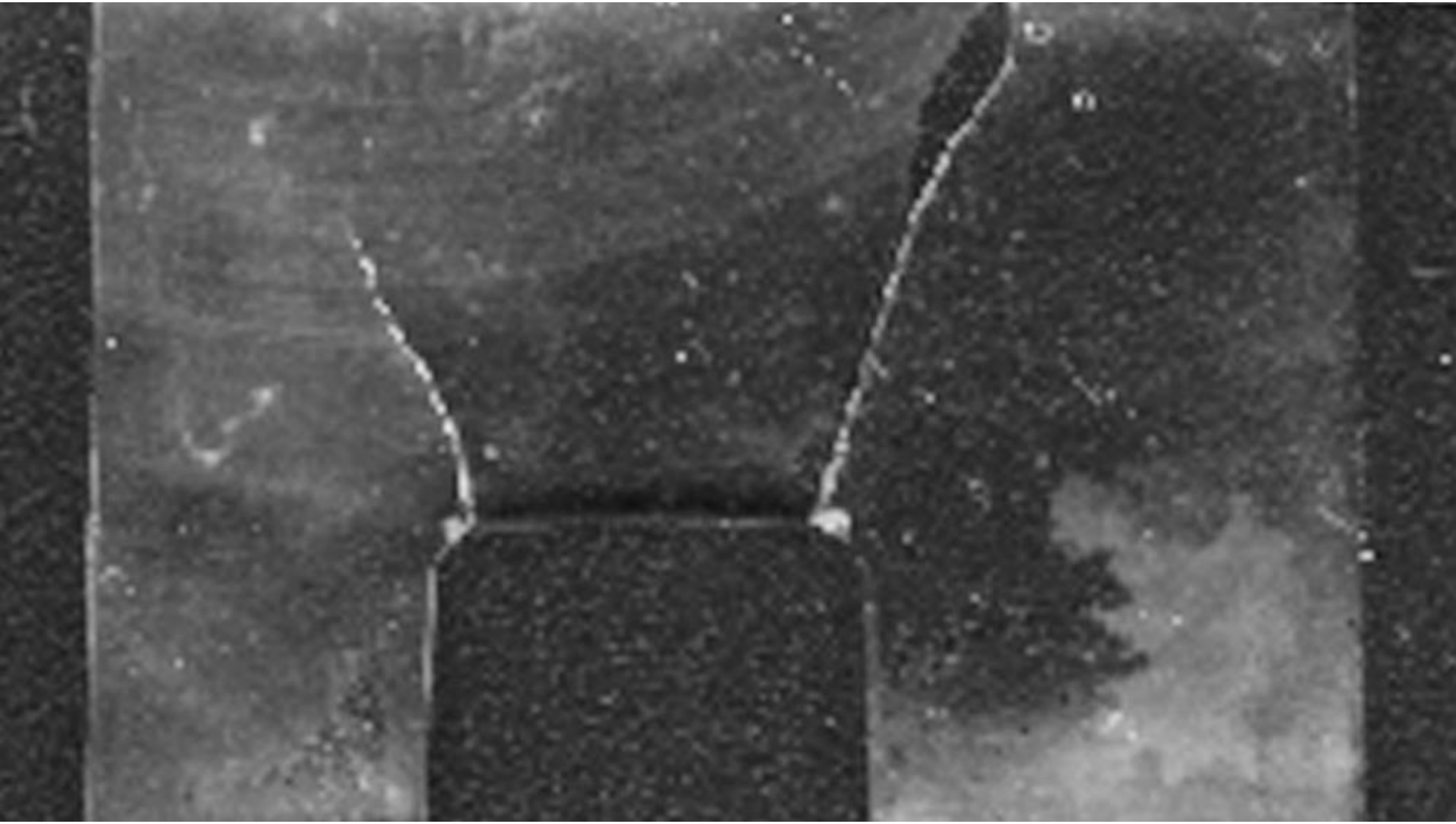

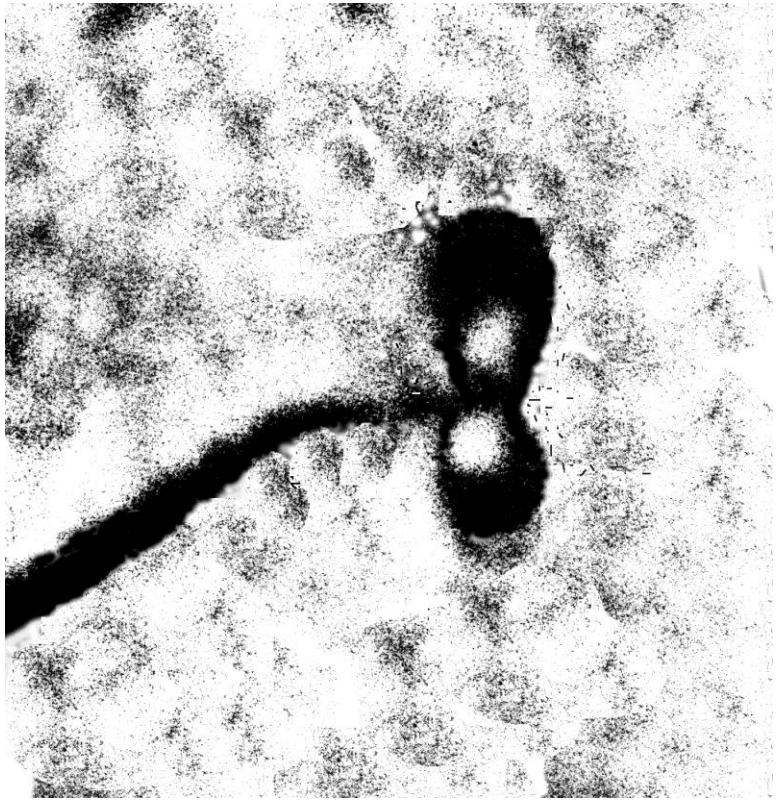

a)

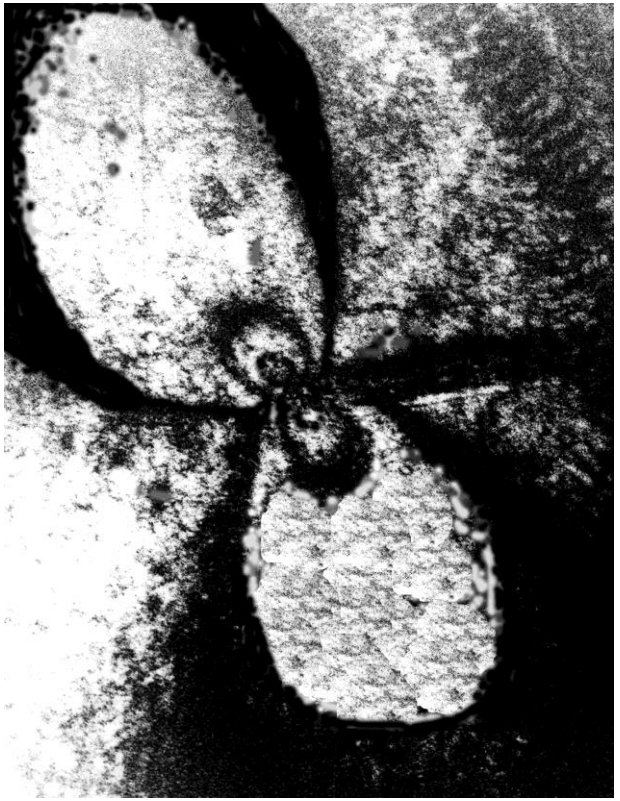

b)

Fringe at the tip of a turning crack; a) first order; b) third order multiplication.

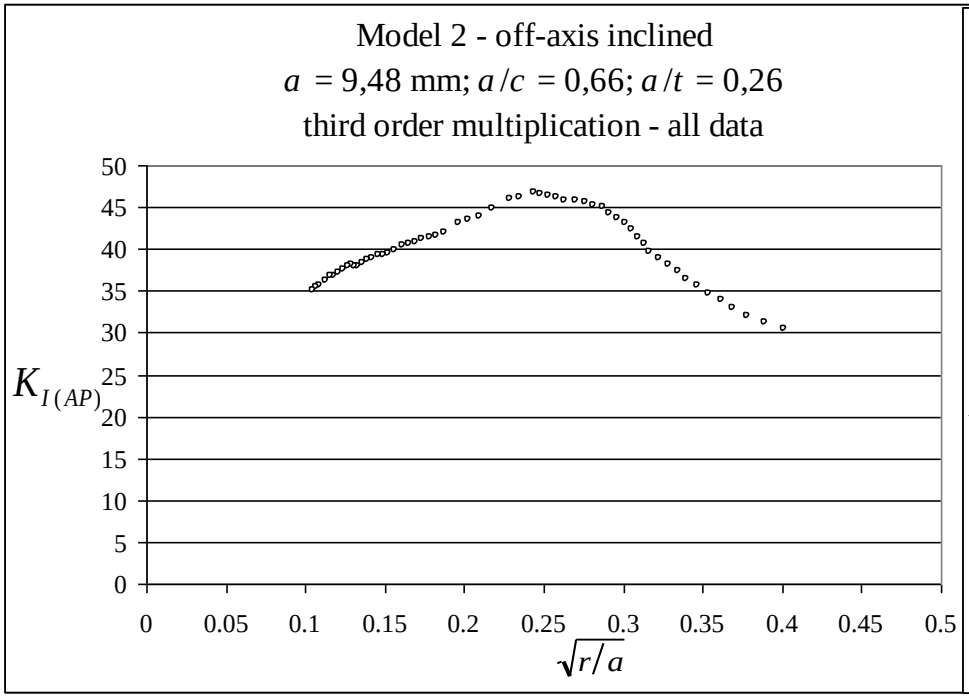
Model 2 - off-axis inclined
a = 9,48 mm; a/c = 0,66; a/t = 0,26
third order multiplication - all data
K I (AP)
√r/a
0
5
10
15
20
25
30
35
40
45
50
0
0.05
0.1
0.15
0.2
0.25
0.3
0.35
0.4
0.45
0.5

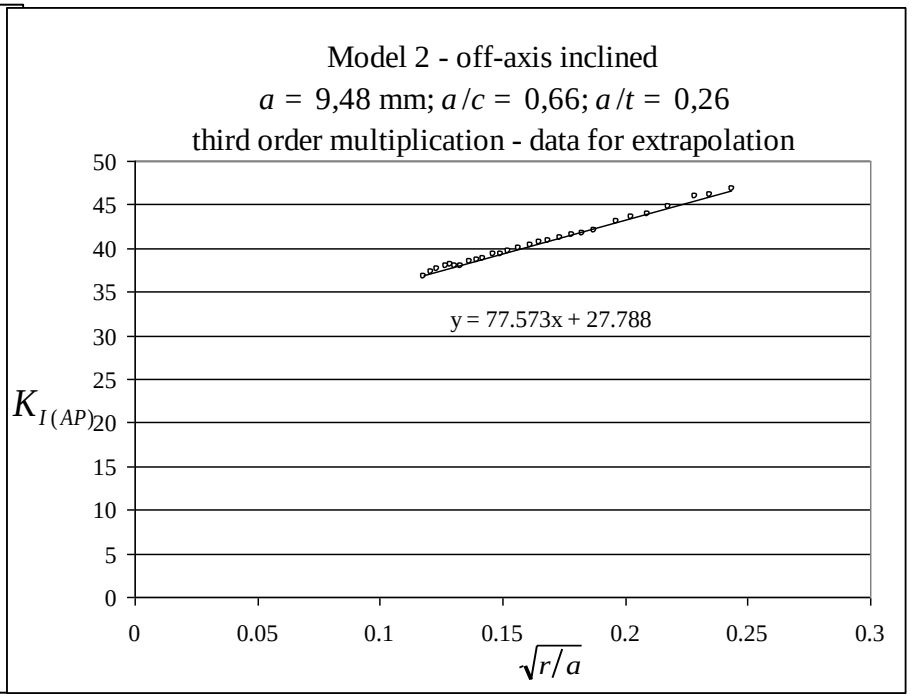
Model 2 - off-axis inclined
a = 9,48 mm; a/c = 0,66; a/t = 0,26
third order multiplication - data for extrapolation
y = 77.573x + 27.788
K I (AP)
√r/a
0
5
10
15
20
25
30
35
40
45
50
0
0.05
0.1
0.15
0.2
0.25
0.3

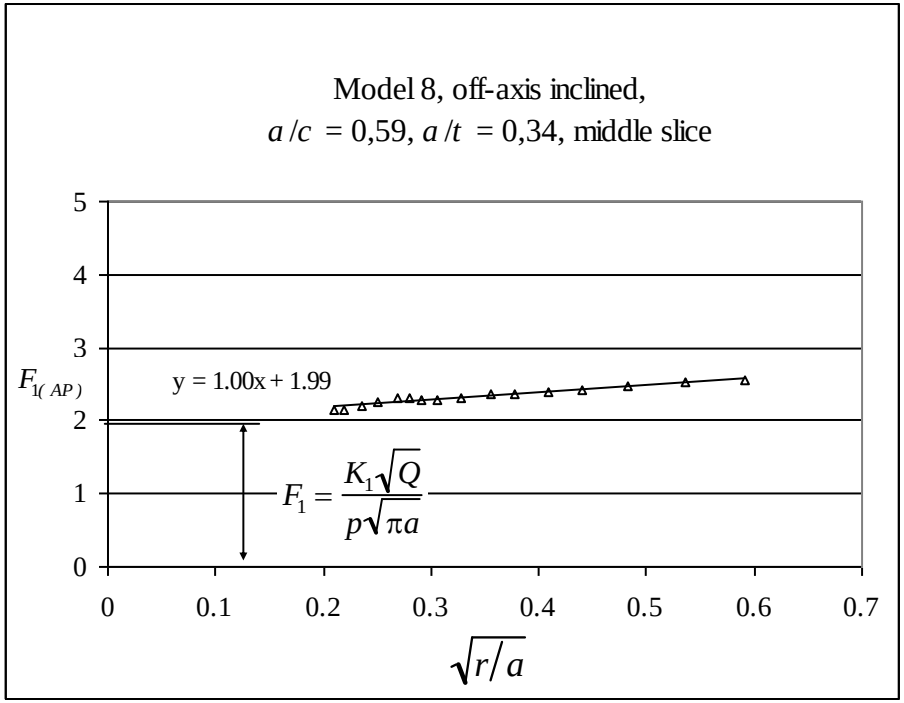
Model 8, off-axis inclined,
a/c = 0,59, a/t = 0,34, middle slice
y = 1.00x + 1.99
F1(AP)
F1 = K1√Q / p√πa
√r/a
0
1
2
3
4
5
0
0.1
0.2
0.3
0.4
0.5
0.6
0.7

Table 4. Normalized SIFs for different crack geometries.

Loads [a]	Crack Description [b] (dimensions in mm)	F_1 [c] middle slice
	Model 4	
	Off-axis inclined	
P = 88,97 N	a = 8,71 Δa = 2,18	F_1 = 1,90
p_{max} = 0,049 MPa	c = 11,15 Δc = 3,02	F_2 = 0,48
p_{sf} = 0,035 MPa	a/c = 0,78 a/t = 0,23	
	Model 8	
	Off-axis inclined	
P = 88,97 N	a = 12,50 Δa = 3,4	
p_{max} = 0,103 MPa	c = 21,1 Δc = 10,4	1,99
p_{sf} = 0,049 MPa	a/c = 0,59 a/t = 0,34	
	Model 6	
	Off-axis straight in	
P = 88,97 N	a = 11,60 Δa = 4,67	
p_{max} = 0,138 MPa	c = 17,00 Δc = 10,66	1,72
p_{sf} = 0,049 MPa	a/c = 0,68 a/t = 0,31	
	Off-axis straight in	
	a = 11,23 Δa = 5,86	1,86
	c = 13,00 Δc = 6,65	
	a/c = 0,86 a/t = 0,30	
	Model 7	
	Off-axis straight in	
P = 88,97 N	a = 15,60 Δa = 10,0	1,58
p_{max} = 0,111 MPa	c = 26,45 Δc = 17,57	
p_{sf} = 0,041 MPa	a/c = 0,59 a/t = 0,42	
	Off-axis straight in	
	a = 13,90 Δa = 4,05	1,87
	c = 18,65 Δc = 10,17	
	a/c = 0,74 a/t = 0,37	
	Model 8	
	Off-axis straight in	
P = 88,97 N	a = 7,90 Δa = 2,8	1,93
p_{max} = 0,103 MPa	c = 13,35 Δc = 7,75	
p_{sf} = 0,049 MPa	a/c = 0,59 a/t = 0,21	
	Model 9	
	Off-axis straight in	
P = 88,97 N	a = 25,10 Δa = 18,7	1,50
p_{max} = 0,110 MPa	c = 39,4 Δc = 33,8	
p_{sf} = 0,049 MPa	a/c = 0,64 a/t = 0,68	

[a] P = axial compressive load; p_{max} = maximum internal pressure to grow crack; p_{sf} = stress freezing pressure.

Marşavina L., Constantinescu D.M., Experimental and numerical crack growth in a special geometry, 21st International Congress of Theoretical and Applied Mechanics, Section SM9L_10864 Fracture and crack mechanics (CD), August 15-21, 2004, Warsaw, Poland

Table 1. Symmetric Crack.

SIF	Initial crack length $a_0 = 8$ mm	Crack extension $\Delta a = 1.8$ mm	Final crack length $a = 9.8$ mm
K_I [MPa $\sqrt{mm}$]	11.18	propagation in 5 steps of 0.36 mm	11.71
K_{II} [MPa $\sqrt{mm}$]	0		0.544

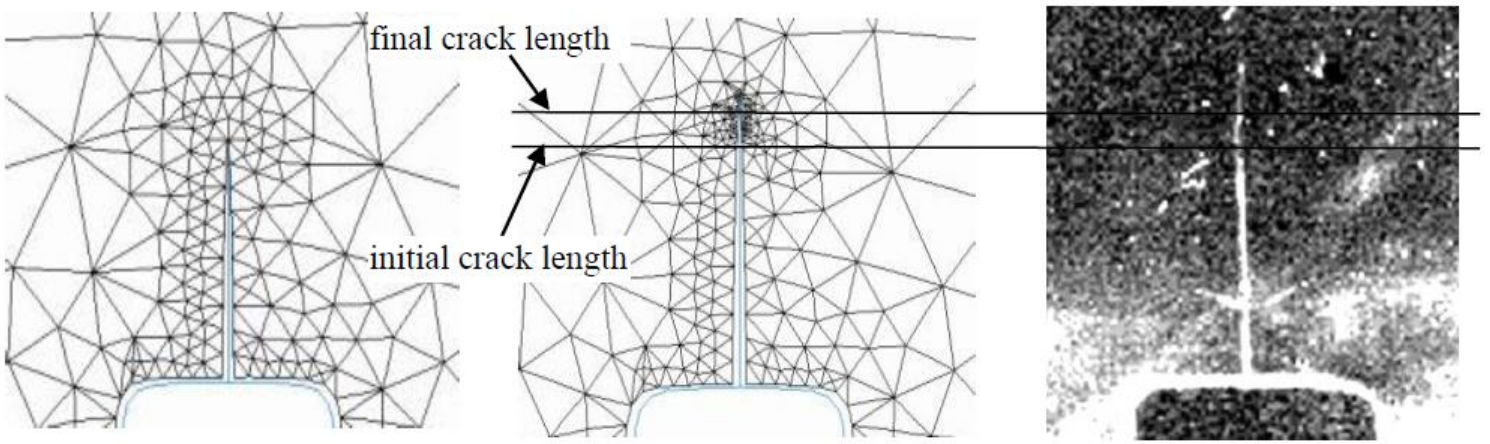

numerical – initial crack | numerical – after propagation | experimental – after propagation

FRANC 2D propagation

Table 2. Off-axis straight-in crack.

SIF	Initial crack length a_0 = 5.6 mm	Crack extension Δa = 10 mm	Final crack length a = 15.60 mm
K_I [MPa $\sqrt{mm}$]	9.457	propagation in 20 steps of 0.5 mm	15.49
K_{II} [MPa $\sqrt{mm}$]	1.020		0.734

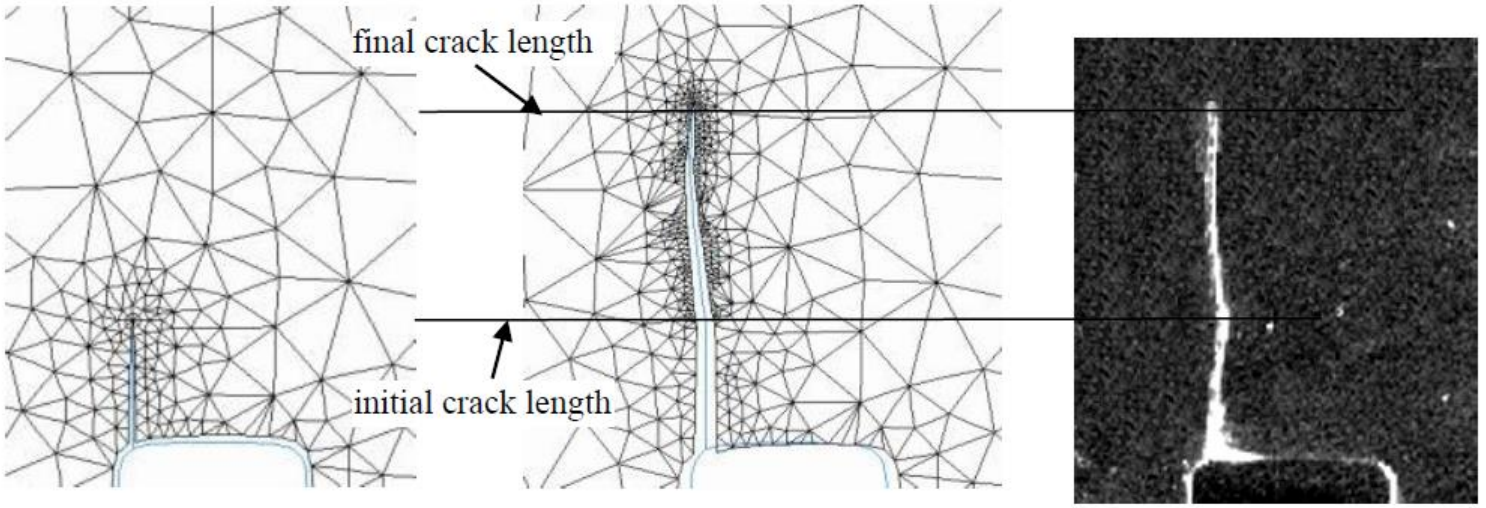

numerical – initial crack | numerical – after propagation | experimental – after propagation

FRANC 2D propagation

Constantinescu D.M., Bocaneala B., Marsavina L. (2006) Three-Dimensional Experimental and Numerical Sifs and Crack Growth. In: Gdoutos E.E. (eds) Fracture of Nano and Engineering Materials and Structures. Springer, Dordrecht.
https://doi.org/10.1007/1-4020-4972-2_577
Section 25_2 Mixed-Mode Fracture CD, 16th European Conference of Fracture (ECF16), 3-7 July, 2006, Alexandroupolis, Greece

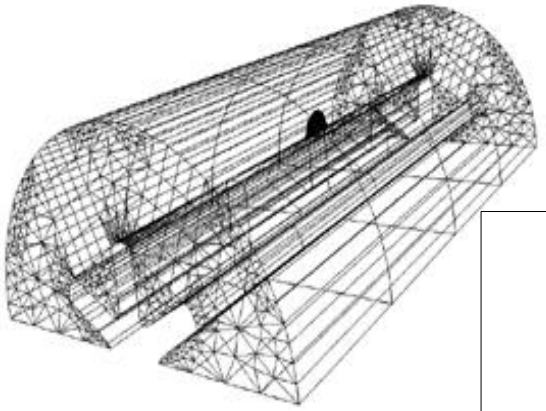

FRANC 3D numerical model

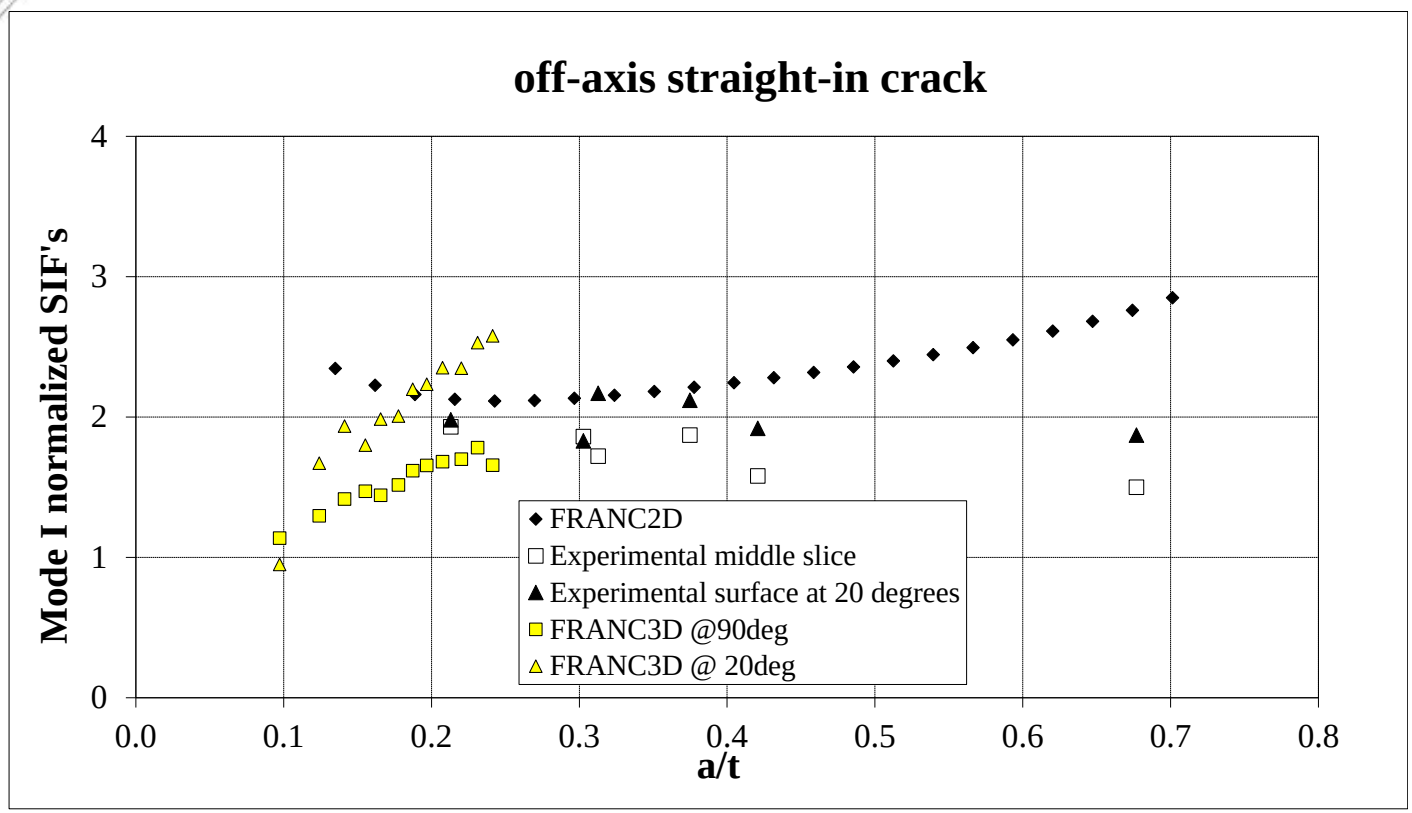

Has photoelasticity a future?

Engineering Fracture Mechanics 236 (2020) 107222

Contents lists available at ScienceDirect

Engineering Fracture Mechanics

journal homepage: www.elsevier.com/locate/engfracmech

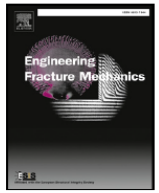

Visualization of full-field stress evolution during 3D penetrated crack propagation through 3D printing and frozen stress techniques

Peng Liu[a], Yang Ju[b,c,*], Guoming Fu[d], Zhangyu Ren[e]

[a] School of Energy and Mining Engineering, China University of Mining & Technology, Beijing 100083, China
[b] State Key Laboratory of Coal Resources & Safe Mining, China University of Mining & Technology, Beijing 100083, China
[c] Frontier Scientific Research Centre for Fluidized Mining of Deep Underground Resources, China University of Mining & Technology, No. 1 University Ave, Xuzhou 221006, China
[d] School of Mechanics and Civil Engineering, China University of Mining & Technology, Beijing 100083, China
[e] School of Aerospace Engineering, Tsinghua University, Haidian District, Beijing 100084, China

Optics and Lasers in Engineering 128 (2020) 106013

Contents lists available at ScienceDirect

Optics and Lasers in Engineering

journal homepage: www.elsevier.com/locate/optlaseng

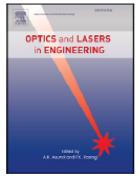

Optical method to quantify the evolution of whole-field stress in fractured coal subjected to uniaxial compressive loads

Yang Ju[a,b,*], Yating Wang[c], Zhangyu Ren[c,d], Lingtao Mao[a,c], Yongliang Wang[c], Fu-pen Chiang[e]

[a] State Key Laboratory of Coal Resources and Safe Mining, China University of Mining and Technology at Beijing, D11 Xueyuan RD, Beijing 100083, China
[b] Frontier Scientific Research Centre for Fluidized Mining of Deep Underground Resources, China University of Mining & Technology, No. 1 University Ave, Xuzhou 221006, China
[c] School of Mechanics and Civil Engineering, China University of Mining & Technology at Beijing, D11 Xueyuan RD, Beijing 100083, China
[d] Department of Engineering Mechanics, Tsinghua University, Beijing 100086, China
[e] Department of Mechanical Engineering, Stony Brook University, NY 11794-2300, USA

Optical methods used in Fracture Mechanics

- The optical techniques for strain measurement mainly include
  - Moiré methods
  - geometric phase analysis (GPA)
  - caustics
  - strain gradient method
  - digital image correlation (DIC)
  - electronic speckle pattern interferometry (ESPI)
  - coherent gradient sensing (dynamic fracture) etc.
- Moiré interferometry (virtual reference grating 4000 lines/mm; sensitivity 0.25 μm/fringe)

  Post D., Han B., Ifju P. (1994) Moiré Interferometry. In: High Sensitivity Moiré. Mechanical Engineering Series. Springer, New York, NY.

  Moiré interferometry is capable of measuring in-plane displacements with very high sensitivity.

Digital Image Correlation (DIC),
Speckle patterns are usually applied by spraying the specimen or component surface with contrasting paints (i.e. black, white and grey). The strain resolution is typically 0.01%. Digital 3D systems are available allowing the dynamic measurement of full-field 3D displacements and subsequent analysis of strains. **Moved to microDIC**.

Behavior and damage of composites

14 – sandwich with two skins **11** and a 12 mm thickness polyurethane core of 40 kg/m^2 is done a material denoted;

9 – sandwich with two 3 mm thickness mat skins; the core is polyurethane of 200 kg/m^3 and a thickness of 12 mm.

The skins and sandwiches have the following configuration:

10 – polyester orange gelcoat and three laminae as 1 x mat 300 gr/m^2, 1 x roving 400 gr/m^2, 1 x mat 300 gr/m^2, all of them being impregnated by ortophtalic polyester resin;

11 – polyester white gelcoat and three laminae as 1 x mat 300 gr/m^2, 1 x roving 500 gr/m^2, 1 x mat 150 gr/m^2, all of them being impregnated by polyester resin Crystic 2-446 PAVL;

12 – polyester green gelcoat 1401 and two laminae as 1 x mat 100 gr/m^2 and 1 x mat 450 gr/m^2, being impregnated by ortophtalic polyester resin;

13 –sandwich with the sequence of **12** and two Coremat cores of 2 mm each, followed by a 1 x mat 450 gr/m^2;

MODE I TESTING OF SANDWICH COMPOSITES

The tested sandwich composites have the skins made from mat having randomly disposed fibers with 50 mm length with one layer of white polyester gelcoat, one layer of mat of 300 g/m^2, one layer of roving of 500 g/m^2 and another layer of mat (from the top to the core). The foam is rigid polyurethane of 200 kg/m^3. The bonding of the foam to the skins was done using a polyurethane tricomponent adhesive and an initial delamination of 70 mm length was produced by including a 70 mm non adherent film on both upper and lower interface zones. The adhesive layer has the thickness 0.2 – 0.25 mm.

Samples prepared for testing

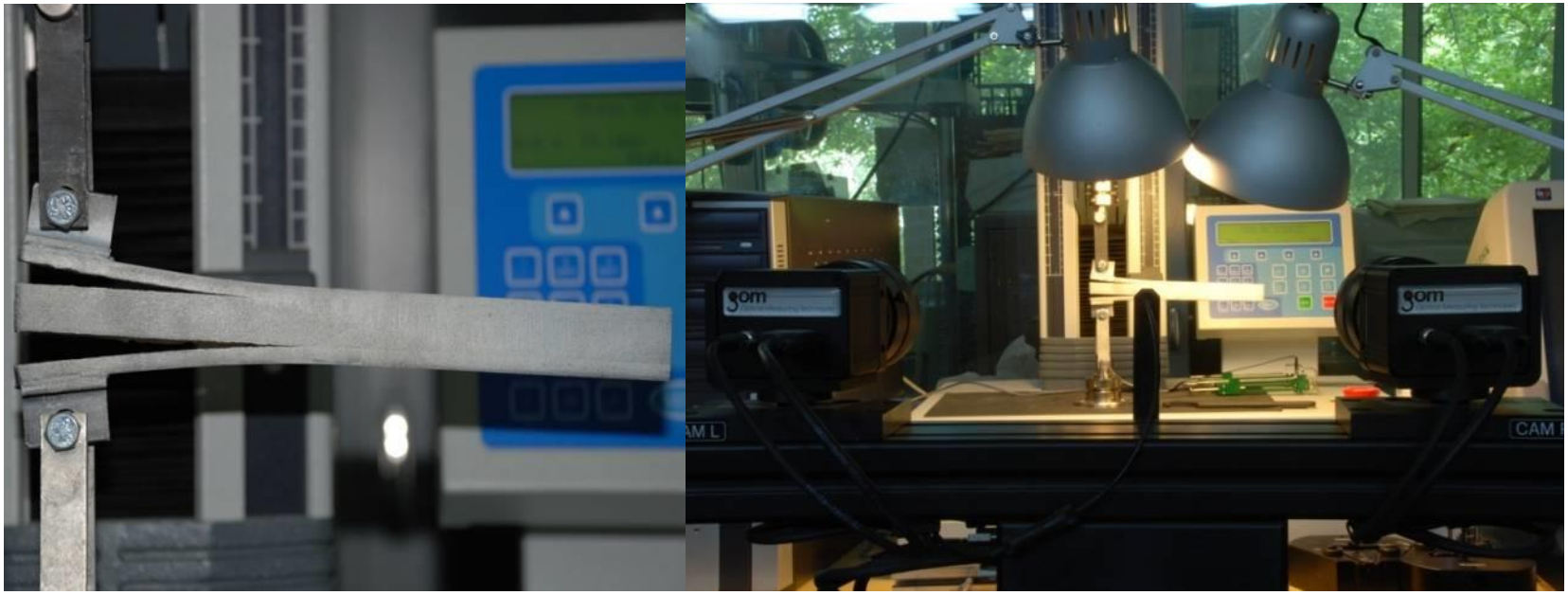

Lloyd testing machine and the ARAMIS system

The sample is loaded in traction with controlled displacement of the crosshead of 0.5 mm/min. During the test the following parameters are recorded:

- Initial delamination lengths (upper and lower). Initial delamination lengths are measured using DIC method and the ARAMIS data acquisition and post processing software.
- Force and displacement values are recorded during the whole test using the Nexygen data acquisition and post processing software provided by LLOYD.
- Position of the crack tip is monitored throughout the whole test using DIC method and ARAMIS data acquisition and post processing software.
- Local strains at the crack tip and CTOD are evaluated using DIC by defining a local measurement point at the crack tip.

Miron, M.C., Constantinescu, D.M., Strain fields at an interface in a sadwich composite, Mechanics of Materials, 43, pp. 870-884, 2011.

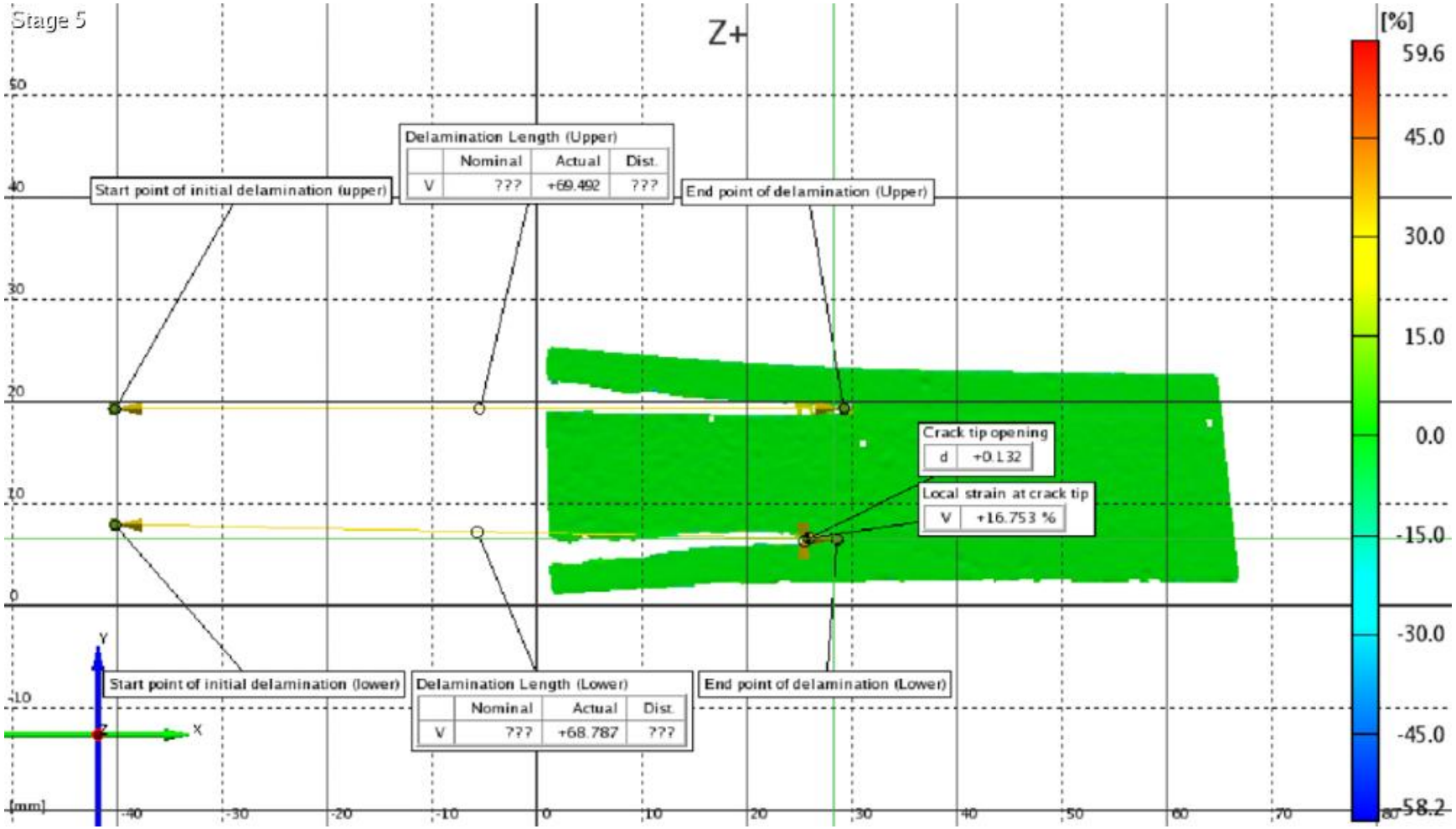

Average maximum strain and the average crack tip opening displacement (CTOD) at the moment of sudden crack propagation

Pictures of the specimen from Test 1 and DIC analyses before and after the second crack propagation.

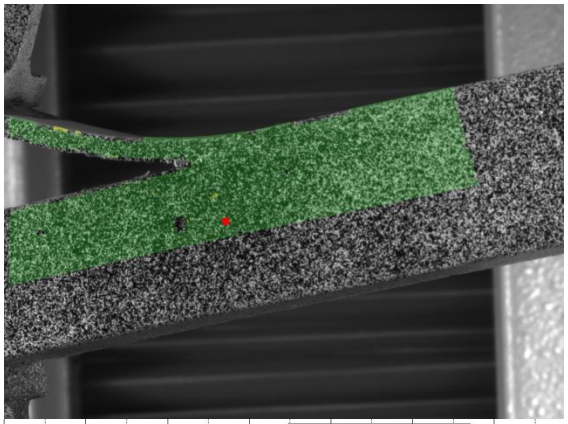

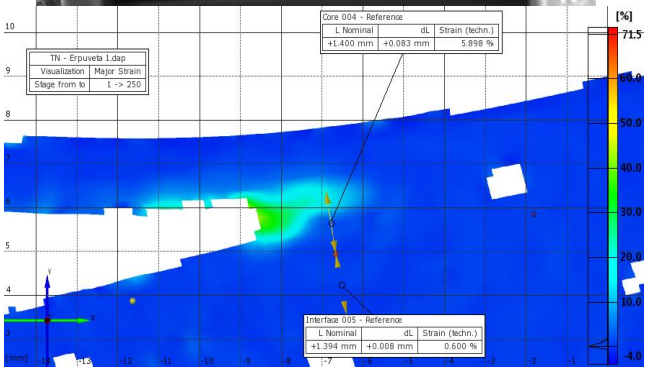

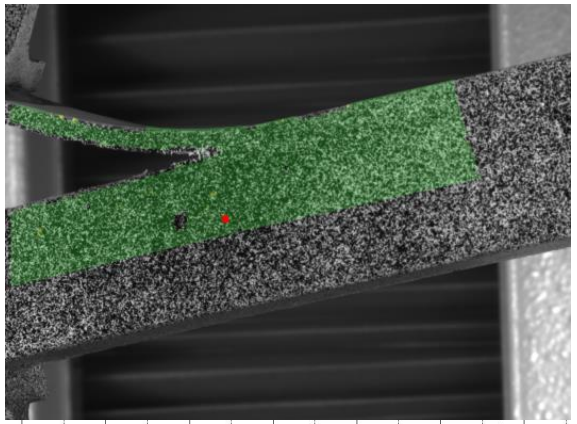

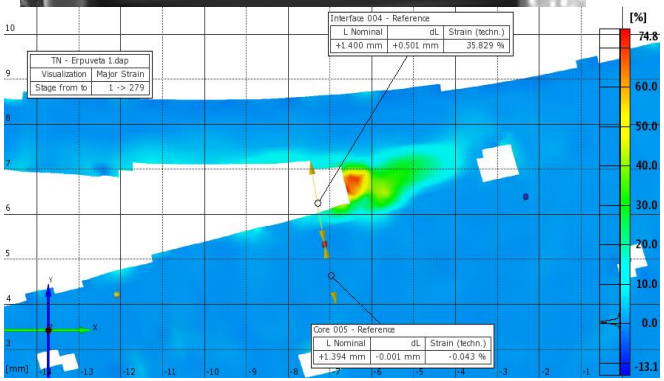

Strain variation at the crack tip before and after unstable crack propagation

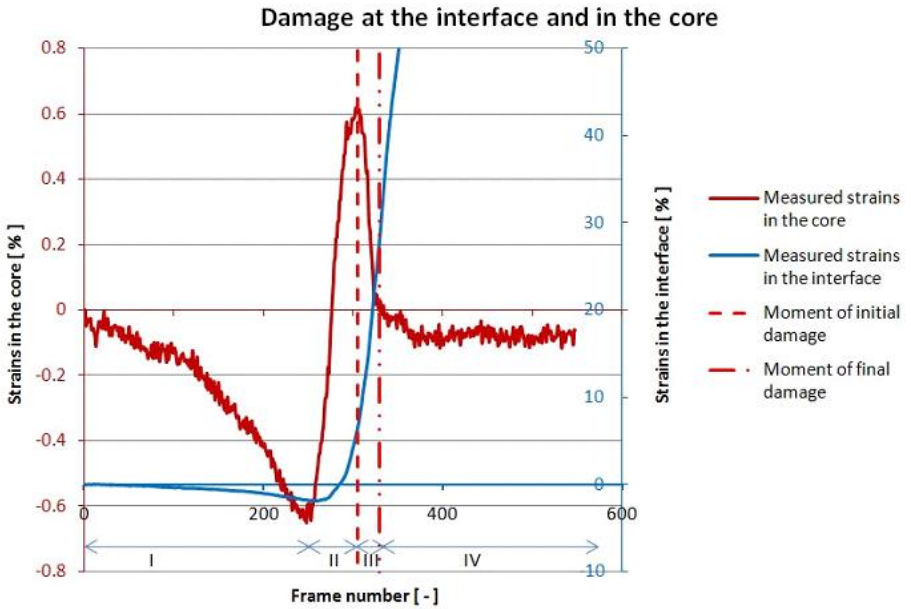

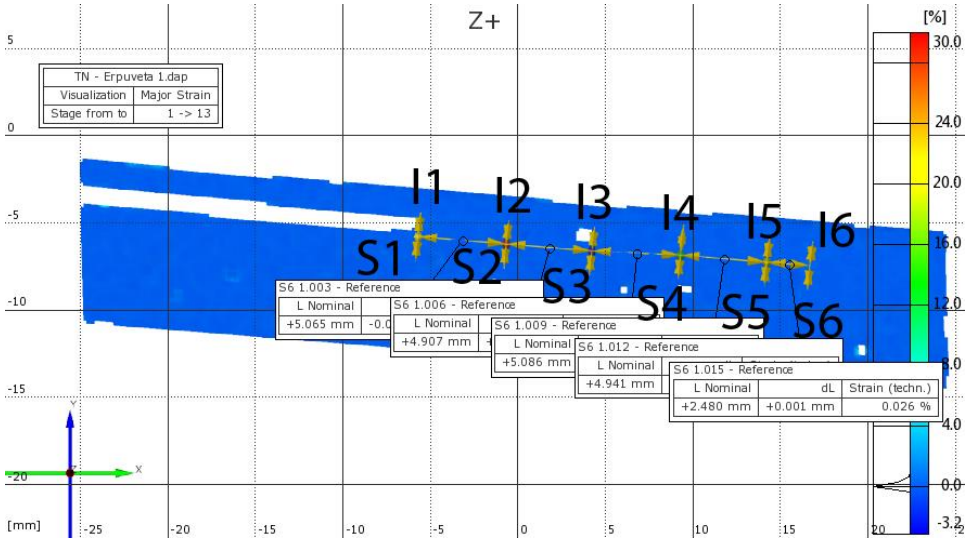

Miron, M.C., Study of the delamination and damage phenomena in laminated and sandwich composites, PhD Thesis, University POLITEHNICA of Bucharest (in Romanian), 2011.

Placement of virtual strain gages along the interface

Experimentally measures strain variation in the core strain gages

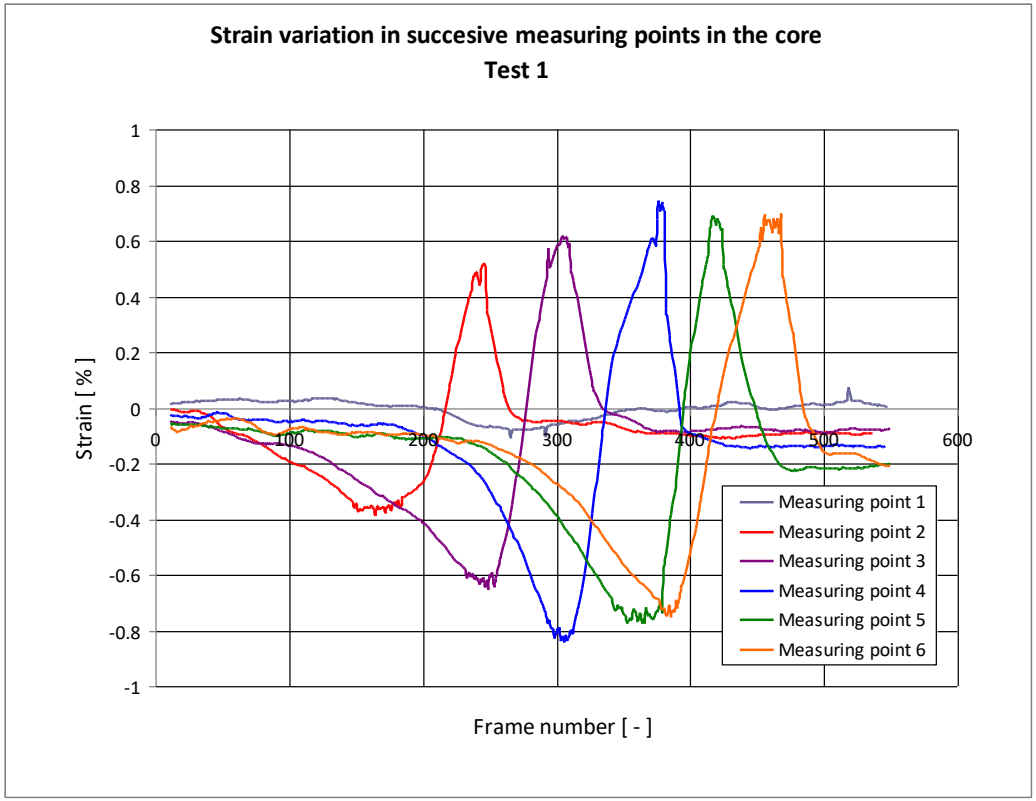

Behavior and damage of nanocomposites

Three types of Bayer **multi-wall carbon nanotubes (MWNT)**: Baytubes C 150 P, Baytubes C 150 HP, Baytubes C70 P (long nanotubes 0,2-1 μm).
Nanopowders from Sigma-Aldricht


Shear mixer Thinky model ARE -250, Japan


Sonicator SONICS model VCX 750, USA

Programmable oven with vacuum, MEMMERT VO400, UK, with electronic module to program up to 40 types of curing cycles through a laptop.

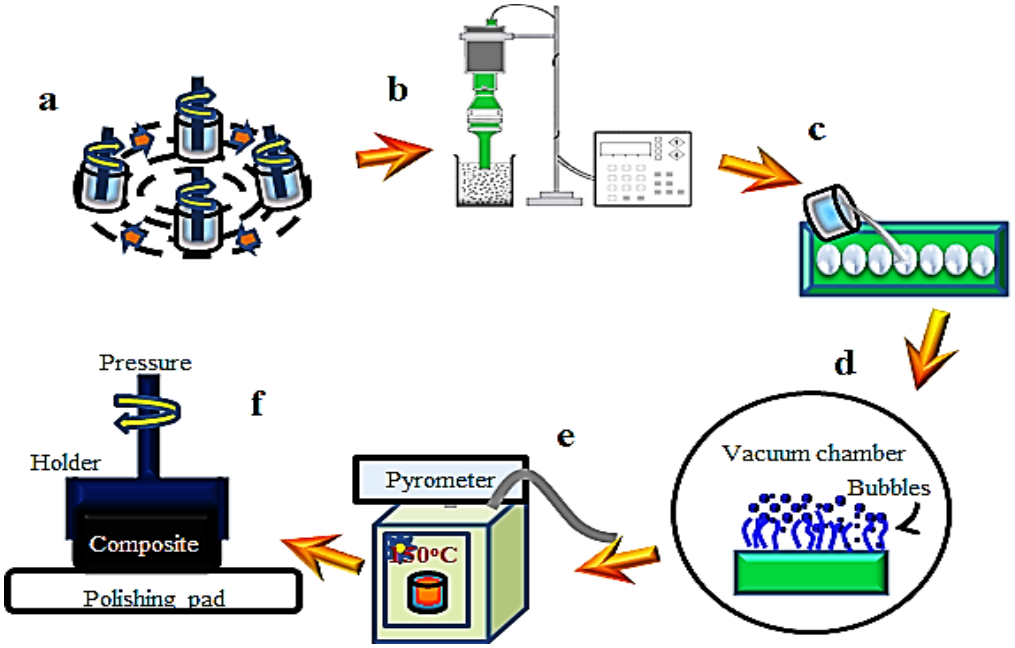

Technology used to fabricate nanocomposites used at Rensselaer Polytechnic Institute (US) transferred to UPB.

Tensile specimens poured in a silicon mold produced at UPB.

Nanopowder	Observations
Iron (II,III) oxide Fe_3o_4 (Magnetite)	< 50 nm (TEM) purity greater than 98%
Aluminium Oxide Al_2O_3 (Alumina)	< 50 nm
Zinc Oxide OZn	< 100 nm
Silicon Dioxide O_2Si (Silica)	5-15 nm purity greater than 99.5 %
Tine (IV) Oxide O_2Sn	< 100 nm
Cobalt (II,III) Oxide Co_3O_4	< 50 nm purity 99.5 %

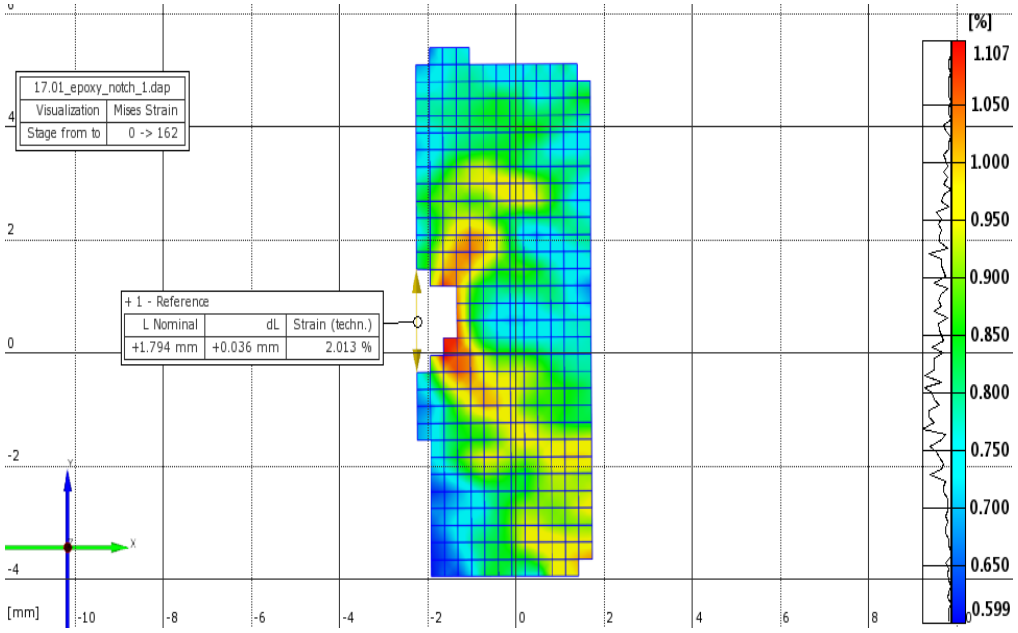

Mises strains in epoxy SEN specimen before failure

Mises strains in epoxy with MWNT SEN specimen before failure

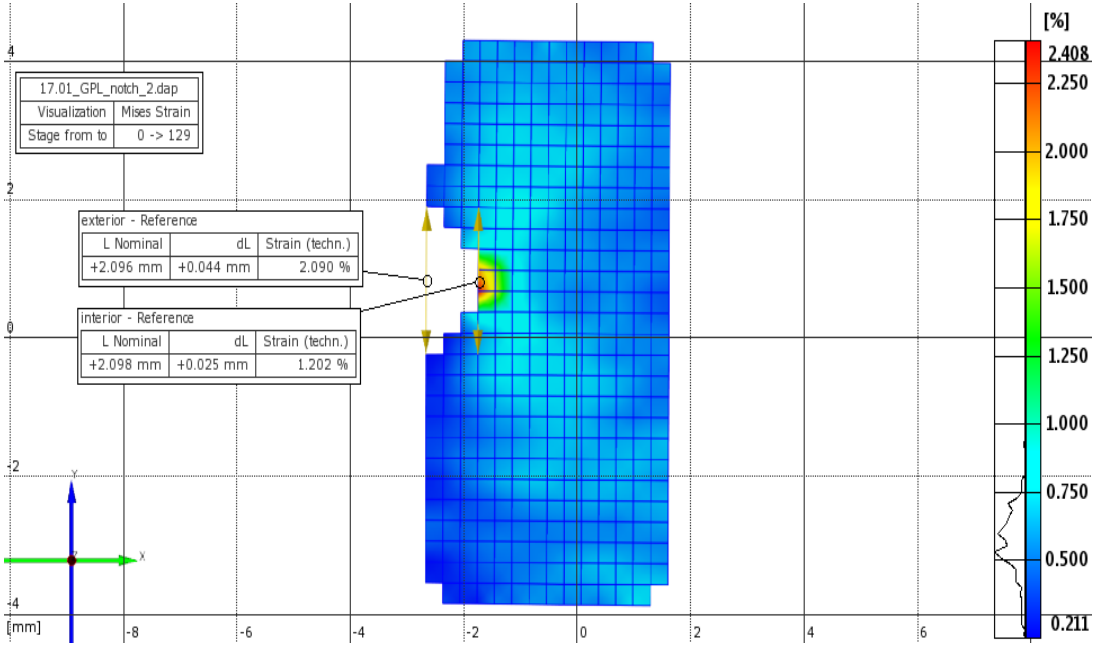

Mechanical properties / Nanofillers	E [MPa]	Ultimate strength [MPa]	Elongation at failure [%]
Pure epoxy	3470	71,37	2,39
	3115	77,07	4,19
CNT 0,1 %	3298	80,38	4,10
CNT 0,2%	3230	78,82	3,95
CNT 0,3%	3603	81,07	3,93
	3445	81,65	4,09
0,1 % Al_2O_3	3263	81,83	3,9
	3331	85,60	4,11
	3345	85,13	3,96
0,3 % Al_2O_3	3632	57,27	1,9
	3294	80,98	4,23
0,5 % Al_2O_3	3394	84,06	4,09
	3648	85,03	4,11
5 % Al_2O_3	3922	85,51	3,91
0,3 % Fe_3O_4	3310	51,58	1,78
0,3 % ZnO	3547	81,59	4,02
0,3 % CO_3O_4	3420	82,26	3,91
0,3 % SnO_2	3459	81,59	3,91
0,3 % SiO_2	3526	83,02	3,92
1 % SiO_2	3632	85,74	3,65
3 % SiO_2	3437	85,02	3,82

Mechanical properties / Nanofillers	E [MPa]	Ultimate strength [MPa]	Elongation at failure [%]	K_{IC} [MPa$\sqrt{m}$]
Pure epoxy	4685	82,98	3,95	3,08
0,1 % Al_2O_3	4370	83,71	4,30	3,76
0,3 % Al_2O_3	4425	81,47	4,35	4,19
0,5 % Al_2O_3	4235	88,58	3,80	4,03
	4505	80,45	4,55	3,48
0,1 % SiO_2	3215	77,38	4,35	2,82
0,3 % SiO_2	4525	83,81	3,40	3,50
0,5 % SiO_2	4290	84,13	4,15	2,98
	4355	83,20	4,35	3,80

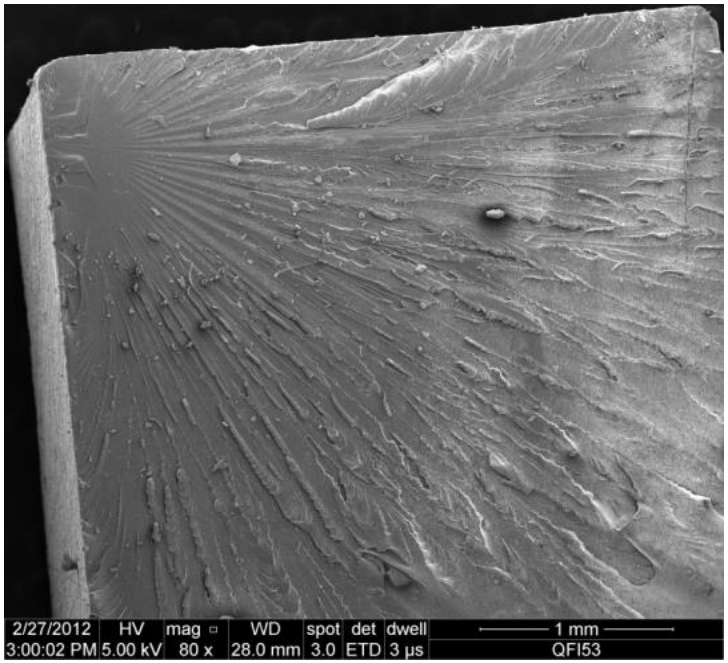

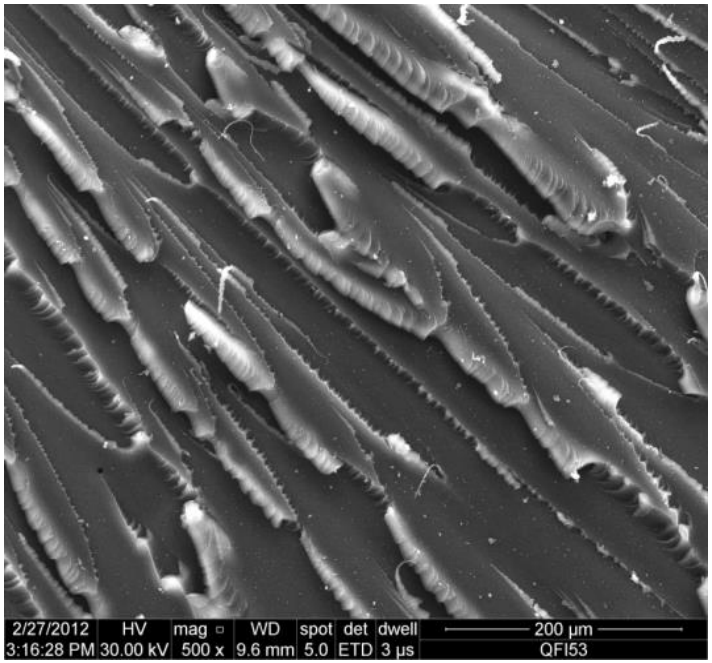

Failure surface for pure epoxy specimen

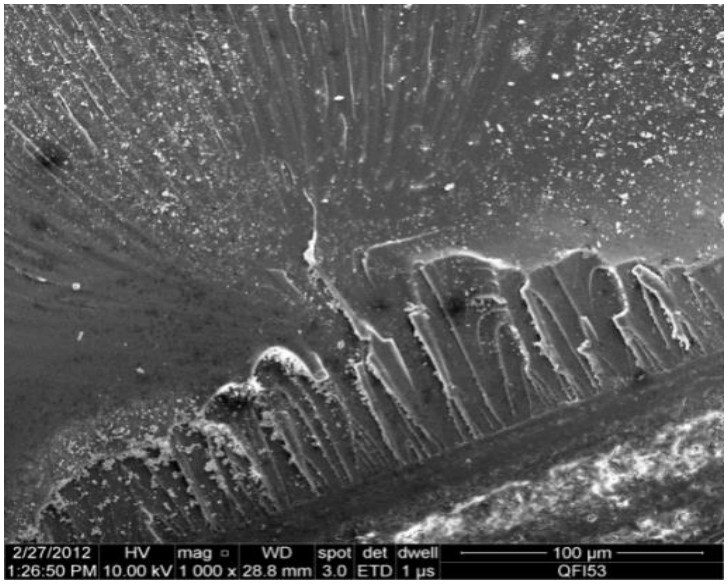

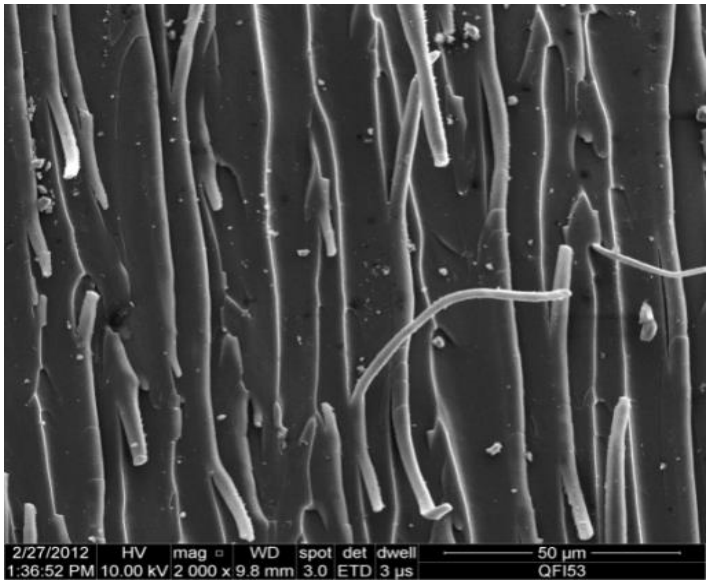

Failure surface for MWNT SEN specimen

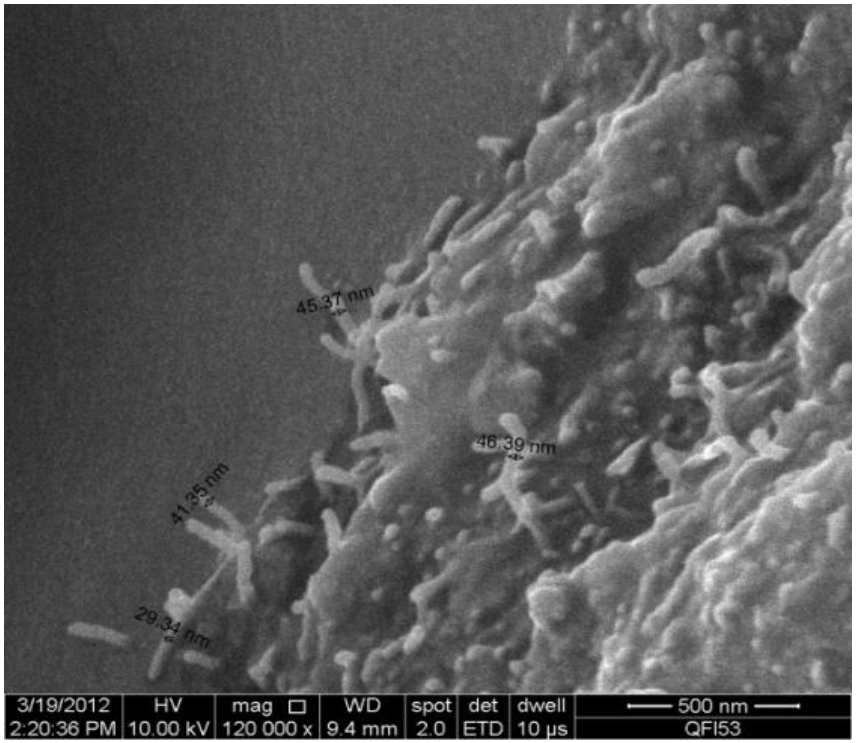

Carbon MWNT with measured diameter between 30-45 nm

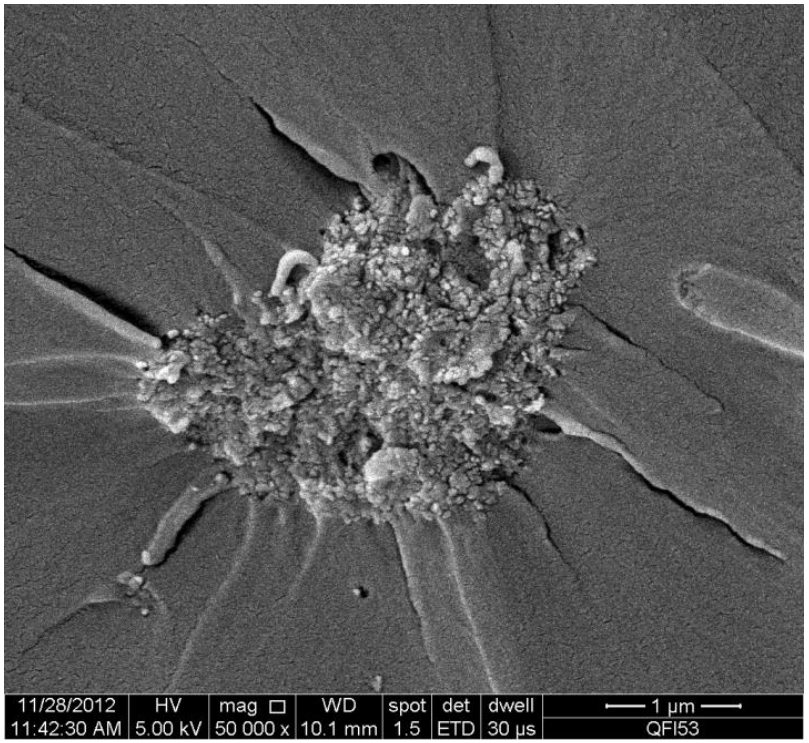

Conglomeration of Al_2O_3 nanoparticles for 0,3 %wt

Cavities induces by air bubbles on the surface

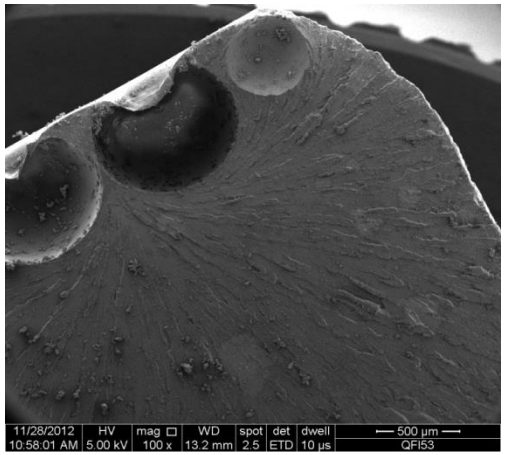

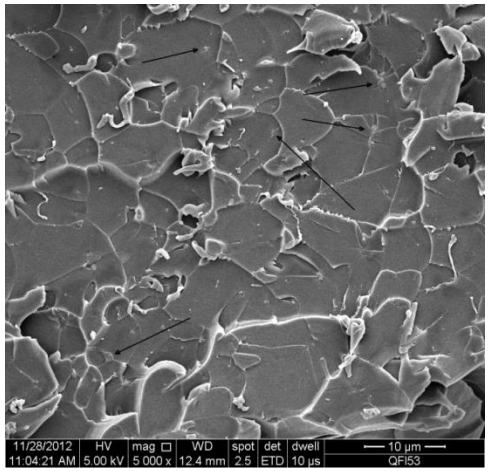

Dispersion of alumina in the bulk epoxy material for 0,5 %wt

Shear behavior of sandwich geometries

ASTM D3528-96 (2008): Standard test method for strength properties of double lap shear adhesive joints by tension loading

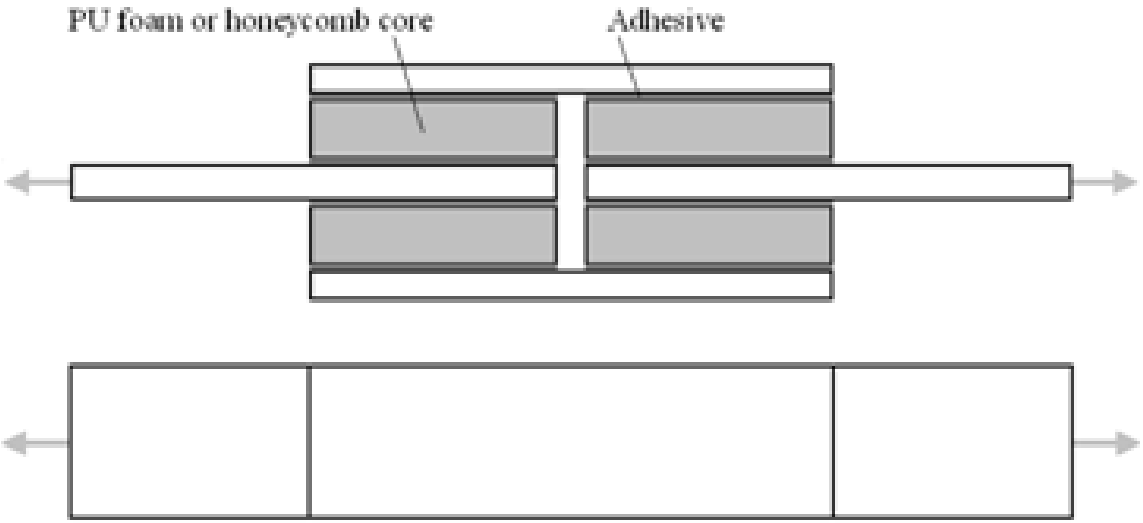

EN 14509 (2006): Self-supporting double skin metal faced insulating panels – Factory made products - Specifications

ASTM C273-00 (2000): Standard test method for shear properties of sandwich core materials

ASTM C393-00 (2000): Standard test method for flexural properties of sandwich constructions

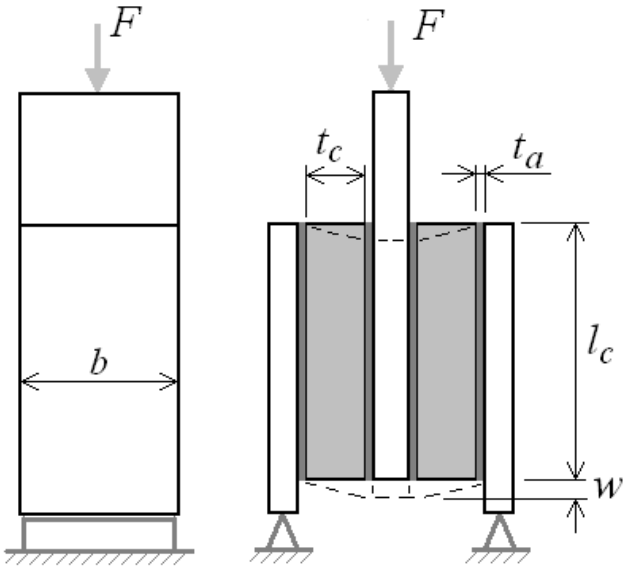

shear modulus of the foam

$$G_c = \frac{F\,t_c}{2\,w\,b\,l_c}$$

ASTM D3528-96

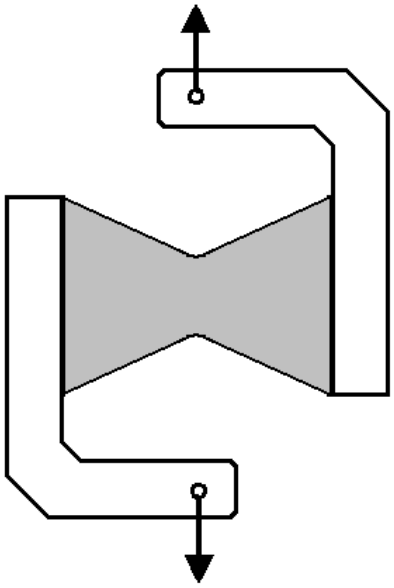

“butterfly” specimen of Iosipescu type used in Arcan loading device

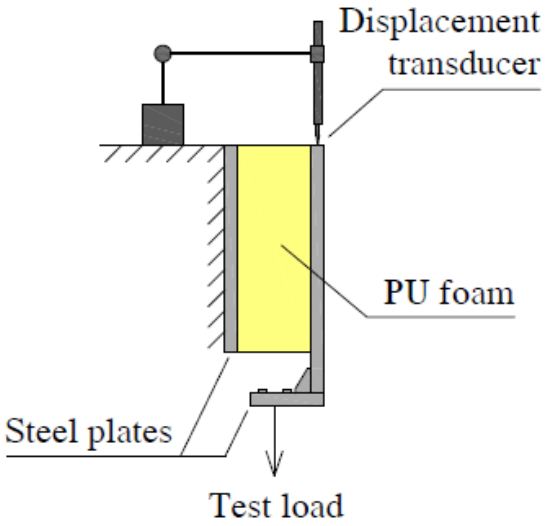

testing arrangement for creep in shear

ANALYZED GEOMETRY

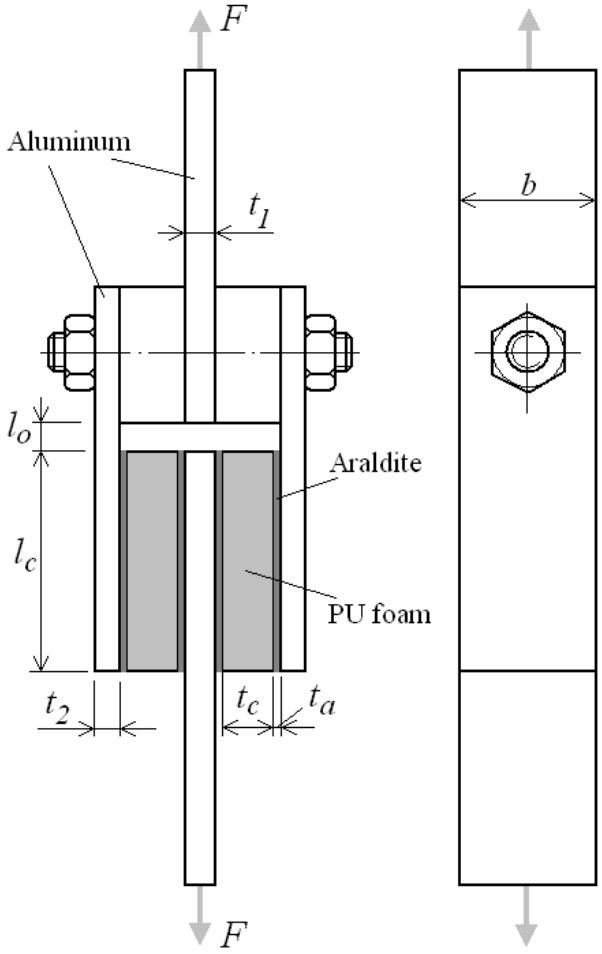

$$\tau_{av} = \frac{F}{2 b l_c}$$

- foam thickness
  t_c = 6 mm, 10 mm, and 15 mm
- overlap length
  l_c = 25 mm and 50 mm
- adherents thickness and width
  $t_1 = t_2$ = 4 mm, b = 25 mm
- adhesive thickness
  t_a = 0.15 mm

	Material	Young's Modulus [MPa]	Poisson's Ratio [-]	Ultimate strength [MPa]
Face sheet	Aluminium alloy	70000	0.33	320
Core	Foam 325 kg/m^3 (NECURON)	220	0.3	4.2
Adhesive	AW 106 (HUNTSMAN)	1350	0.45	33

Experimental evaluation of the failure

Failure initiates in the foam at the critical location, close to the inner adherent

In few cases failure is produced in the foam on both sides of the inner adherent

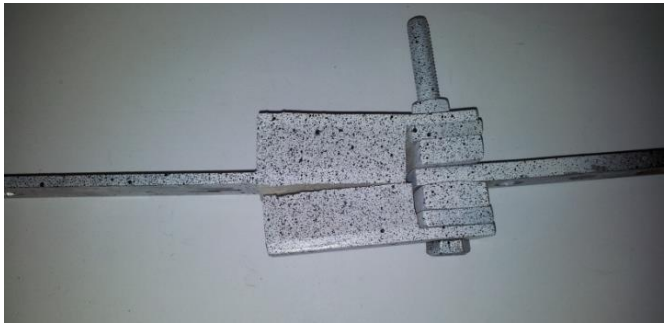

Outer adherent may bend after testing

Cohesive failure in the foam, close to the adhesive layer

The deformation of the double lap joint was obtained using the 3-dimensional digital image correlation (3D-DIC) technique.
The full-field surface displacement and strain distributions obtained provided detailed information about the deformation of the overlap.
The ARAMIS system was calibrated using a 35 x 28 mm caliber and a facet of 27 x 15 pixels; thus a 44 % facet overlap has been obtained.

F.A. Stuparu, Delamination phenomena assessment for adhesive bonded joints, PhD thesis, University POLITEHNICA of Bucharest (in Romanian), 2015.

overlap 25 mm – foam thickness 6 mm

Major strain

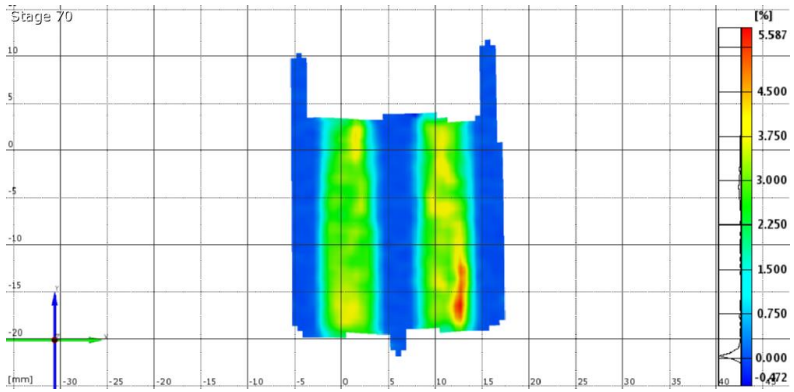

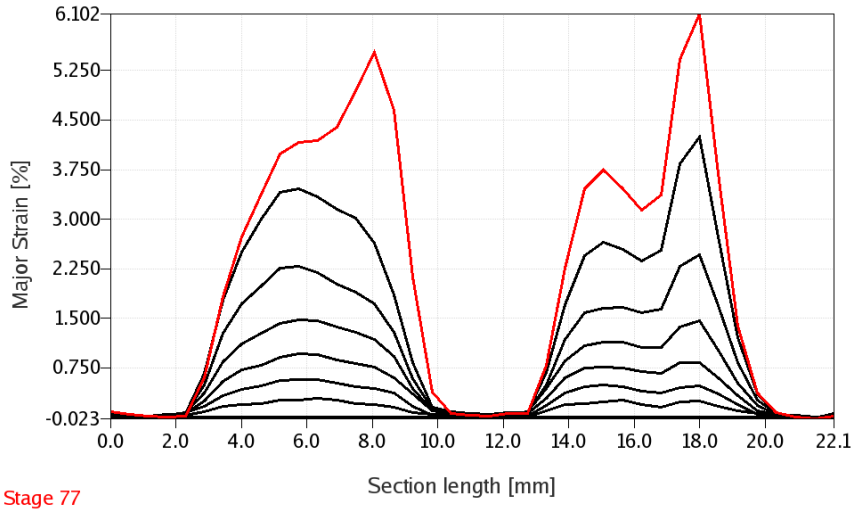

Stage 77

ARAMIS 5/21/13 www.gom.com

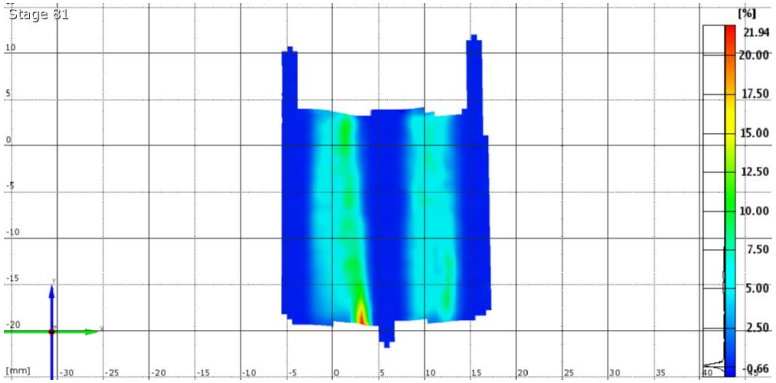

Shear angle

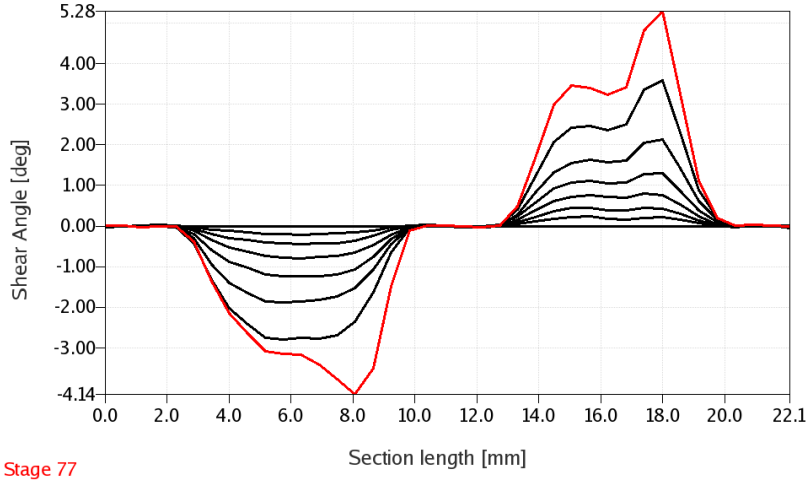

Stage 77

ARAMIS 5/21/13 www.gom.com

overlap 25 mm – foam thickness 15 mm

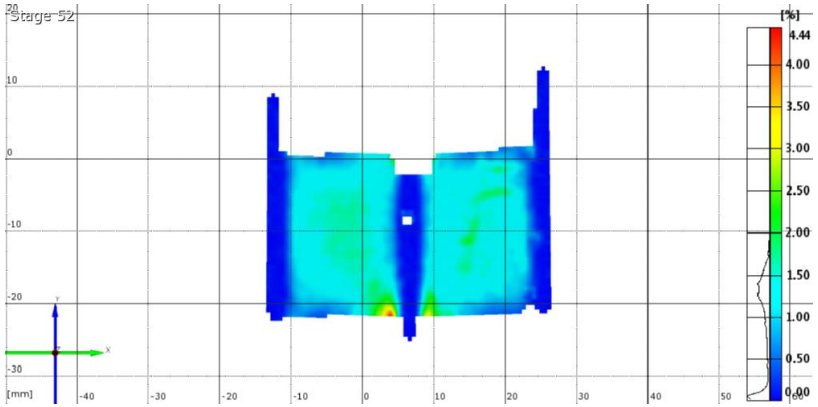

Mises strain

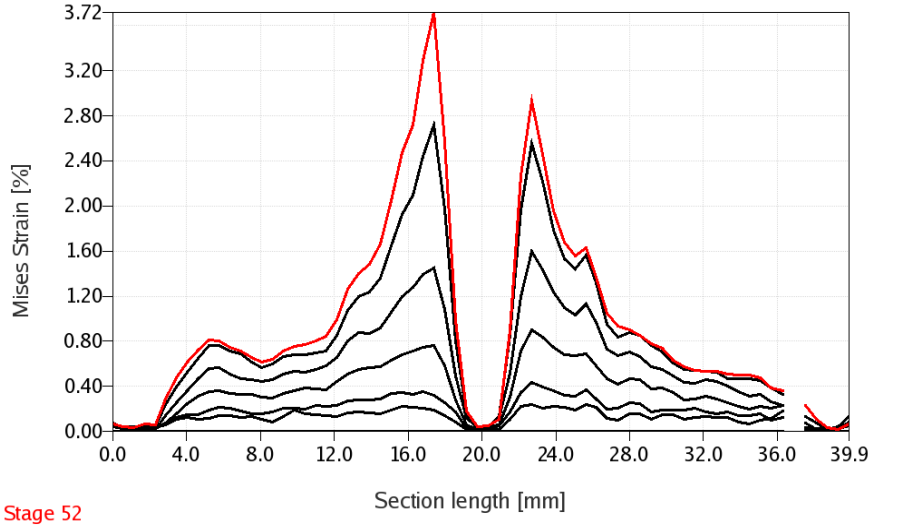

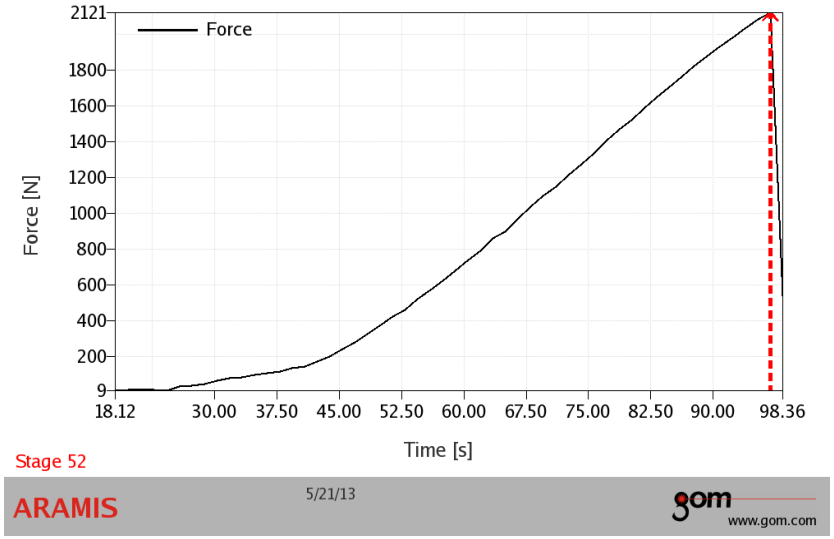

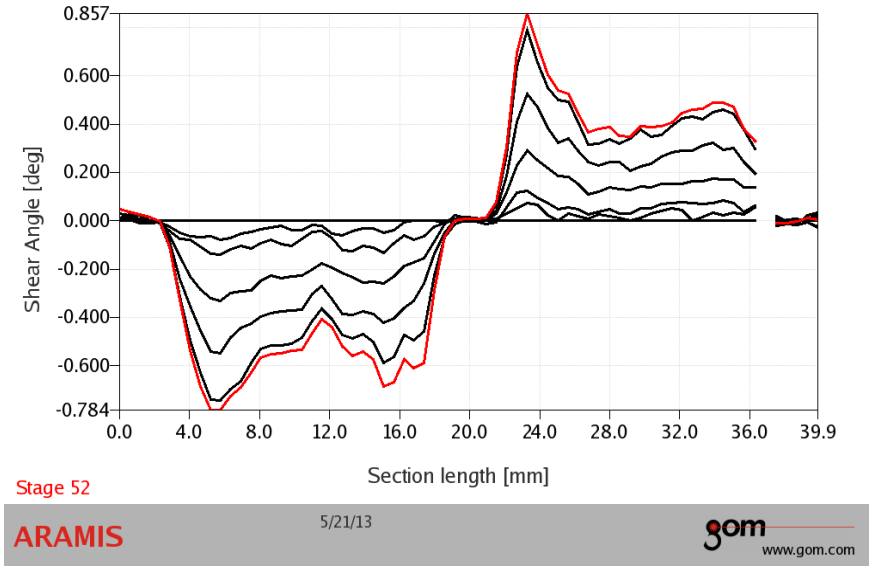

overlap 50 mm – foam thickness 6 mm

Mises strain

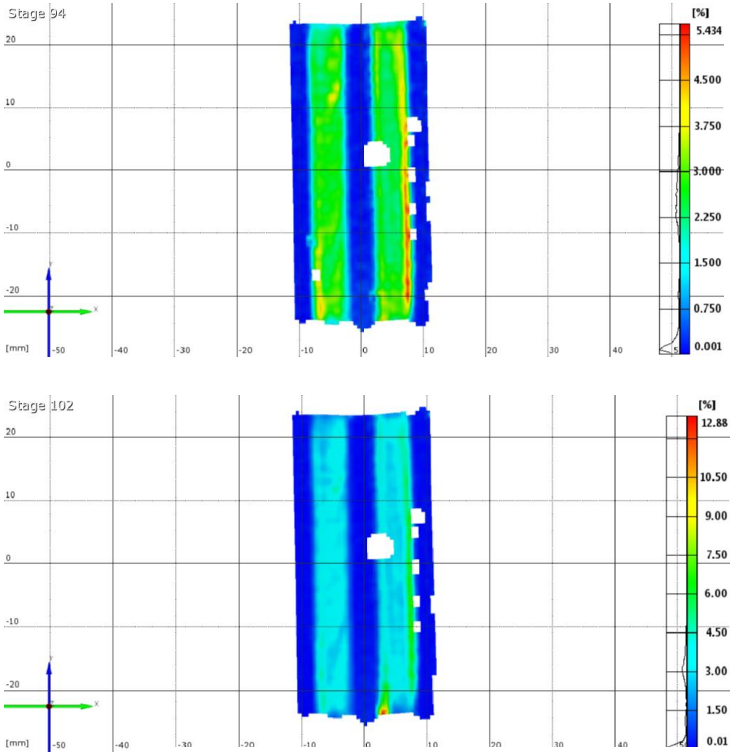

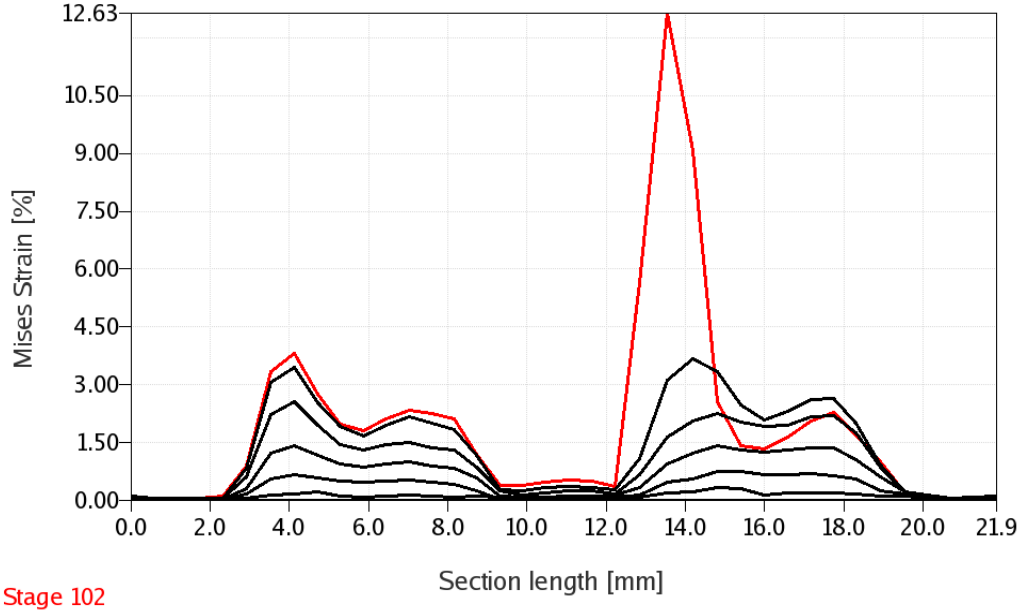

Stage 102

ARAMIS 5/16/13 www.gom.com

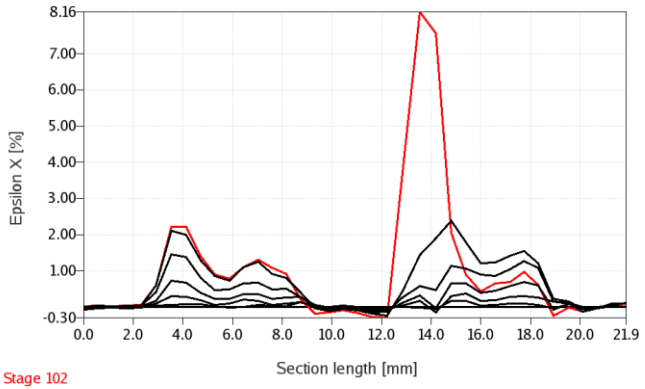

Stage 102

ARAMIS 5/16/13 www.gom.com

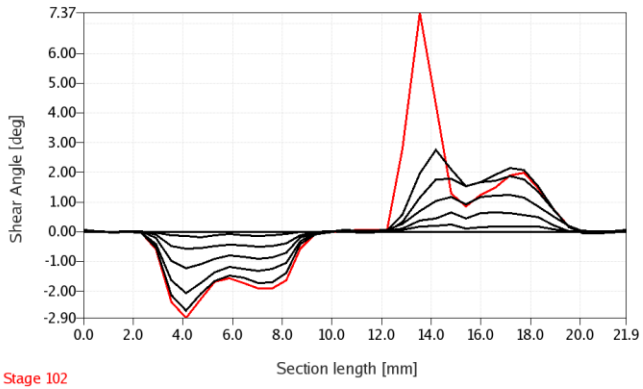

Stage 102

ARAMIS 5/16/13 www.gom.com

overlap 50 mm – foam thickness 15 mm

peeling strain

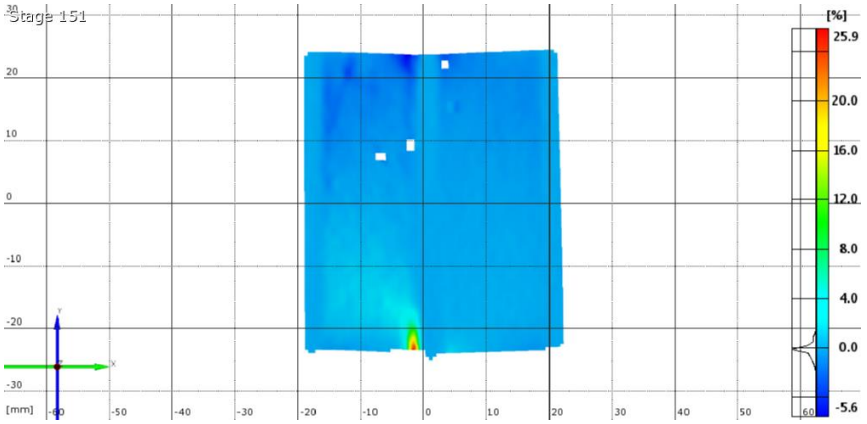

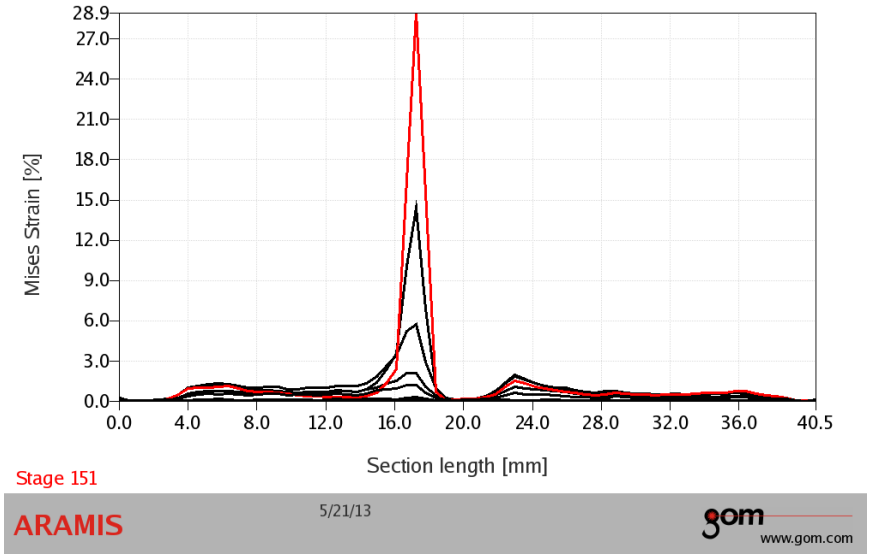

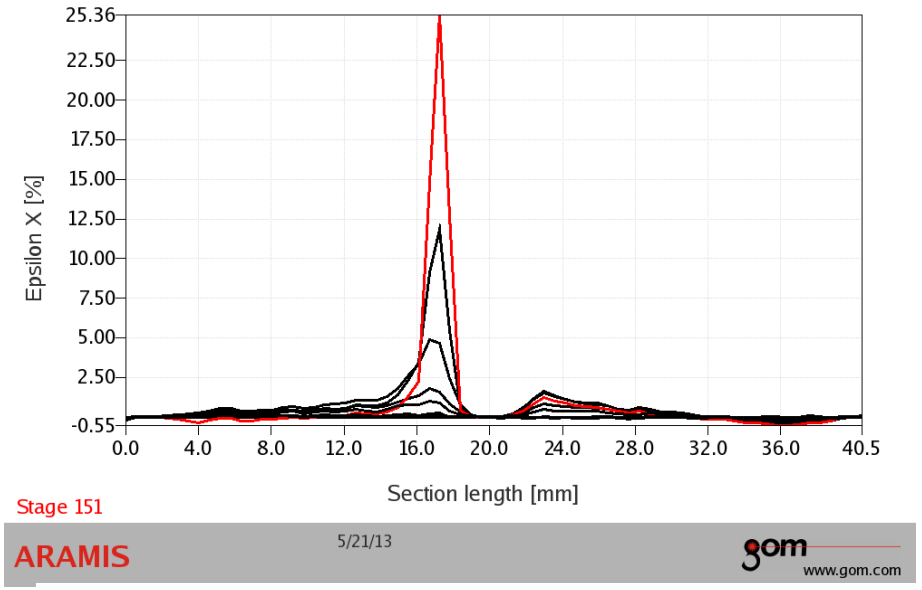

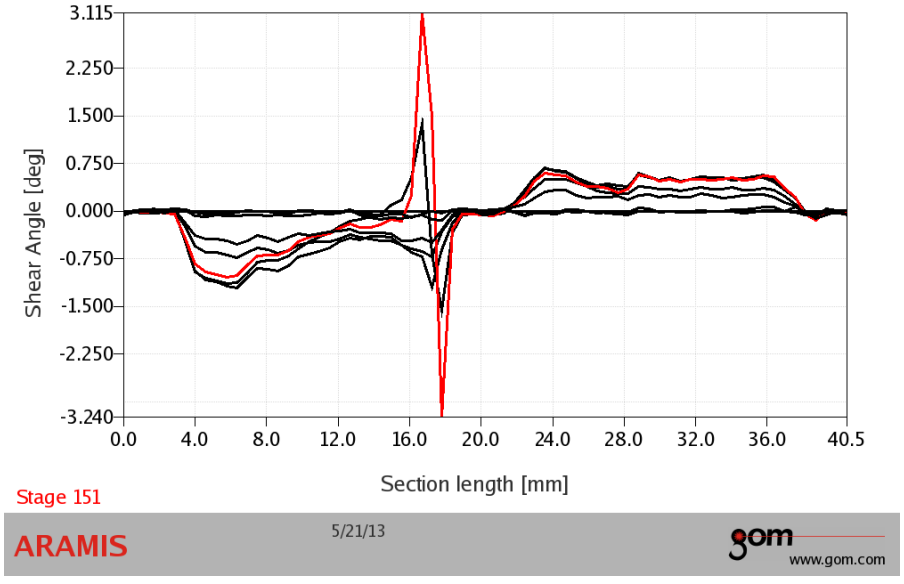

Different foams have been selected for this study, having the densities of 35, 93, 100, 140 and 325 kg/m³

The tested foams are used for the construction of sandwich panels used for different boat models

D.A. Apostol, Investigations concerning the behaviour and damage of composites made with rigid and semirigid foams, PhD thesis, University POLITEHNICA of Bucharest (in Romanian), 2011.

Use of DIC for damage assessment

The deformation of foam specimens in compression was obtained using the 3-dimensional digital image correlation (3D-DIC) technique.
The full-field surface displacement and strain distributions obtained with this technique provided detailed information about the nonhomogeneous deformation over the area of interest during compression.
The ARAMIS system was calibrated using a 35 x 28 mm caliber and a facet of 27 x 15 pixels; thus a 44 % facet overlap has been obtained.

100 kg/m^3

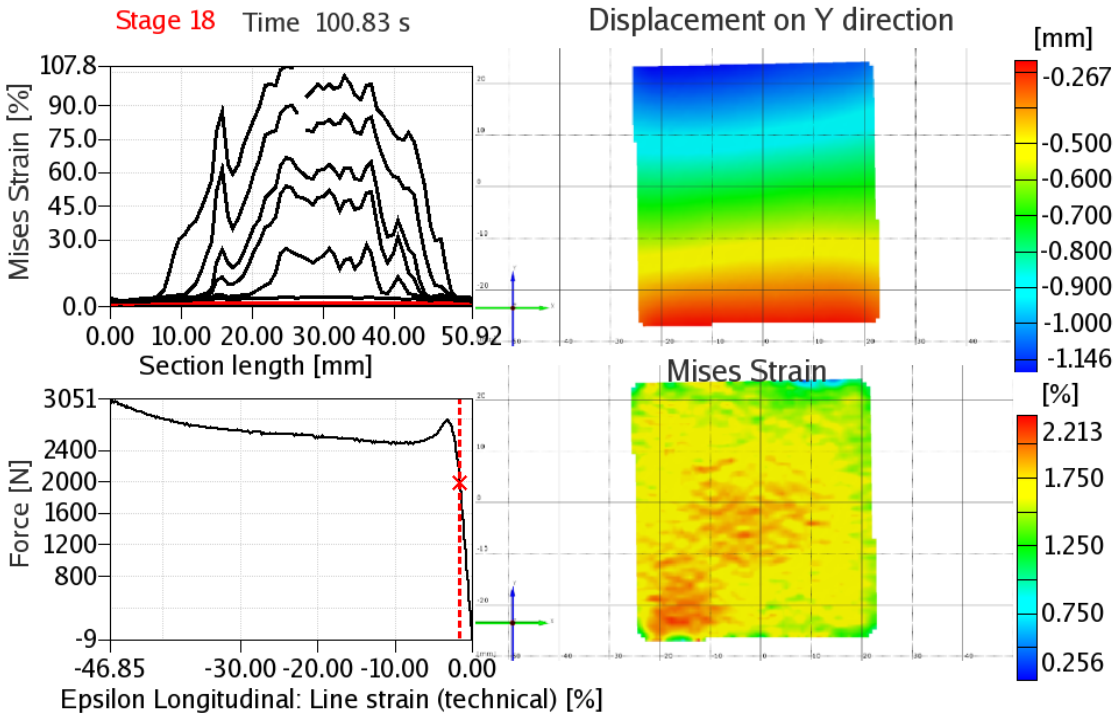

For the foam of 100 kg/m^3 and a speed of 1 mm/min are presented the reports obtained in the linear elastic region. Global and local strains are about the same at the same moment of the test, as after about 1120 seconds.

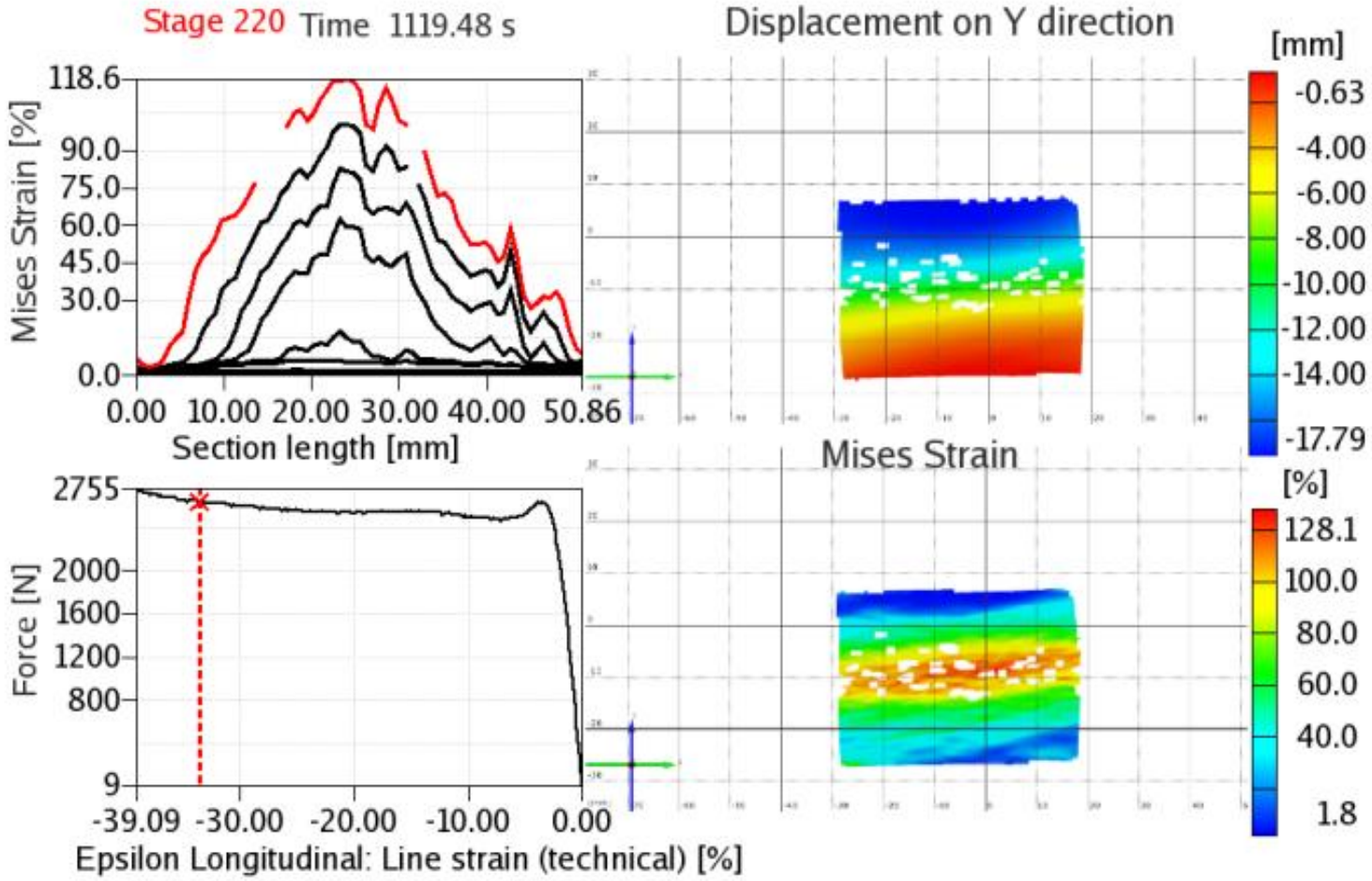

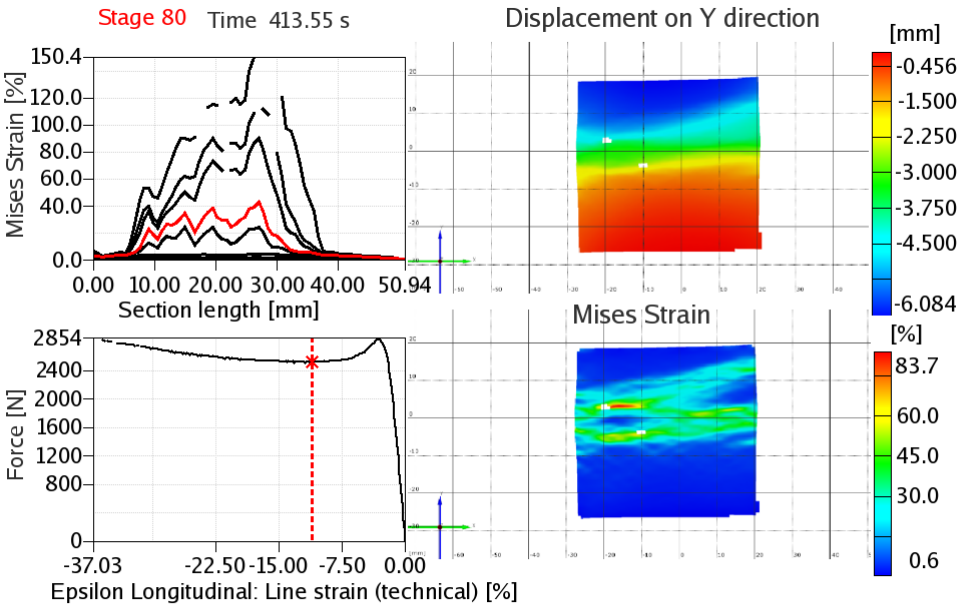

Two stages for different tests in the plateau region for the foam of 100 kg/m^3

Localized deformation bands appear in the middle section of the specimen

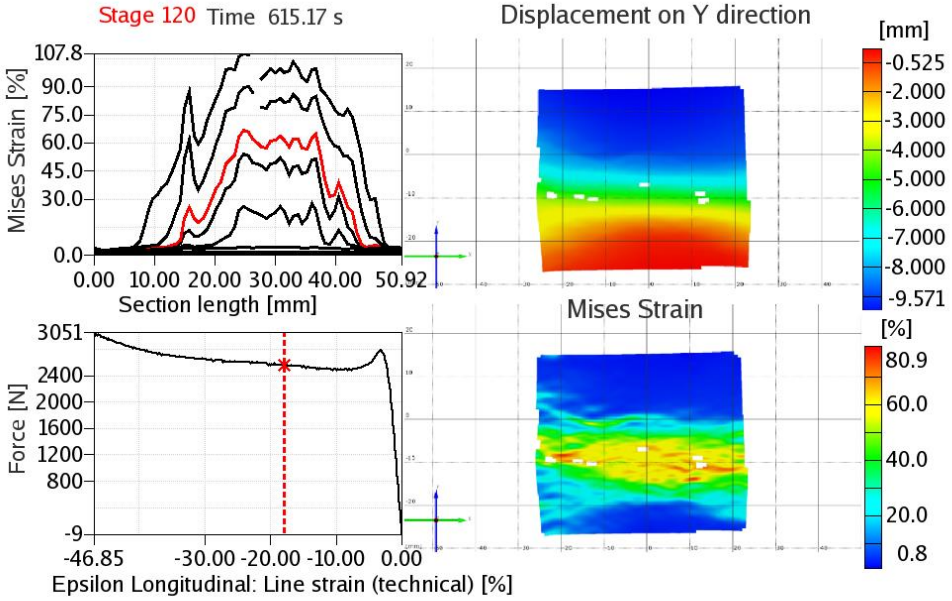

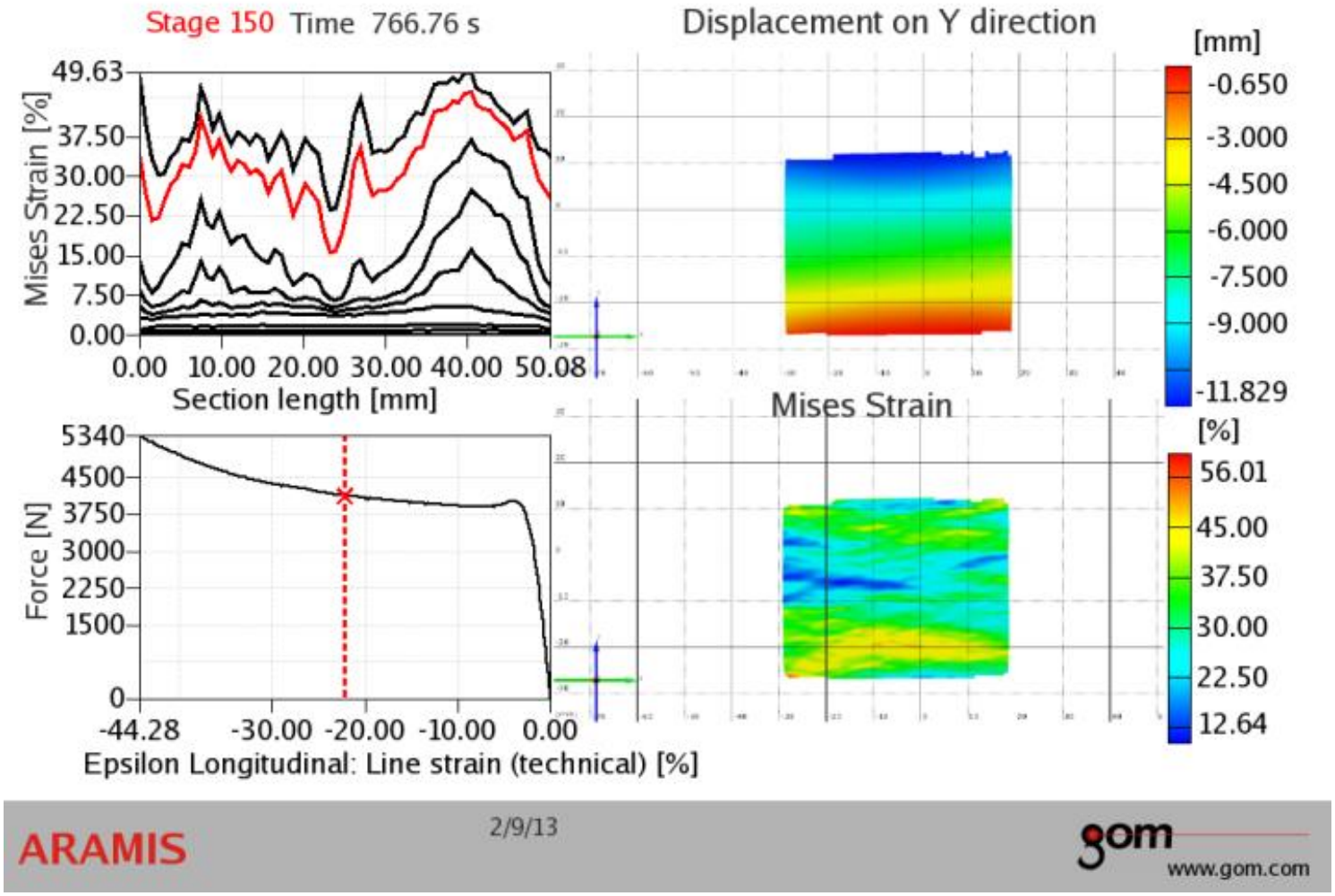

140 kg/m^3

Apostol D.A., Constantinescu D.M., Marsavina, L., Linul, E., Analysis of deformation bands in polyurethane foams, Key Engineering Materials, 601, 250-253, 2014.

Apostol D.A., Constantinescu D.M., Stuparu F.A., Characterization and Damage Assessment of Polyurethane Foams Subjected to Compression Testing, Materiale Plastice, vol. 53, no. 3, 454-457, 2016.

These experimental observations of deformation bands indicate DIC as a powerful full-field tool to monitor the local crushing behaviour, being capable to account for the influence of the foam density and speed of testing.

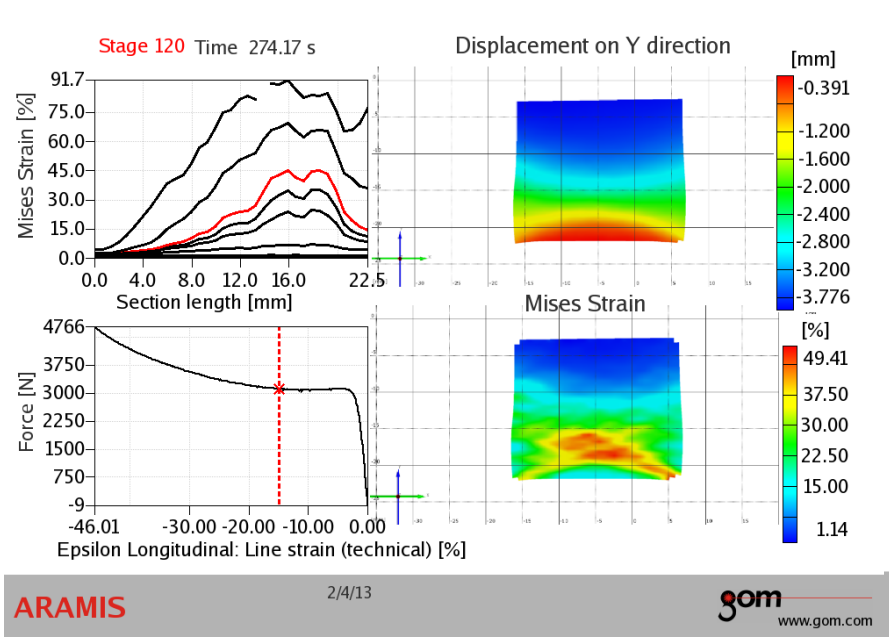

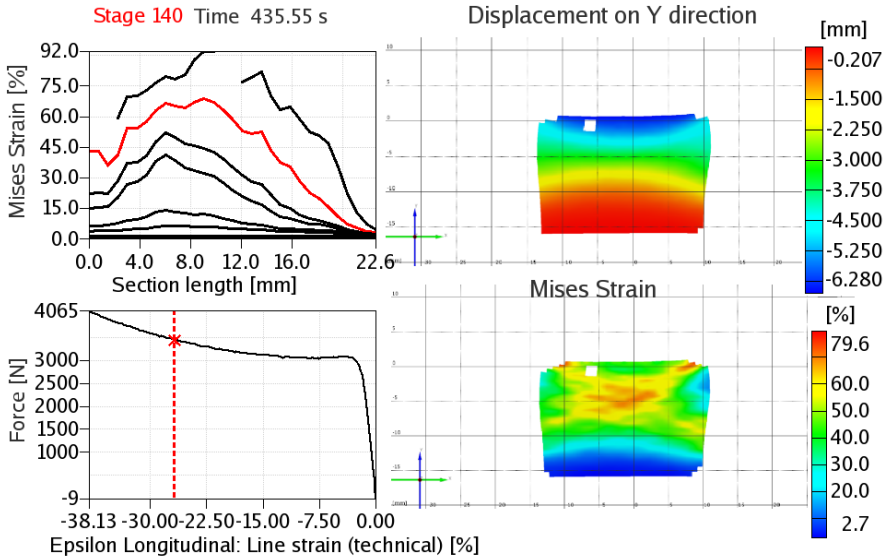

Local deformation for the foam with 325 kg/m^3 tested at 1 mm/min

Influence of the boundaries for the foam with 325 kg/m^3 tested at 1 mm/min

100 kg/m^3

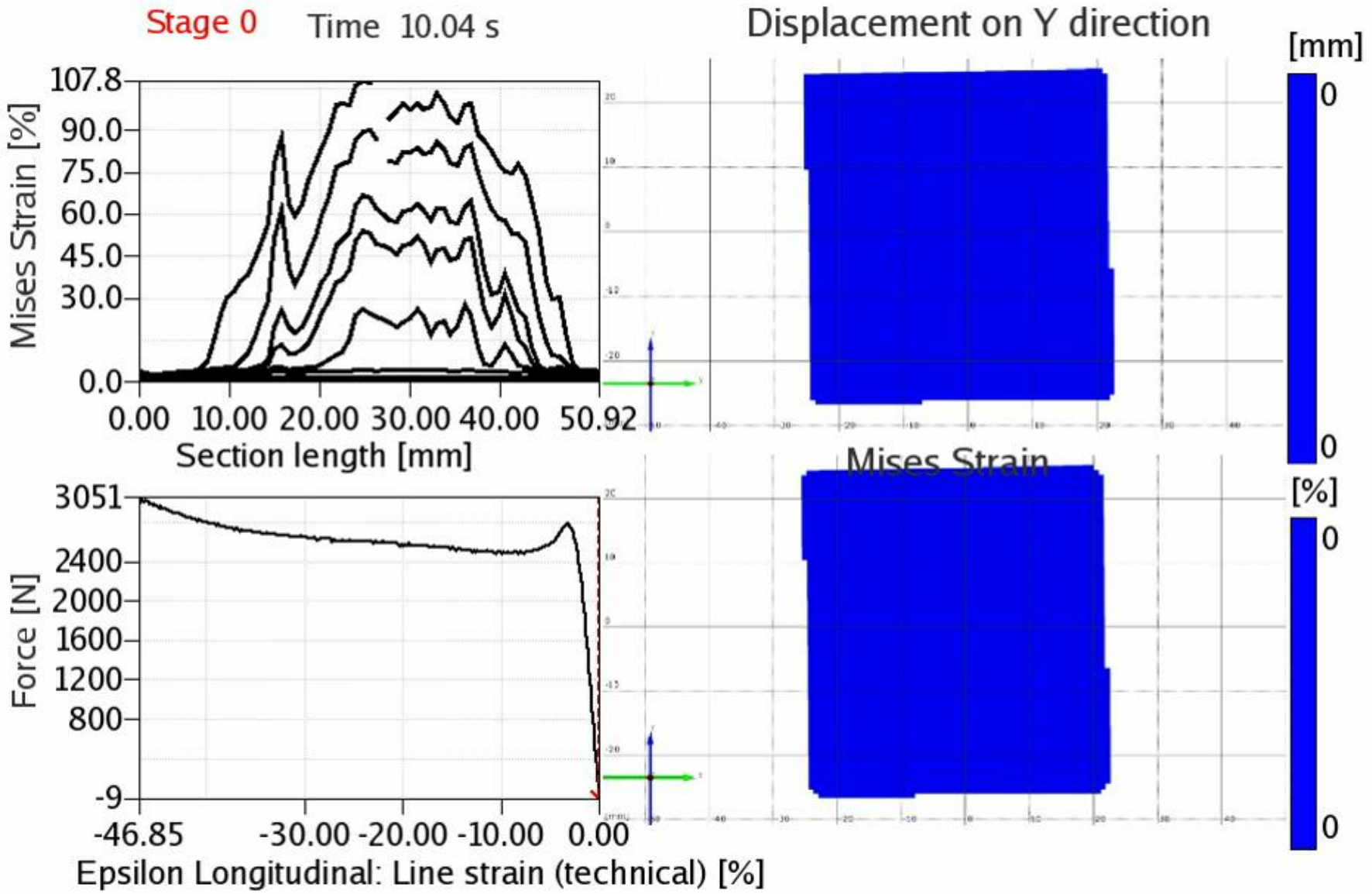
Stage 0
Time 10.04 s
Displacement on Y direction
[mm]
0
0
Mises Strain [%]
107.8
90.0
75.0
60.0
45.0
30.0
0.0
0.00 10.00 20.00 30.00 40.00 50.92
Section length [mm]
Mises Strain
[%]
0
0
Force [N]
3051
2400
2000
1600
1200
800
-9
-46.85 -30.00 -20.00 -10.00 0.00
Epsilon Longitudinal: Line strain (technical) [%]

140 kg/m^3

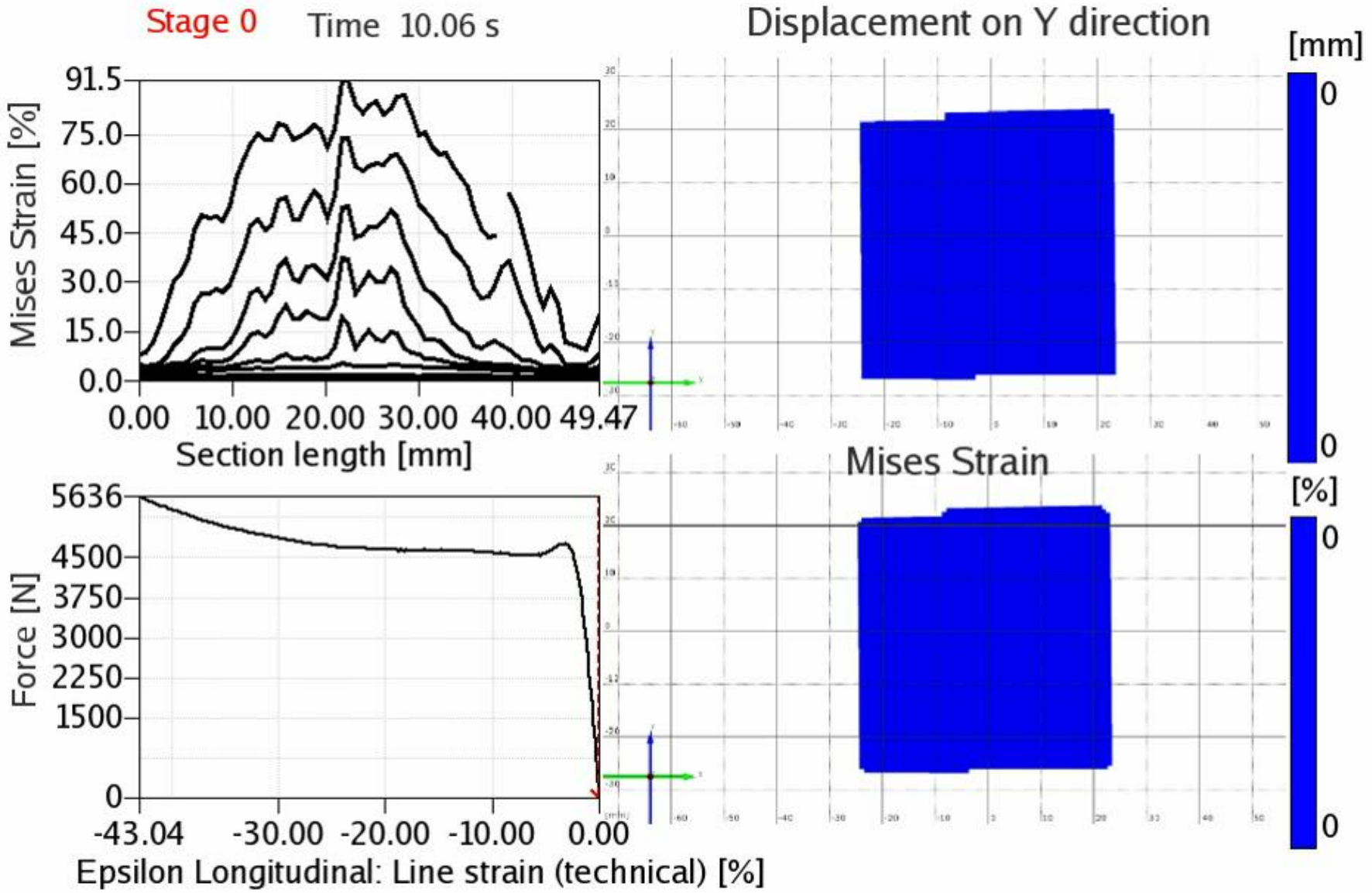
Stage 0
Time 10.06 s
Displacement on Y direction
[mm]
0
0
Mises Strain [%]
91.5
75.0
60.0
45.0
30.0
15.0
0.0
0.00 10.00 20.00 30.00 40.00 49.47
Section length [mm]
Mises Strain
[%]
0
0
Force [N]
5636
4500
3750
3000
2250
1500
0
-43.04 -30.00 -20.00 -10.00 0.00
Epsilon Longitudinal: Line strain (technical) [%]

325 kg/m^3

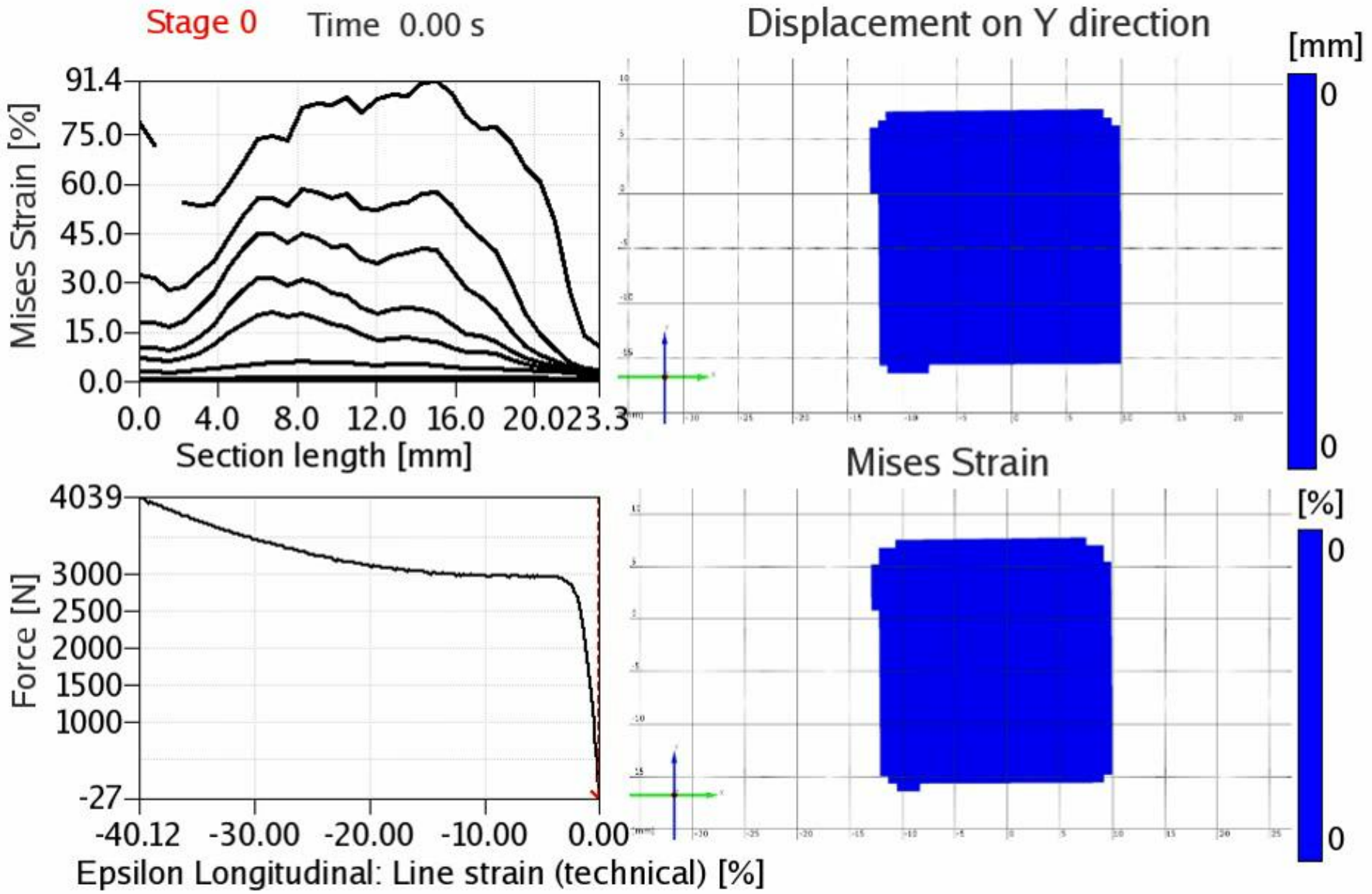
Stage 0
Time 0.00 s
Displacement on Y direction
[mm]
0
0
Mises Strain [%]
91.4
75.0
60.0
45.0
30.0
15.0
0.0
0.0 4.0 8.0 12.0 16.0 20.023.3
Section length [mm]
Mises Strain
[%]
0
0
Force [N]
4039
3000
2500
2000
1500
1000
-27
-40.12 -30.00 -20.00 -10.00 0.00
Epsilon Longitudinal: Line strain (technical) [%]

Current research in AM

M-ERA.NET project 2020-2023

Reactive Inkjet Printing of Epoxy Thermoset Composites (RIPE4TEC)

COORDINATOR (P1)	PARTNER 2:	PARTNER 3:	PARTNER 4:	PARTNER 5:
JOANNEUM RESEARCH FORSCHUNGSGESELLSCHAFT M.B.H.	BTO-EPOXY GMBH	MONTANUNIVERSITÄT LEOBEN	UNIVERSITY POLITEHNICA OF BUCHAREST	NATIONAL INSTITUTE FOR AEROSPACE RESEARCH "ELIE CARAFOLI"

The core technology to be developed in the project is **reactive inkjet printing** as a technology to enable the **additive manufacturing of novel thermoset composites** based on epoxy-polyamine resins.

We will *pioneer heterogeneous epoxies, composed from hard and soft microscale subdomains*, *with contrast and spatial distribution, which will be designed by modelling such to enhance the overall material toughness, without compromising its strength and modulus*. *Functionalized nanoparticles will be introduced at specific sites to either produce reinforcement or to enhance energy dissipation*.

The proposal addresses **two important needs**:

(i) The need of 3D printing with thermoset materials. Although AM was used extensively with thermoplastics, *printing of thermosets* is still to be convincingly demonstrated,

(ii) Epoxy is typically brittle. Any *improvement in toughness* would greatly increase its range of applications and market share.

5PhD students and 2 MSc students working in the laboratory

- ANYCUBIC Photon 3D, Digital Light Processing (DLP) – metamaterials

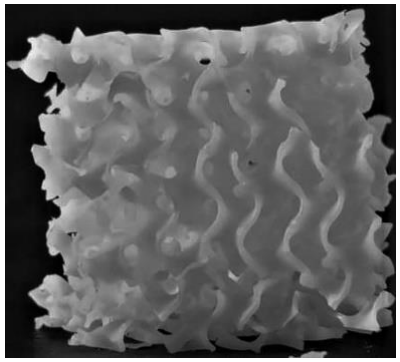

Gyroid 6x6x6 unit cells

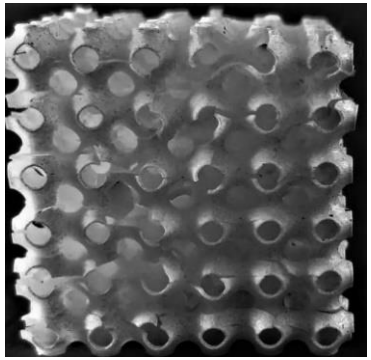

Schwarz P 6x6x6 unit cells

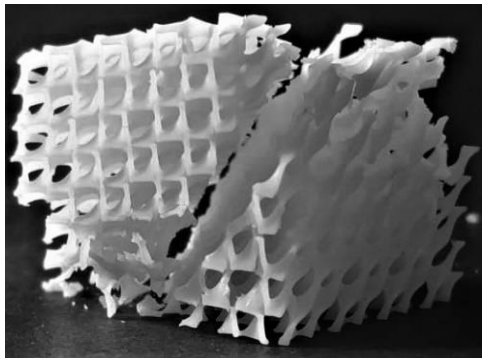

Schwarz D 6x6x6 unit cells

- CREALITY Ender-5 Pro 3D FDM

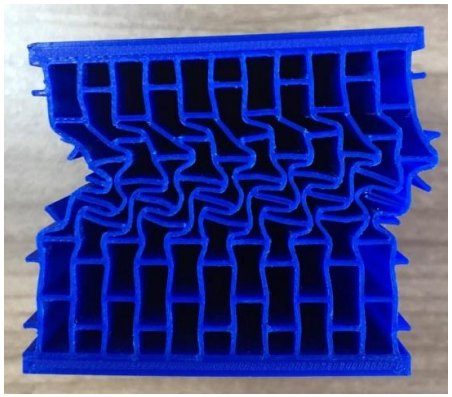

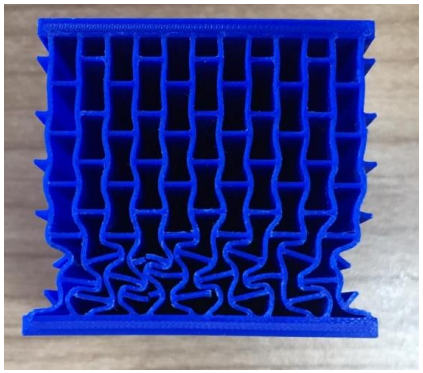

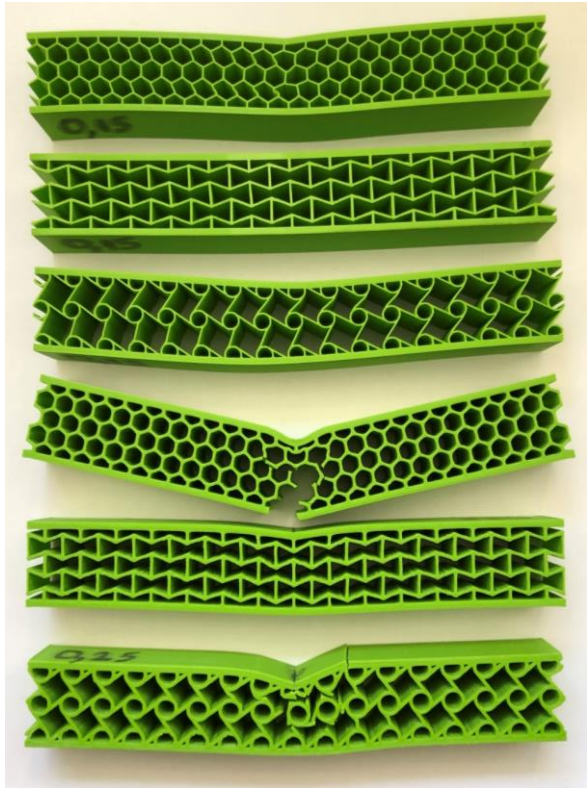

Experimental methods are beautiful!

Thank you for your attention!